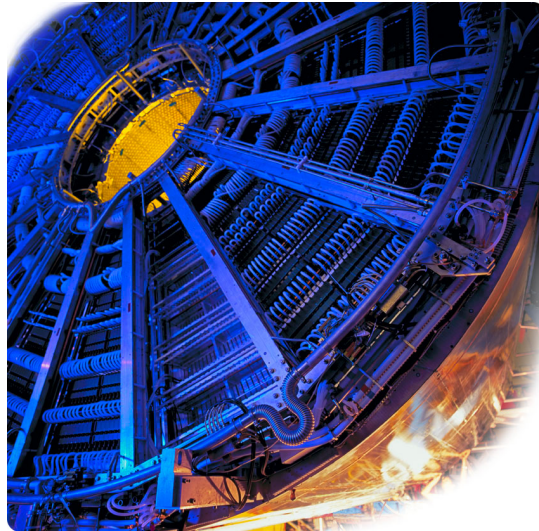


# Commissioning and Calibration of the ALICE-TPC



Dissertation  
zur Erlangung des Doktorgrades  
der Naturwissenschaften

Vorgelegt beim Fachbereich Physik  
der Goethe-Universität Frankfurt am Main

von  
Jens Wiechula  
aus Berlin

Frankfurt am Main, 2008  
(D 30)

vom Fachbereich Physik der  
Goethe-Universität Frankfurt am Main  
als Dissertation angenommen.

Dekan: Prof. Dr. Dirk-Hermann Rischke

Gutachter: PD Dr. Hans-Rudolf Schmidt  
JProf. Dr. Christoph Blume  
Prof. Dr. Peter Braun-Munzinger

Datum der Disputation: 21. April 2009

# Zusammenfassung

Quarks und Leptonen, sowie deren Anti-Teilchen, bilden aus heutiger Sicht die Grundbausteine unserer Materie (siehe Kapitel 1). Ihre Eigenschaften und Wechselwirkungen, die von sogenannten Eichbosonen vermittelt werden, sind im Standardmodell der Teilchenphysik zusammengefasst. Danach unterscheidet man sechs verschiedene Arten von Quarks (*flavours*), die als **up**, **down** - **charm**, **strange** - **top**, **bottom** bezeichnet werden und in drei Familien, angedeutet durch die Trennung mit Bindestrichen, vorkommen. Zu jeder Familie gehört neben dem Quark-Paar ein Leptonen-Paar. Die Leptonen heißen Elektron, Elektron-Neutrino - Myon, Myon-Neutrino - Tau, Tau-Neutrino, wobei im Allgemeinen die Zeichen  $e^-$ ,  $\nu_{e^-}$  -  $\mu$ ,  $\nu_\mu$  und  $\tau$ ,  $\nu_\tau$  verwendet werden. Die physikalischen Eigenschaften der Teilchen-Familien sind absolut identisch, der einzige Unterschied liegt darin, dass sich die Massen der Teilchen unterscheiden: Sie steigen mit jeder Familie an.

Eine interessante Eigenschaft der Quarks ist, dass sie niemals einzeln auftreten, sondern entweder in Mesonen, welche Quark-Antiquark-Paare sind ( $q\bar{q}$ ) oder Baryonen, bestehend aus Quark- bzw. Antiquark-Triplets ( $qqq$ ,  $\bar{q}\bar{q}\bar{q}$ ), gebunden sind. Diese Eigenschaft nennt man *Confinement*. Zusammen bilden Mesonen und Baryonen die Gruppe der Hadronen, der stark wechselwirkenden Teilchen.

Die starke Wechselwirkung ist neben der elektromagnetischen, der schwachen und der gravitativen, eine der vier grundlegenden Wechselwirkungen. Sie bindet sowohl die Quarks in den Hadronen als auch die Neutronen und Protonen in den Kernen unserer Atome. Ähnlich zur elektrischen Wechselwirkung, die eine Kraft zwischen (elektrisch) geladenen Teilchen vermittelt, wirkt die starke Wechselwirkung auf die so genannte *Farb-Ladung* (kurz Farbe) der Quarks. Neben den Eigenschaften einen 'flavour' (engl.: Geschmack) und eine elektrische Ladung zu haben, trägt ein Quark also u.a. eine Farbe, bzw. ein Anti-Quark eine Anti-Farbe. Es existieren drei verschiedene Farb(ladung)en: Rot, Grün und Blau. Die Eigenschaft des Confinement lässt sich damit so formulieren, dass ein Hadron nach außen hin immer *farbneutral* (weiß) erscheinen muss. Das lässt sich entweder durch eine Kombination von Farbe + Anti-Farbe = Weiß ( $q\bar{q}$ ), bzw. in Anlehnung an die Farblehre die Kombination Rot + Grün + Blau = Weiß ( $qqq$ ), bzw. deren Anti-Farben, erreichen. Die Eichbosonen der elektromagnetischen Wechselwirkung sind die Photonen. Die der Farb-Wechselwirkung nennt man *Gluonen*.

In der Theoretischen Physik wird die starke Wechselwirkung durch die *Quanten Chromo Dynamik* (QCD) beschrieben. Diese erlaubt es, Vorhersagen darüber zu machen, wie sich ein System aus Hadronen verhält, wenn man Druck und/oder Temperatur variiert. U.a. sagt die QCD voraus, dass bei der Überschreitung einer kritischen Temperatur  $T_c$  von ca. 170 MeV ( $\sim 10^{12}$  K) ein Phasenübergang von einem Gas aus Hadronen zu einem Zustand von freien Quarks und Gluonen stattfindet. Dieser Zustand wird als *Quark-Gluon-Plasma* bezeichnet. Es wird angenommen, dass im frühen heißen Universum, zwischen ca.  $10^{-5}$  und  $10^{-4}$  s nach dem Urknall, ein Quark-Gluon-Plasma existiert hat, bevor es sich weit genug abkühlte und die uns umgebende Materie entstehen konnte. Heute könnte dieser Zustand noch im Inneren von Neutronen-Sternen existieren, in deren Zentrum die Materie so stark komprimiert wird, dass die Quarks keinem einzelnen Nukleon mehr zugeordnet

werden können, sie sich also über einen großen Bereich frei bewegen können.

Seit ca. 30 Jahren versucht man ein solches Quark-Gluon-Plasma im Labor zu erzeugen und somit den Zustand der Materie kurz nach dem Urknall zu erforschen. Dafür werden an Beschleunigeranlagen Kerne schwerer Ionen bei ultrarelativistischen Energien zur Kollision gebracht. In dem dabei entstehenden Feuerball werden Temperaturen erzeugt, die hoch genug sein sollten, um den vorausgesagten Phasenübergang zu erreichen. Der Feuerball, anfänglich ein Quark-Gluon-Plasma, dehnt sich mit der Zeit aus und kühlt dabei ab. Unterhalb der kritischen Temperatur *hadronisiert* das System von freien Quarks und Gluonen zu gebundenen Mesonen und Baryonen. Durch weiteres Abkühlen hören die unelastischen Stöße auf, bei denen sich die Teilchenzusammensetzung des Systems noch ändern kann. Nach diesem *chemischen Ausfrieren* ist die Anzahl der verschiedenen Teilchenarten festgelegt. Als *kinetisches Ausfrieren* bezeichnet man den Punkt, an dem die Temperatur so weit gesunken ist, dass auch die Impulse der Teilchen sich nicht mehr ändern und sie wechselwirkungsfrei auseinander streben.

Zur Bestimmung der Eigenschaften jedes einzelnen Teilchens bedarf es hochpräziser Detektor-Systeme. Um das intrinsische Auflösungsvermögen der Detektoren zu erreichen, ist nicht nur eine präzise mechanische Fertigung notwendig, sondern auch ein anschließendes genaues Verständnis des Detektorverhaltens sowie eine exakte Kalibration.

Eines der Experimente, dessen Hauptaugenmerk der Auswertung von Schwerionen-Kollisionen gilt, ist das ALICE (A Large Ion Collider Experiment) Detektorsystem (siehe Kapitel 2). ALICE ist darauf optimiert, Stöße schwerer Atomkerne bei den am LHC (Large Hadron Collider) höchstmöglichen Energien von  $\sqrt{s} = 5.5$  TeV pro Nukleonen-Paar auszuwerten. Die maximal vorausgesagte Anzahl der dabei entstehenden geladenen Teilchen pro Pseudorapiditätseinheit<sup>1</sup> ist  $dN_{ch}/d\eta \approx 8000$ . Für den zentralen Teil von ALICE ergibt sich daraus eine Anzahl von 20000 geladenen primären und sekundären Teilchen, von denen jedes einzelne rekonstruiert werden soll.

Der Hauptdetektor für die Spurrekonstruktion der in der Kollision entstandenen Teilchen ist mit einem aktiven Volumen von ca.  $88 \text{ m}^3$  und einer aktiven Auslesefläche von  $32.5 \text{ m}^2$  die größte bis jetzt gebaute TPC. Die Auslesefläche ist dabei in 557568 einzelne Ausleseeinheiten (Pads) segmentiert. Neben anderen Detektoren befindet sie sich in dem 0.5 T Solenoid-Magneten des vorigen L3-Experiments. Die vorliegende Arbeit beschäftigt sich mit der Inbetriebnahme und Kalibration der TPC (Time Projection Chamber) des ALICE Detektor-Systems. Daher wird die TPC in Kapitel 3 detailliert beschrieben.

Eine TPC ist ein Teilchendetektor, der es ermöglicht, die Trajektorien der durch sein aktives Volumen fliegenden Teilchen dreidimensional im Raum zu rekonstruieren. Geladene Teilchen mit relativistischen Geschwindigkeiten ionisieren das Gas des Detektors entlang ihrer Flugbahn. In einem elektrischen Feld driften die Ionisations-Elektronen zu einer Ausleseebene, welche die *Projektion* der Spur auf diese Ebene misst. Hierdurch werden zwei der drei Raumkoordinaten bestimmt. Mit Hilfe der gemessenen *Flugzeit* sowie der als bekannt vorausgesetzten Driftgeschwindigkeit der Elektronen im Detektorgas, lässt sich die dritte Raumkomponente ermitteln. Eine Rekonstruktionssoftware findet solche "Cluster", bestimmt über eine Schwerpunktbildung den dreidimensionalen Ortspunkt und verbindet anschließend die Punkte zu den Teilchenpuren. Über den spezifischen Energieverlust pro Wegstrecke  $dE/dx$  lässt sich zudem die Teilchensorte bestimmen. Über die Krümmung der Bahn im magnetischen Feld wird der Impuls des Teilchens bestimmt.

---

<sup>1</sup>Die Pseudorapidität  $\eta$  hängt direkt vom Polarwinkel  $\theta$  unter dem die Teilchen dem Interaktionspunkt entfliehen ab:  $\eta = -\ln(\tan(\theta/2))$

Die ALICE-TPC ist ca. 5 m lang und in radialer Richtung durch zwei Zylinder bei  $r \approx 60$  cm und  $r \approx 280$  cm beschränkt. Das aktive Volumen wird von zwei zusätzlichen Zylindern bei  $r \approx 80$  cm und  $r \approx 250$  cm eingefasst. Eine zentrale Elektrode teilt den Detektor in zwei Driftregionen von 2.5 m Länge. Sie werden als A- bzw. C-Seite bezeichnet. Die Enden der TPC sind in 18 trapezförmige Sektoren unterteilt, wobei jeder dieser Sektoren eine innere (IROC) und eine äußere (OROC) Auslesekommer fasst. Damit besteht die TPC auf jeder Seite aus 36 einzelnen trapezförmigen Detektoren.

Für die Detektion der Teilchen werden in der ALICE-TPC Vieldraht-Proportionalkammern mit einer segmentierten Kathodenebene verwendet. Diese bestehen aus der Padebene, einer Ebene aus Anodendrähten und einer Kathodenebene, die als Drahtebene realisiert ist, damit die driftenden Elektronen zu den Anodendrähten gelangen können. An diesen erfahren die Elektronen ein immer größeres elektrisches Feld, je näher sie einem der Drähte kommen. Ab einem gewissen Punkt ist ihre Energie so hoch, dass sie das Gas ionisieren können und ein zweites Elektron erzeugt wird, welches seinerseits anfängt zu driften und das Gas zu ionisieren. Dadurch entsteht ein Lawinenprozess, der die anfängliche Ladung um ein Vielfaches verstärkt. Die Spannung an den Anodendrähten ist dabei so gewählt, dass die Verstärkung proportional zur ursprünglichen Ladung erfolgt.

Während die Elektronen typischerweise innerhalb weniger Nanosekunden von den Anodendrähten absorbiert werden, driften die entstandenen Ionen mit einer ca. 1000fach niedrigeren Geschwindigkeit in Richtung des aktiven Volumens. Um zu verhindern, dass sie dort als sich ansammelnde Raumladung das Driftfeld verzerren, befindet sich zwischen den Kathodendrähten und dem Driftvolumen eine weitere Drahtebene. Die Drähte dieser so genannten ‘Gate-Ebene’ können alternierend auf positive und negative Spannung gelegt werden. In diesem Fall enden die Feldlinien der driftenden Ionen auf den Gate-Drähten. Zusätzlich enden aber auch die Feldlinien der aus dem Driftvolumen kommenden Elektronen auf den Gate-Drähten. Somit ist der Detektor ‘blind’ für weitere Teilchenspuren. Im Normalbetrieb bleibt das Gate geschlossen, bis von einem Trigger-Detektor ein Ereignis gemeldet wird. Dann wird das Gate für die Dauer der Auslese geöffnet und anschließend wieder geschlossen. Somit wird verhindert, dass ständig eine Gasverstärkung stattfindet, was eine Belastung für den Detektor bedeuten würde.

Die von den Anodendrähten wegdriftenden Ionen erzeugen auf der Padebene eine Spiegelladung, die von ladungsempfindlichen Verstärkern und Pulsformern (PASA-Chips) für die anschließende Digitalisierung aufbereitet werden. Die hierfür benötigte Elektronik sitzt direkt am Detektor (‘Front-End-Elektronik’) und besitzt einen digitalen Verarbeitungsschaltkreis. Das anfallende Rohdaten-Volumen von ca. 700 MB pro Kollision verlangt eine Nullunterdrückung der Daten bereits auf dem Level der Front-End Elektronik, was die Notwendigkeit eines digitalen Schaltkreises erklärt. Hierfür muss für jeden Kanal die elektronische Basislinie (Pedestal) gemessen, und an die Elektronik geschickt werden.

Simulationen der Detektorrespons haben gezeigt, dass der Rauschabstand der Elektronik mindestens 30:1 sein muss, um das intrinsische Auflösungsvermögen des Detektors voll ausschöpfen zu können. Die Elektronik wurde zusammen mit den möglichen Gasverstärkungsfaktoren gerade so ausgelegt, dass die minimale Ionisation eines Teilchens ein Signal von 30 ADC Kanälen hervorruft. Das Elektronikrauschen sollte somit einen Wert von einem ADC Kanal nicht überschreiten, was relativ genau der äquivalent-Ladung von 1000 Elektronen entspricht. Der intrinsische Wert der verwendeten Verstärkerbausteine liegt bei 570 Elektronen. Aufgrund der an seinem Eingang liegenden Kapazität ist der resultierende Wert höher. Durch Erdungsschleifen kann das Rauschen der Elektronik ebenfalls steigen. Eine genaue Messung des Rauschens ist daher notwendig.

Um das Verstärkungs- und Pulsformverhalten der Elektronik studieren zu können, lässt sich auf der Kathodendrahtebene ein Puls einspeisen, der ein Signal ähnlich dem der Gasverstärkung erzeugt. Damit lassen sich herstellungsbedingte Variationen in der Elektronik-Respons messen und korrigieren.

Kapitel 4 beschäftigt sich mit der ersten Inbetriebnahme der TPC und Auswertung der dabei genommenen Daten. Die Inbetriebnahme fand in einem Reinraum am ‘Point 2’ des CERN statt, wo der Detektor auch bereits zusammengebaut wurde. Der Einbau der Vieldraht-Proportionalkammern begann Ende August 2005 und dauerte etwas länger als einen Monat. Nach ihrem Einbau wurde mit Hilfe einer fotogrammetrischen Vermessung die Position aller Kammern relativ zur zentralen Elektrode bestimmt. Mit Hilfe von Abstandstücken ist eine Feinjustage der Kammern möglich. Die in Verbindung mit der photogrammetrischen Messung erreichte Präzision beträgt 100  $\mu\text{m}$ .

Ziel der Inbetriebnahme im Jahr 2006 war das Testen der Auslesekanäle nach deren Einbau mit der endgültigen Elektronik und das Studieren der Detektor-Eigenschaften. Für den Fall, dass sich herausgestellt hätte, dass eine Kammer nicht nach ihren Spezifikationen funktioniert, wäre es am sichersten gewesen, diese noch im Reinraum auszutauschen. In der endgültigen Position der TPC unter Tage ist sowohl der Platz stark beschränkt als auch das Herstellen von Reinraum-Bedingungen nicht trivial. Daher war es entscheidend, alle Systeme der TPC bereits getestet und deren Funktionsfähigkeit verifiziert zu haben, bevor sie in die endgültige Position gebracht wurde.

Im Reinraum konnten jeweils nur zwei Sektoren, also vier Auslesekanäle gleichzeitig in Betrieb genommen werden. Dies war dadurch bedingt, dass die Elektronik wassergekühlt ist und das zur Verfügung stehende Kühlsystem nur den Betrieb zweier Sektoren zuließ. In der Zeit zwischen dem 27.6. und 11.8.2006 wurden alle Sektoren paarweise nach und nach in Betrieb genommen. Ein zweite Runde von Tests erfolgte ab dem 18.8. und ging bis Ende des Jahres. Ihr Hauptanliegen war der Dauerbetrieb inklusive Datennahme jeden Sektors für mindestens 48 Stunden, um die Elektronik einem Belastungstest zu unterziehen.

Die Vorliegende Arbeit beschäftigt sich mit der Bestimmung der Pedestalwerte, der Analyse des Elektronikrauschens sowie der Auswertung von Signalen, des Kalibrations-Pulsers. Des Weiteren wurden Daten analysiert, die mit dem Laserkalibrations-System erzeugt wurden.

Die gemessenen Pedestalwerte der Auslesekanäle folgen einer Gauß-Verteilung um einen Mittelwert von ca. 50 ADC Kanälen. Das entspricht den erwarteten Designvorgaben. Die Verteilung des Elektronikrauschens hat ein Maximum bei ca. 0.7 ADC Kanälen mit einem langen Schwanz zu höheren Werten hin. Der Anteil der Kanäle mit einem Rauschen höher als 1 ADC Kanal beträgt dabei 10 %. Um eine effiziente Nullunterdrückung sicherzustellen und somit das Datenvolumen zu minimieren, ist dieser Anteil wesentlich zu hoch. Darüber hinaus wird für diese Kanäle der geforderte Rauschabstand nicht eingehalten. Eine genaue Analyse des Rauschverhaltens ist daher erforderlich.

Das Rauschen an ladungsempfindlichen Vorverstärkern steigt linear mit der Eingangskapazität. Daher ist zu erwarten, dass das Rauschen sowohl von der Padgröße<sup>2</sup>, als auch der Länge der Leiterbahnen der Ausleseebene<sup>3</sup> abhängt. Die Analyse des Rauschverhaltens erfolgt daher für die drei verschiedenen Padgrößen getrennt und wird auch jeweils in

---

<sup>2</sup>Die Größe der IROC-Pads beträgt  $4 \times 7.5 \text{ mm}^2$ , die OROC besitzt zwei verschiedene Padgrößen:  $6 \times 10 \text{ mm}^2$  im inneren und  $6 \times 15 \text{ mm}^2$  im äußeren Teil.

<sup>3</sup>Die Ausleseebene oder Padebene ist eine dreilagige Platine, auf deren Oberfläche die Padstruktur geätzt ist. Die Pads sind über Leiterbahnen mit Steckern auf der Rückseite der Padebene verbunden.

Abhängigkeit der Leiterbahnlänge betrachtet.

Alle Padgrößen zeigen eine lineare Abhängigkeit des Rauschens von der Leiterbahnlänge. Da die Kapazität der Leiterbahn linear mit ihrer Länge ansteigt war dies, wie oben erläutert, zu erwarten. Das Rauschen steigt von der kürzesten (ca. 5 mm) bis zur längsten (ca. 150 mm) Leiterbahn von ca. 0.6 ADC Kanälen auf ca. 1 ADC Kanal an. Ein Teil der Pads folgt jedoch nicht diesem Trend, sondern zeigt ein höheres Rauschen.

Der Anteil der Pads mit einem Rauschen Größer als 1 ADC Kanal beträgt für die verschiedenen Padgrößen (IROC, OROC kurze pads, OROC lange Pads) 0.6 %, 11 % bzw. 24 %. Der höchste Anteil kommt also von den größten Pads. Es hat sich gezeigt, dass Pads mit hohem Rauschverhalten auf wenige, in allen Ausleseammern identische Bereiche beschränkt ist. Betroffen sind Pads entlang der Kanten in radialer Richtung als auch Pads in den äußeren Ecken der Kammern.

Das unerwartet hohe Rauschen konnte durch den ‘ground bounce’ Effekt erklärt werden: Die in der Front-End-Elektronik (FEE) verwendete CMOS Technologie besitzt die Eigenschaft, bei einem schnellen Schaltsignal niederohmig zu werden. Dies passiert in der FEE zu dem Moment, an dem der Start zur Auslese erteilt wird. Fangen alle 557568 gleichzeitig mit der Auslese an, so bedingt dies kurzzeitig einen sehr hohen Strom. Auf Grund der endlichen Widerstände im System ändert sich dadurch in diesem Zeitraum die Versorgungsspannung der Elektronik und dadurch bedingt die für einen stabilen Betrieb notwendigen Referenzspannungen der einzelnen Komponenten. Hierdurch wird ein Rauschen verursacht.

Zwei Maßnahmen konnten diesen Effekt wesentlich verringern. Zum einen bietet die Elektronik die Möglichkeit die Auslese einzelner Gruppen von Pads zu einem verschiedenen Zeitpunkt zu starten. Somit wird der momentan fließenden Strom verringert. Zum anderen konnte der Effekt weiter verringert werden, indem die Erdung der FEE verbessert wurde. Nach diesen beiden Änderungen war im Wesentlichen nur noch die Abhängigkeit des Rauschens von der Leiterbahnlänge zu beobachten.

Mit Hilfe des Kalibrations-Pulsers, der ein Signal auf die Kathodendrahtebene einspeist, wurde die Elektronik Respons untersucht. Bedingt durch den Herstellungsprozess variiert das Pulsformverhalten von Chip zu Chip. Das wirkt sich sowohl auf die Bestimmung der Ankunftszeit, als auch der ankommenden Ladung aus. Mit den hierbei gemessenen Werten lassen sich die Daten korrigieren.

Die gemessenen Variationen der Ankunftszeit zeigen eine Gauß-Verteilung mit einer Breite (Sigma) von 6.2 ns. Der Fehler, der hierdurch in der Ortsauflösung entsteht, beträgt in etwa 170  $\mu\text{m}$ . Der durch die Diffusion der Driftelektronen im Gas erwartete Fehler in der Ortsauflösung beträgt je nach Driftdistanz zwischen 300 und 800  $\mu\text{m}$ . Die herstellungsbedingten Chip zu Chip Variationen sind somit nicht dominierend. Da der Messfehler statistisch über die Cluster einer Teilchenspur verteilt ist, hat dieser keinen Einfluss auf die Ortsauflösung der Spur selbst.

Für die gemessene relative Ladungs-Verteilung (normiert auf den Mittelwert der jeweiligen Ausleseammern) erhält man ebenfalls eine Gauß-Verteilung. Ihre Breite entspricht einer relativen Abweichung von 2.8 %. Um die intrinsische Auflösung des spezifischen Energieverlustes ( $dE/dx$ ) von ca. 6 % zu erreichen, müssen die Chip zu Chip Variationen in der Ladungsbestimmung korrigiert werden.

Das Laserkalibrations-System reflektiert auf beiden Seiten der TPC jeweils 168 Strahlen in deren aktives Volumen. Durch Streuung können die Photonen jeden Winkel der TPC erreichen. Sie sind energetisch genug, um beim Auftreffen auf metallische Oberflächen Photoelektronen zu erzeugen. Interessant für die Detektorkalibration sind Photoelektronen von der Zentralelektrode. Die ausgelösten Elektronen sind so zahlreich, dass in

jedem Auslesepad ein Signal gemessen werden kann. Da die Zentralelektrode eine stetige Fläche ist, können Unstetigkeiten in der Ankunftszeitmessung als Fehljustage der Ausleseammern interpretiert und anschließend darauf korrigiert werden. Des Weiteren ist es möglich, globale Ausrichtungsfehler<sup>4</sup> und Feldverzerrungen zu sehen. Mit Hilfe der Daten der Zentralelektrode ist es auch möglich, die mittlere Elektronen-Driftgeschwindigkeit sowie Driftgeschwindigkeitsgradienten zu messen.

Die Messungen haben einen vertikalen Driftgeschwindigkeitsgradienten, sowie eine weitere radiale Abhängigkeit in der Ankunftszeitmessung gezeigt. Der erste Effekt lässt sich durch die Temperaturabhängigkeit der Driftgeschwindigkeit erklären: auf Grund der Höhe der TPC bildete sich ein Temperaturgradient von ca. 570 mK. Dieser kann die 1.7‰ Differenz zwischen der Ankunftszeit am oberen und unteren Rand der TPC erklären. Der zweite Effekt legt zwei Erklärungen nahe: zum einen kann eine konische Verformung der Ausleseebene vorliegen oder aber eine globale Feldverzerrung.

Die gemessene Differenz der Ankunftszeiten zwischen innerem und äußerem Radius der TPC entspricht auf der A-Seite 2.5 mm und ist über innere und äußere Ausleseammern sichtbar. Auf der C-Seite ist lediglich für die inneren Ausleseammern eine radiale Abhängigkeit zu beobachten. Diese beträgt vom inneren zum äußeren Rand der Kammer 390 µm. Eine mechanische Fehlausrichtung ist auf Grund von Messungen der Ausrichtung der Ausleseammern relativ zur Zentralelektrode sehr unwahrscheinlich. Die Messgenauigkeit des verwendeten fotogrammetrischen Verfahrens beträgt 100 µm.

Feldverzerrungen können über die Einstellungen der Offsetspannung der Gatingdröhte, sowie dem Potential von Elektroden entlang der Kammerränder beeinflusst werden. Eine genauere Untersuchung der beobachteten Effekte wurde auf Grund der Messung mit nur je zwei Sektoren gleichzeitig nicht durchgeführt. In der endgültigen Position der TPC wird diese Studie daher nachgeholt werden müssen.

Im Januar 2007 wurde die TPC aus dem Reinraum zu ihrer endgültigen Position unter Tage transportiert. Kapitel 5 befasst sich mit der Analyse der dort vorgenommenen Messungen des Elektronikrauschens. Erste Datenauswertungen haben gezeigt, dass der Anteil von Auslesepads, die ein Rauschen über 1 ADC Kanal zeigen, 24 % beträgt und damit ein Faktor 2.4 über den ersten Messungen im Reinraum liegt. Eine Analyse hat ergeben, dass das Rauschen von den Netzgeräten der FEE verursacht wurde. Der Grund war ein Gleichstrom bei einer Frequenz von ca. 300 kHz. Mit Hilfe von Ferrit-Toroiden konnte das Rauschen minimiert werden. Um die optimale Konfiguration zu finden, wurden verschiedene Anordnungen zweier unterschiedlicher Toroide untersucht. Nach der Modifikation aller Netzgeräte zeigen lediglich 1.4 % aller Auslesepads ein Rauschen größer als 1 ADC Kanal. Für die einzelnen Padgrößen erhält man 0.3 % (IROC), 0.2 % (OROC kurze Pads) und 4.9 % (OROC lange Pads).

Für die Analyse der Pedestalwerte und des Rauschverhaltens, sowie die Analyse der Kalibrations-Pulser-Daten und Signale der Zentralelektrode, wurden Kalibrations-Algorithmen entwickelt, die in das offizielle Analyse-Framework *AliRoot* von ALICE integriert worden sind.

---

<sup>4</sup>z.B. eine Nichtparallelität von Ausleseebene und Zentralelektrode







# Contents

<b>1</b>	<b>Introduction</b>	<b>1</b>
1.1	Quantum-Chromo Dynamics . . . . .	2
1.2	Quark-Gluon Plasma . . . . .	4
1.3	Relativistic Heavy-Ion Collisions . . . . .	6
1.4	Outline of this Thesis . . . . .	7
<b>2</b>	<b>A Large Ion Collider Experiment</b>	<b>9</b>
2.1	Detectors . . . . .	10
2.1.1	Central barrel . . . . .	10
2.1.2	Central single-arm Detectors . . . . .	11
2.1.3	Forward Region . . . . .	12
2.2	Coordinate Systems . . . . .	13
2.2.1	Global Coordinate System . . . . .	13
2.2.2	Local Coordinate System . . . . .	13
<b>3</b>	<b>The Alice TPC</b>	<b>15</b>
3.1	Functional Principle . . . . .	16
3.2	Physics Processes . . . . .	18
3.2.1	Energy Loss of Charged Particles in Gases . . . . .	18
3.2.2	Two Photon Ionisation using UV Lasers . . . . .	19
3.2.3	Drift Properties of Electrons in Gases . . . . .	20
3.2.4	Gas Amplification and Signal Generation . . . . .	23
3.3	Technical Design . . . . .	25
3.3.1	Mechanical Structure . . . . .	25
3.3.2	Field Cage and Field Cage Rods . . . . .	26
3.3.3	Service Support Wheel . . . . .	28
3.3.4	Readout Chambers . . . . .	28
3.3.5	Front-end Electronics . . . . .	29
3.3.6	Sector Naming Conventions and Usage of the Field Cage Rods . . . . .	32
3.4	Auxiliary Systems . . . . .	34
3.4.1	Laser Calibration System . . . . .	34
3.4.2	Choice of the Gas Mixture and the Gas System . . . . .	36
3.4.3	Cooling System . . . . .	37
3.4.4	Temperature Monitoring System . . . . .	38
3.4.5	Gating Grid Pulser System . . . . .	38
3.4.6	Calibration Pulser System . . . . .	39
<b>4</b>	<b>The TPC Commissioning in SXL2</b>	<b>41</b>
4.1	Introduction . . . . .	41
4.2	Setup . . . . .	42
4.3	Results . . . . .	44

## Contents

4.3.1	Mechanical Alignment of the Readout Chambers . . . . .	44
4.3.2	Pedestal Distribution and Detailed Noise Studies . . . . .	45
4.3.3	Calibration Pulser . . . . .	55
4.3.4	Laser Events . . . . .	59
4.3.5	Floating Wires . . . . .	67
<b>5</b>	<b>The TPC Commissioning Underground</b>	<b>69</b>
5.1	Noise Measurements . . . . .	69
5.1.1	First Noise Measurements at the Final Position . . . . .	69
5.1.2	Measurement of the Common Mode Current . . . . .	70
5.1.3	Noise Measurements with Ferrite Toroids . . . . .	71
5.1.4	Noise with the Final Configuration of the LV Power Supplies . . . . .	73
<b>6</b>	<b>Summary and Outlook</b>	<b>79</b>
<b>A</b>	<b>Description of the calibration classes</b>	<b>81</b>
A.1	Common introduction . . . . .	81
A.2	Pedestal calibration class . . . . .	82
A.2.1	Signal filling [Update(...)] . . . . .	82
A.2.2	Calibration value calculation [Analyse()] . . . . .	83
A.2.3	Stored calibration values . . . . .	83
A.3	Pulser calibration class . . . . .	83
A.3.1	Signal filling [Update(...)] . . . . .	83
A.3.2	Channel information processing [ProcessPad()] . . . . .	83
A.3.3	Event information processing [EndEvent()] . . . . .	84
A.3.4	Calibration value calculation [Analyse()] . . . . .	84
A.3.5	Stored calibration values . . . . .	84
A.4	Central electrode signal calibration class . . . . .	84
A.4.1	Signal filling [Update(...)] . . . . .	84
A.4.2	Channel information processing [ProcessPad()] . . . . .	85
A.4.3	Event information processing [EndEvent()] . . . . .	85
A.4.4	Calibration value calculation [Analyse()] . . . . .	86
A.4.5	Stored calibration values . . . . .	86
A.5	Using the Calibration Classes . . . . .	86
<b>B</b>	<b>Additional data</b>	<b>89</b>
B.1	Pedestal and Noise calibration . . . . .	89
B.2	Central Electrode analysis . . . . .	90
	<b>Bibliography</b>	<b>96</b>





# 1 Introduction

About 2500 years ago the greek philosophers Leukipp and Demokrit argued that everything is composed entirely of various imperishable, indivisible elements they called ‘atomos’ (greek: indivisible). However it was only during the last two centuries that our understanding of the structure of matter evolved. J.L.Proust and J.Dalton observed at the beginning of the 19<sup>th</sup> century that chemical elements always bind in discrete proportion to their masses. Between 1869 and 1872 Dimitrij Mendelejew and Lothar von Meyer independently ordered the known elements by their chemical properties. The resulting table, known today as the ‘periodic table of the chemical elements’, summarises the building blocks of matter - our *atoms*.

It was in 1897 when J.J. Thomson found that a hot cathode emits particles significantly smaller than atoms - the *electrons*. Therefore he proposed that the “indivisible” atom has a substructure and developed an atomic model, where positive particles and negative electrons are homogeneously distributed inside a sphere. Ernest Rutherford, the “father” of nuclear physics, found in his famous scattering experiments, where he bombarded a gold foil with alpha particles, that the atom is mostly empty space with nearly all of its mass and one of its two kinds of charges concentrated in a tiny centre. His results led to a new atomic model with a positively charged nucleus and electrons orbiting around it. In 1920 Rutherford introduced the name *proton* for the positively charged hydrogen nucleus. With the discovery of the *neutron* by J. Chadwick in 1932, the last building block of the atom was found and the modern picture of the atom was formed: The nucleus, which is made of *nucleons* (protons and neutrons) is surrounded by a cloud of electrons.

With the discovery of the *muon* in 1937 the belief of having found the building blocks of matter in electrons, protons and neutrons had to be given up. Starting with the discovery of the *pion* and the *kaon* in cosmic ray induced interactions in 1947, a complete “particle zoo” emerged. From the 1950s on, new particles were also found in scattering experiments. Today the zoo is filled by more than 250 particles. The found particles had been classified according to their mass into medium weight particles called *mesons* (greek “mesos”: medium, including e.g. the pion and the kaon) and heavy weight particles called *baryons* (greek “barys”: heavy, including the neutron and proton), which together form the group of strongly interacting particles - the *hadrons*.

In 1964 M. Gell-Mann and G. Zweig independently proposed a model which could explain all the up to then known particles by introducing a substructure of three particles and their anti-particles. In his publication “A Schematic Model of Baryons and Mesons” [1] Gell-Mann called those particles *quarks* which gave them their name. By allowing combinations of either a quark with an anti-quark ( $q\bar{q}$ ) or a quark or anti-quark triplet ( $qqq$ ,  $\bar{q}\bar{q}\bar{q}$ ) the known particles could be grouped into multiplets using a unitary symmetry. This symmetry is know today as the SU(3)-Flavour symmetry. First experimental evidence for the existence of a substructure of the nucleons came from experiments at the Stanford Linear Accelerator Center (SLAC) in 1969 from high energy inelastic scattering experiments of electrons off nucleons [2]. While former experiments probed the high energy behaviour of the scattering amplitude at low momentum transfer (small scattering angles) the new

---

## 1 INTRODUCTION

---

experiments studied large momentum transfers that probed the short distance structure of the hadrons (large scattering angles). The scaling behaviour which was seen in the data had been predicted by Bjorken end of 1968 [3]. Feynman explained the results by the scattering of the electrons off sub-hadronic particles [4] he called *partons*, which were later on identified with the quarks of Gell-Mann<sup>1</sup>.

Today we know of the existence of six quarks and their anti-quarks. They exist in the *flavours* **up**, **down**, **charm**, **strange**, **top** and **bottom**. Together with the *leptons*, meaning the electron ( $e^-$ ), the muon ( $\mu$ ), the tau ( $\tau$ ) and their associated neutrinos ( $\nu_e, \nu_\mu, \nu_\tau$ ) and their anti-particles, they are today considered the building blocks of matter. All of these particles are fermions (spin 1/2). The described particles are grouped in three generations. Each generation consists of a quark pair and a lepton pair.

	Generation 1		Generation 2		Generation 3	
Quarks	Up	$u$	Charm	$c$	Top	$t$
	Down	$d$	Strange	$s$	Bottom	$b$
Leptons	Electron	$e^-$	Muon	$\mu$	Tau	$\tau$
	Electron-Neutrino	$\nu_e$	Muon-Neutrino	$\nu_\mu$	Tau-Neutrino	$\nu_\tau$

**Table 1.1:** *Fermions of the Standard Model*

To describe these particles and their interactions in a single theory is the great goal of particle physics. The search for such a theory led to the development of the *Standard Model of particle physics* (SM)<sup>2</sup> which combines three of the four known fundamental forces: the electromagnetic, the weak and the strong interaction<sup>3</sup>. The SM is a model based on the local gauge group  $SU(3) \otimes SU(2)_L \otimes U(1)_Y$ , where the  $SU(3)$  gauge group or *colour group* describes the strong interactions and the  $SU(2)_L \otimes U(1)_Y$  gauge group the unified weak and electromagnetic interactions.

### 1.1 Quantum-Chromo Dynamics

The theory based on the  $SU(3)$  gauge group describing the strong interactions is a non-Abelian quantum field theory called *Quantum-Chromo Dynamics* (QCD). QCD introduces a new quantum number called colour. This prevents baryonic wave functions (e.g.  $\Delta^{++}(1238)=(uuu)$ ), which are symmetrical under the exchange of quarks, to violate Fermi statistics. A quark thus carries one of the colours red, green or blue (or the anti-colour). In  $SU(3)$  hadronic wave functions are colour neutral states (colour singlets), resulting in the above mentioned meson ( $q\bar{q}$ ) or baryon ( $qqq, \bar{q}\bar{q}\bar{q}$ ) states. For a meson colour neutrality means the combination of colour + anti-colour = white (e.g. red + anti-red) and for baryons, following chromatics, red + green + blue = white. This also explains the origin of the name QCD. The strong interaction is mediated between the quarks by eight massless gauge bosons called *gluons*. A crucial difference to Quantum Electro Dynamics (QED), which describes the electro-magnetic interactions with the (electric-)charge neutral photon as the gauge boson, the gluons carry (colour-)charge and therefore interact among each other. This has severe consequences as will be seen below.

---

<sup>1</sup>The term parton today also includes the gluon (see below).

<sup>2</sup>For an introduction see e.g. [5].

<sup>3</sup>Gravitation, being the fourth fundamental force, in principle should also be included in the model, but at the accessible energies their impact on the interaction of fundamental particles is negligible.



The development of QCD had the problem that it was necessary to describe two seemingly contradictory problems:

- In deep inelastic electron nucleon scattering (meaning large momentum transfer) pointlike particles have been identified which move nearly freely within the nucleon. This phenomenon is known as *asymptotic freedom*<sup>4</sup>.
- However, trying to separate a single one of these partons is not possible. It seems that no matter how large the transferred momentum is, the partons are bound into the hadrons. This is known as *confinement*.

First attempts, in the 1950's, to explain these effects with the help of field theory failed and it was first thought that field theory was the wrong tool to describe strong interactions. This however changed rapidly with the discovery of asymptotic freedom by Gross and Wilczek and Politzer [7, 8], which were awarded with the [Nobel Prize in 2004](#). They could show that the coupling constant of the strong interaction  $\alpha_S$  is strongly energy dependent and decreases with increasing momentum transfer  $Q$ . Therefore, at long distances the coupling is strong, confining the quarks inside the hadron, while at short distances the coupling is weak, allowing the quarks to move freely within the hadron. In Fig. 1.1 results from measurements are compared with QCD predictions.

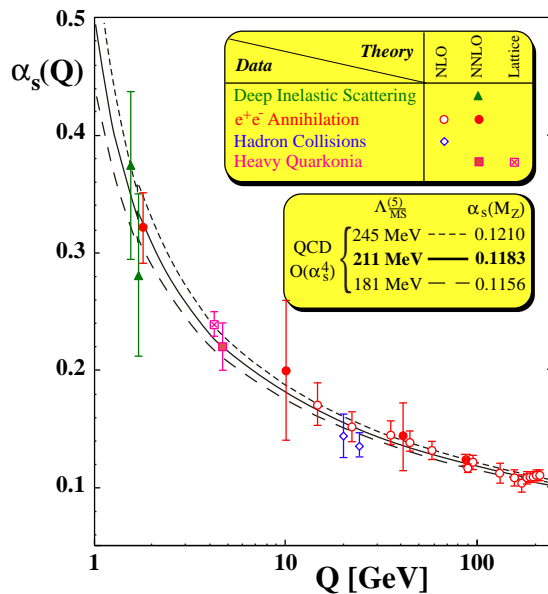


**Figure 1.1:** Summary of measurements of the strong coupling constant  $\alpha_S(Q^2)$ . The measured data are compared with the running of  $\alpha_S$  as predicted by QCD calculations for three different masses of the  $Z^0$  boson<sup>5</sup> [9].

In QED a running coupling is also known, where  $\alpha \approx \frac{1}{137}$  is increasing slightly with energy. This effect is explained by the polarisation of the surrounding vacuum which screens the bare charge. Probing at shorter and shorter distances (larger momentum transfers) shrinks the size of the surrounding cloud and measures more and more the bare charge. In analogy in QCD one could expect the same effect for the quarks, where the

<sup>4</sup>A review of the discovery of asymptotic freedom and the emergence of QCD can be found in [6].

<sup>5</sup>The  $Z^0$  and  $W^\pm$  bosons are the gauge bosons of the weak interaction.

(colour-)charge is screened by the polarised vacuum. However, in QCD the gluons also carry (colour-)charge providing for an anti-screening which overcomes the screening and makes QCD asymptotically free. Therefore the gluons are responsible for the strong energy dependence of  $\alpha_S$ , thus causing confinement and asymptotic freedom.

A consequence of the energy dependence of the coupling constant is that perturbation theory in QCD only works for large momentum transfers, where  $\alpha_S$  is sufficiently small. *Perturbative QCD* (pQCD) is therefore only applicable for hard processes. For the regime of soft processes pQCD fails due to the large  $\alpha_S$  and alternative methods have to be used. One ansatz is to use the path integral method introduced by Feynman and solve the QCD Lagrangian numerically on a discretised lattice of space-time points. *Lattice QCD* is an important tool to study the behaviour of quarks and gluons in the non-perturbative region.

## 1.2 Quark-Gluon Plasma

A question that arises when thinking about confinement is whether there is any kind of matter in which quarks are not bound into hadrons but can move freely.

One possibility that comes to mind is to compress matter so much that the valence quarks of a nucleon cannot any longer be associated to this particular nucleon. It is believed that this happens in the core of neutron stars where the nuclear density is more than an order of magnitude larger ( $>1 \text{ GeV}/\text{fm}^3$ ) than under normal conditions<sup>6</sup>.

Another possibility is to heat up nuclear matter such that the quarks have a mean free path comparable to the system size. It is commonly believed that the hot early universe has been in such a phase during the first few microseconds after the Big Bang.

The state of matter where quarks can move freely over distances comparable to the system size (core of a neutron star, early universe) is called the *Quark-Gluon Plasma* (QGP).

Lattice QCD calculations predict a transition to a QGP once the system goes beyond a critical temperature  $T_C$ . Fig. 1.2 shows lattice calculations of the energy density of nuclear matter divided by  $T^4$  as a function of the temperature in units of  $T_C$ . The steep rise around  $T_C$  indicates a rapid increase in the number of degrees of freedom which indicates the phase transition from a gas of hadrons to a plasma of free quarks and gluons.

The different phases of a substance are usually displayed in a phase diagram. The most familiar example is the phase diagram of water with its solid, liquid and gaseous phase, the various coexistence lines as well as the triple point and the critical point. In the case of water the most appropriate thermodynamic potential to use is the Gibbs free energy  $G(T, P)$ . The phase diagram has therefore the two control parameters Temperature ( $T$ ) and Pressure ( $P$ ). Considering nuclear matter, the most convenient thermodynamic potential is the *grand canonical potential*  $\Omega(T, V, \mu_B)$ , where  $\mu_B$  is the baryon chemical potential and  $V$  the volume of the system.  $\Omega$  is the best choice to describe a system in which the number of particles (in our case the number of baryons) may change. Considering as observables only densities, the remaining control parameters are  $T$  and  $\mu_B$ . In Fig. 1.3 the phase diagram of nuclear matter is displayed with its different states of aggregation.

---

<sup>6</sup>A nucleon with a mass of about 938 GeV and a radius of about 0.87 fm yields an energy density of  $0.35 \text{ GeV}/\text{fm}^3$ . The nuclear density is about  $0.15 \text{ GeV}/\text{fm}^3$  indicating that the nucleons are well separated within the nucleus.

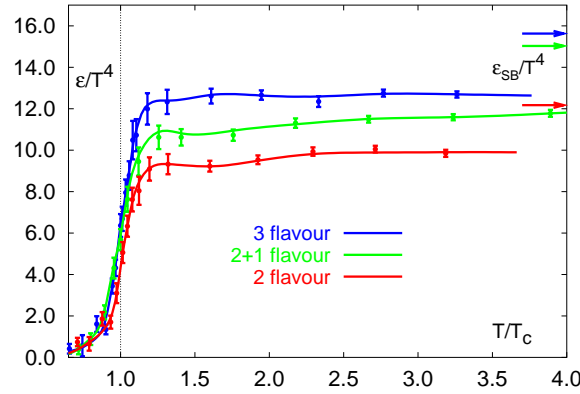


**Figure 1.2:** Lattice QCD calculations of the energy density of nuclear matter as a function of the temperature [10]. The three curves are calculations for different quark masses. 3, 2+1 and 2 flavour means three light quarks, two light+one heavy quark and 2 light quarks, respectively. The arrows denote the Stefan-Boltzmann limits for the different quark configurations.

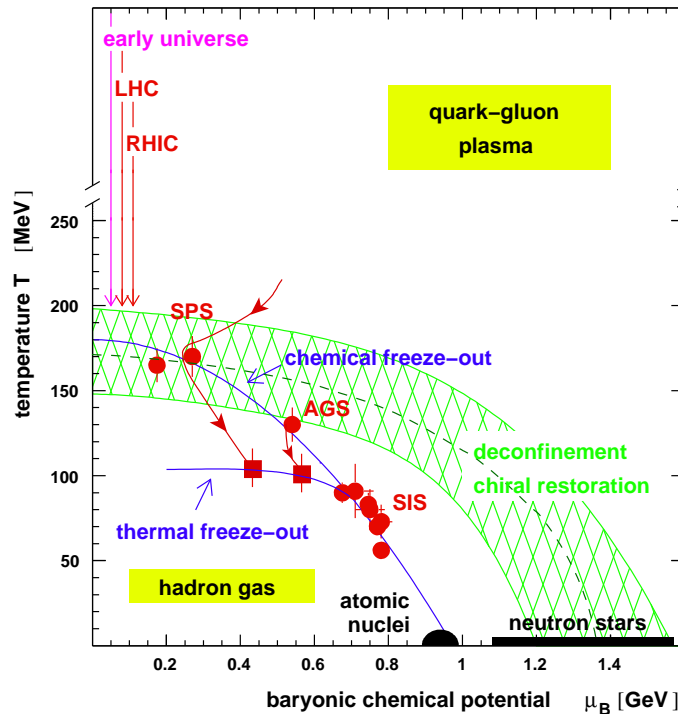


**Figure 1.3:** The phase diagram of QCD [11]

### 1.3 Relativistic Heavy-Ion Collisions

As already mentioned, the QGP may be found in the early universe or in the centre of neutron stars. However neither of these are accessible in the laboratory. Over 30 year ago, in 1975 T.D. Lee suggested that “by using high energy collisions between heavy ions” one may create abnormal states of matter [12]. With particle accelerators a tool is available which allows to realise this suggestion. The first heavy ion collisions heralded a new area of expertise - relativistic heavy ion physics.

The relativistic heavy ion program led to a series of experiments at several particle accelerators. The first experiments have been performed with fixed targets at the Alternating Gradient Synchrotron (AGS) in Brookhaven, USA (starting in mid 1980’s) and the Super Proton Synchrotron (SPS) at CERN, Switzerland (starting late 1980’s). The centre of mass (CM) energies covered by these accelerators is 2 GeV - 17 GeV per nucleon pair. The first colliding heavy ion beams were delivered by the Relativistic Heavy Ion Collider (RHIC) in Brookhaven in 2000 with a CM energy of up to 200 GeV per nucleon pair. In summer 2008 the Large Hadron Collider (LHC) at CERN will deliver the first proton beams and in 2009 the first heavy ion beams. The CM energy for these ion collisions will be 5.5 TeV per nucleon pair.

Heavy ion collisions undergo various stages (see e.g. [13]). In the initial phase, where the nuclei meet, *hard processes* with momentum transfers  $Q^2 \gg 1 \text{ GeV}^2$  take place. Those processes can be calculated by pQCD. The time scale for the production of hard particles is, according to the uncertainty relation,  $\tau_{form} \simeq 1/\sqrt{Q^2}$ , resulting in  $\tau_{form} \simeq 0.1 \text{ fm}/c$  for a 2 GeV particle<sup>7</sup>. Those processes happen before the bulk particle production.

Rescattering of the initially produced quanta produce a *fireball* of dense, strongly interacting matter. If thermalisation happens quickly enough and the energy density is sufficiently high a QGP is formed. The energy in the fireball is available to produce  $q\bar{q}$  pairs. At large enough initial beam energies<sup>8</sup> the mid-rapidity region will be baryon free.

Due to the pressure of the hot system against the surrounding vacuum, the system expands and cools down and the QGP hadronises. If the kinetic energy of the resulting hadrons does not allow inelastic collisions anymore, the particle abundances are fixed. This is called *chemical freeze-out*. The temperature and baryon chemical potential of the system in this state can be obtained using thermal models to fit measured particle abundance ratios (see e.g. [14]). In Fig. 1.3 the resulting  $T$  and  $\mu_B$  from various experiments at different energies are displayed as red circles.

Once the system gets so dilute that also elastic collisions cease one speaks of the *thermal freeze-out* of the system. In this stage the transverse momentum spectra of the produced particles are fixed and show an approximately exponential shape. The spectra reflect the temperature of the system at thermal freeze-out, blue-shifted by the average collective radial expansion (radial flow). Experimental results of the thermal freeze-out parameters are displayed in Fig. 1.3 as red squares.

From the above description it is immediately clear that the QGP is hidden from direct access by the subsequent hadronisation and freeze-out processes. Therefore experimental evidence for the formation of a QGP has to be searched for in its remnants. Several signals have been proposed which indicate the presence of a QGP. Two of the most important are the  $J/\psi$  suppression [15] and the strangeness enhancement [16].

<sup>7</sup>A useful conversion factor is  $1 \text{ fm}/c \simeq (200 \text{ MeV})^{-1}$

<sup>8</sup>This is the case if the energy loss of the colliding beam particles is small compared to their initial energy.

## 1.4 Outline of this Thesis

In heavy ion collisions at LHC energies about five thousand<sup>9</sup> charged particles will emerge into the acceptance of the central detector system ( $|\eta| \leq 0.9$ ) of ALICE which have to be detected simultaneously.

To exhaust the intrinsic resolution of the detectors a detailed understanding of their performance and a precise calibration are essential.

The present work concentrates on the commissioning and calibration<sup>10</sup> of the main tracking device of ALICE, a large volume Time Projection Chamber (TPC).

In the following chapter a short overview of the ALICE detector system will be given, while in chapter 3 the TPC will be described in detail. Chapter 4 describes the first commissioning of the TPC on surface level and presents results from the first measurements. In chapter 5 results of measurements of the electronics noise of the TPC in its final position are presented and discussed. The calibration algorithms which have been developed in the course of the data analysis are described in appendix A.

---

<sup>9</sup>This value is derived from the expected charged particle pseudorapidity density of  $dN_{ch}/d\eta \approx 2000$

<sup>10</sup>with respect to electronics response, geometrical alignment and electron drift properties



## 2 A Large Ion Collider Experiment

ALICE [17, 18] is the dedicated heavy ion experiment at the Large Hadron Collider (LHC) at CERN. Its primary task is to study the physics of strongly interacting matter and the quark gluon plasma in nucleus-nucleus collisions at centre of mass energies up to 5.5 TeV per nucleon pair.

The complete ALICE detector system was designed to cope with particle multiplicities as high as  $dN_{ch}/d\eta \approx 8000$ , which were anticipated for Pb-Pb collisions at the above mentioned energy.

ALICE consists of a central part, placed in a large 0.5 T solenoid (L3 magnet), a forward muon spectrometer and several smaller detectors in the forward region. The detector system is displayed in fig. 2.1.

The central part can be divided into the ‘central barrel detectors’ (ITS, TPC, TRD, TOF), covering at full acceptance a pseudo rapidity range of  $|\eta| < 0.9$  over the full azimuth and three single-arm detectors (HMPID, EMCal, PHOS) with smaller azimuthal and polar acceptance. The muon arm covers a range of  $2.5 < \eta < 4$ .

ALICE has unique possibilities in particle identification (PID). Fig. 2.2 shows the PID performance of the experiment as a function of the momentum in terms of several particle ratios. Solid bars mark regions of a separation better than  $3\sigma$ , dashed regions of better than  $2\sigma$ .

Combining measurements in the central part with data from the Forward Multiplicity Detector, a large range in pseudorapidity of up to  $-4.5 \leq \eta \leq 5$  is covered, enabling to measure the charged particle pseudorapidity density in an interval of about eight units of rapidity.

In the following a short description of all detectors is given. At the end of the chapter the two coordinate systems commonly used within ALICE are introduced.

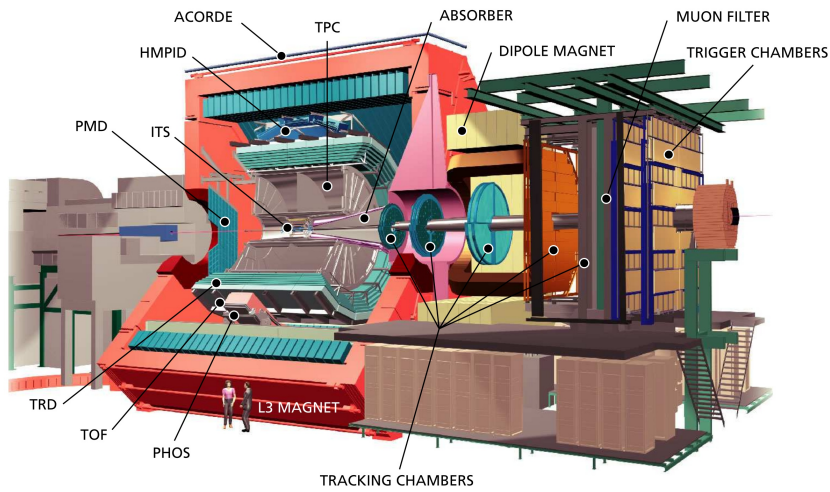


**Figure 2.1:** *The ALICE detector system [17]. Not labeled are the forward detectors (T0, V0, FMD). The EMCal is not yet present in this illustration and HMPID is not in the correct position.*

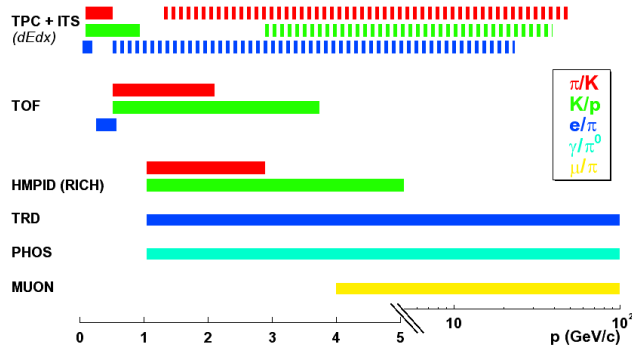


**Figure 2.2:** *ALICE PID performance as a function of momentum in terms of particle ratios. Solid bars mark regions of a separation better than  $3\sigma$ , dashed regions of better than  $2\sigma$ .*

## 2.1 Detectors

### 2.1.1 Central barrel

#### The Inner Tracking System (ITS)

Primary goals of the ITS [19] are the determination of the primary collision vertex and secondary vertices necessary for the reconstruction of charm and hyperon decays. Further it should provide tracking and identification of low momentum particles not reaching the TPC and improve the momentum and angular resolution of particles measured within the TPC.

The ITS is built up of six layers of silicon detectors at radii between 4 cm and 44 cm. The two innermost layers are silicon pixel detectors (SPD), the two middle layers silicon drift (SDD) and the two outer layers are equipped with double-sided silicon microstrip detectors (SSD). The outer four layers have an analogue readout allowing for particle identification via their specific energy loss ( $dE/dx$ ) in the  $1/\beta^2$  region<sup>1</sup>.

In Pb-Pb collisions the primary vertex can be determined with a precision of about 5  $\mu\text{m}$  in the beam direction and about 25  $\mu\text{m}$  in transverse direction. For p-p collisions the precision is about an order of magnitude worse due to the much lower number of tracks. Including the primary vertex resolution the track impact parameter can be measured with a precision of 50  $\mu\text{m}$  and 100  $\mu\text{m}$  in Pb-Pb and p-p collisions, respectively (ITS + TPC at 1 GeV/c).

#### The Time Projection Chamber (TPC)

The TPC [20] is the main tracking device in ALICE. A detailed description is given in chapter 3. It has an active volume of  $\approx 88 \text{ m}^3$  filled with a gas mixture of Ne-CO<sub>2</sub>-N<sub>2</sub> in proportions 90-10-5. In radial direction it reaches from  $\approx 80 \text{ cm}$  to 250 cm with an overall length of 500 cm.

A central HV electrode divides the drift volume into two readout sides. Each endcap is instrumented with  $2 \times 18$  multi-wire proportional readout chambers with a total active area of 32.5 m<sup>2</sup>, segmented into 557568 readout pads.

The efficiency of the TPC track finding software is close to 100 % for particles with  $p_t$  above 0.2 GeV/c. Due to particle decays and the dead zones in the TPC, its physical track

<sup>1</sup>For a discussion of the  $dE/dx$  measurement see section 3.2.1.



finding efficiency is about 80 %, increasing up to 90 % for particles with  $p_t$  above 1 GeV/c. The momentum and  $dE/dx$  resolution vary slightly with the event multiplicity, reaching values of 0.7 % and 6 %, respectively, at  $p_t = 1$  GeV and  $B = 0.5$  T.

### The Transition Radiation Detector (TRD)

With the help of the TRD [21] the electron identification in the central barrel can be improved significantly for particles with momenta larger than 1 GeV/c. At higher energies the pion rejection in the TPC using the energy loss information is no longer sufficient.

Six layers of TRD chambers with a fivefold segmentation in  $z$  direction surround the TPC at radii between  $2.9 < r < 3.7$  m. 30 chambers each are grouped in 18 ‘super-modules’ in azimuthal direction.

Combining the transition radiation signal information of all six layers a pion rejection of the order of 100 at 90 % electron efficiency is reached for particles at 2 GeV/c. In addition the specific energy loss  $dE/dx$  of the particles is measured, supplementing the information from the TPC.

### The Time Of Flight detector (TOF)

Using as a complementary method the flight time of a particle, the TOF [22] helps to substantially improve the particle identification capabilities of ALICE in a momentum range between about 0.5 and 2.5 GeV.

The TOF array surrounds the TRD modules at radii between 3.7 and 4 m. Multi-gap Resistive Plate Chambers (MRPC) are used for the TOF detector, which allow for an overall time resolution of 80 ps. With this excellent resolution a  $\pi/K$  and  $K/p$  separation better than 3 sigma is achieved for track momenta up to 2.5 GeV and 4 GeV, respectively.

## 2.1.2 Central single-arm Detectors

### The High Momentum Particle Identification detector (HMPID)

The HMPID [23], a Ring Imaging Cherenkov detector (RICH), is devoted to the identification of high momentum particles ( $\approx 1$  to 5 GeV/c).

It is placed at a distance of about 5 m to the beam axis, covering a polar angle of  $\approx 54^\circ$  and  $57^\circ$  in azimuth, respectively. This corresponds to about 5 % of the ALICE central barrel acceptance.

### The Photon Spectrometer (PHOS)

PHOS [24], an electromagnetic calorimeter, is optimised for measuring photons (of  $\approx 0.5$  - 10 GeV/c),  $\pi^0$  (of  $\approx 1$  - 10 GeV/c) and  $\eta$  mesons (of  $\approx 2$  - 10 GeV/c).

It is positioned at the bottom in the ALICE setup, covering the pseudo rapidity range of  $-0.12 \leq \eta \leq 0.12$  and  $100^\circ$  in azimuth. The calorimeter is build of lead-tungstate crystals and has 17280 readout channels.

### The Electromagnetic Calorimeter (EMCal)

The addition of the EMCal [25] to the ALICE setup enhances the capabilities for jet quenching studies. It improves the jet energy resolution as well as the measurement of high momentum photons and electrons. The possibility to trigger on high energy jets is also opened.

The full detector, which is segmented into 12672 towers of layered Pb-scintillator, spans  $-0.7 \leq \eta \leq 0.7$  in pseudo rapidity and  $110^\circ$  in azimuth. It is placed at a distance of  $\approx 5$  m from the beam pipe.

### 2.1.3 Forward Region

#### The Di-muon Forward Spectrometer

The Muon Spectrometer [26] is dedicated to the analysis of heavy quark vector mesons ( $J/\Psi$ ,  $\Psi'$ ,  $\Upsilon$ ,  $\Upsilon'$ ,  $\Upsilon''$ ) via their decay in the di-muon channel. To separate all resonance states the mass resolution at around 10 GeV is better than 100 MeV.

It consists of a front absorber which absorbs the hadrons and photons from the interaction vertex, a system of 10 cathode pad chambers with a resolution better than 100  $\mu\text{m}$  for tracking, a large 3 Tm dipole magnet and a passive muon filter wall followed by four planes of resistive plate chambers for triggering. In addition the beam line is shielded to protect the chambers from particles produced at large rapidities and their secondaries. The covered acceptance range is  $2.4 \leq \eta \leq 4$ .

#### The Zero Degree Calorimeter (ZDC)

One essential measure in heavy-ion collisions is the event-by-event determination of the collision centrality. The ZDC [27] allows for measuring this quantity and can be used as a fast trigger to enhance the sample of central collisions.

Due to the beam optics (separation dipoles) the collision spectators are split, separating neutrons and protons. Therefore two types of calorimeters are needed. One set each is placed at a distance of about 116 m on both side of the interaction point. The neutron ZDCs are placed between the two beam axis, while the proton ZDCs are centred at a distance of 19 cm. For central events the energy resolution of the ZDC system is better than 10 %.

#### The Forward Detectors (T0, V0, FMD)

On both sides of the interaction point (IP) one of the detectors T0, V0 and FMD [28] is placed, which are needed for triggering purposes.

The Time0 detector (T0) provides fast timing signals used in the Level 0 (L0) trigger. It covers a pseudorapidity range of  $-3.3 \leq \eta \leq -2.9$  and  $4.5 \leq \eta \leq 5$ . Its time resolution is better than 50 ps and the trigger efficiency varies from about 50 % in pp up to 100 % for A-A collisions. In addition T0 gives a fast evaluation of the multiplicity in A-A collision.

The Vertex0 detector (V0) provides the on-line L0 centrality/multiplicity trigger. In addition it provides background rejection for the di-muon spectrometer and contributes to the rejection of beam-gas interactions. The detectors are segmented into eight plastic scintillator pads and cover approximately the same pseudorapidity range as the FMD.

The Forward Multiplicity Detector (FMD) is used in the off-line determination of event multiplicity. It consists of 51200 silicon strip channels. Due to a readout time of  $\approx 13 \mu\text{s}$  it can only be used at the L2 trigger level or above. The covered pseudorapidity range is  $-3.4 \leq \eta \leq -1.2$  and  $1.7 \leq \eta \leq 5.0$ . Together with the SPD from the ITS, the FMD allows to measure charged particle multiplicities in the range  $-3.4 \leq \eta \leq 5.0$ , with some overlap regions, providing redundancy.

#### The Photon Multiplicity Detector (PMD)

For the detection of photons, the PMD [29] consists of a preshower detector with a charged particle veto detector in front. Photons passing through the converter of the detector make a shower and produce signals in several of the  $\approx 2 \cdot 10^5$  cells. Hadrons normally affect only one cell and can be rejected.

The PMD has an acceptance of  $1.8 \leq \eta \leq 2.6$ . It allows to measure the  $N_\gamma/N_{\text{ch}}$  ratio on an event-by-event basis.

## 2.2 Coordinate Systems

### 2.2.1 Global Coordinate System

The global ALICE coordinate system [30] is a right handed orthogonal cartesian system which has its origin at the beam interaction point.

Its  **$z$ -axis** is parallel to the mean beam direction, pointing towards the ‘A-Side’, away from the muon arm. This side is also called Shaft- or RB24-Side. The opposite side (negative  $z$  values) is called C-Side, or also Muon- or RB26-Side.

The  **$x$ -axis** is lying in the local horizontal accelerator plane, pointing towards the centre of the LHC ring. The side with positive  $x$  values is also called I-Side (inner), the opposite side correspondingly O-Side (outer).

The  **$y$ -axis** is chosen to define a right handed system, thus pointing upwards.

The **azimuthal angle  $\phi$**  is increasing counterclockwise, starting from the  $x$ -axis ( $\phi = 0$ ) and looking from the A-Side towards the C-Side.

The **polar angle  $\theta$**  is increasing from the  $z$ -axis towards the  $xy$ -plane.

A sketch of the global coordinate system is given in figure 2.3a.

### 2.2.2 Local Coordinate System

To account for the azimuthal segmentation of the central barrel detectors the reconstruction software uses a local coordinate system [18] related to a given sub-detector (TPC sector, ITS module etc.). The local coordinate system is as the global a right handed cartesian system. Both have the same origin and  $z$ -axis. The local system is rotated such that the  $x$ -axis is perpendicular to the sub-detectors ‘sensitive plane’ (TPC pad row, ITS ladder etc.). Therefore the local and global system can be transformed into each other by a simple rotation of the angle  $\alpha$  around the  $z$ -axis.

A sketch of the local coordinate system is given in figure 2.3b.

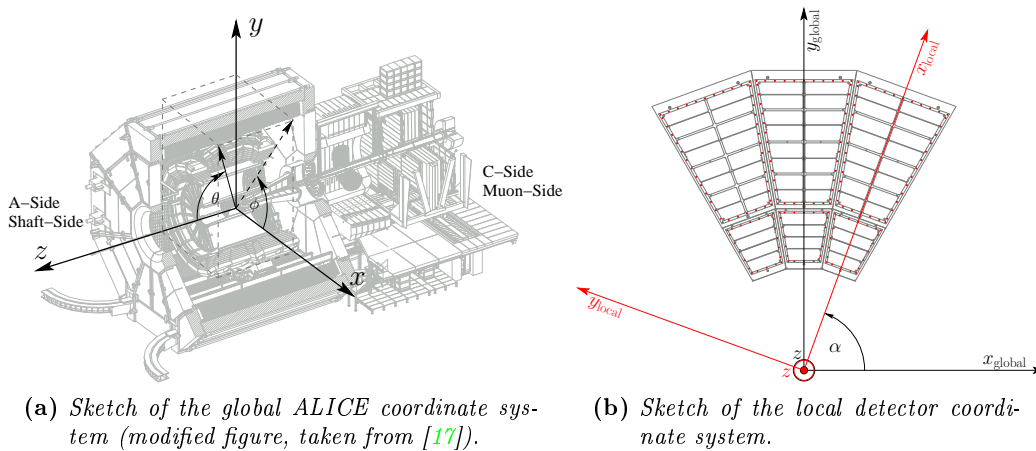


**Figure 2.3:** ALICE coordinate systems.



### 3 The Alice TPC

The main tracking device of the ALICE experiment is a large volume ( $\approx 88 \text{ m}^3$ ), cylindrical **T**ime **P**rojection **C**hamber (TPC) [20]. The choice of the gas mixture (Ne-CO<sub>2</sub>-N<sub>2</sub>) implies a non-saturated drift velocity at the nominal drift field (400 V/cm). The consequence is that a temperature stability and homogeneity of  $\Delta T < 0.1^\circ\text{C}$  is required in order to exhaust the intrinsic detector resolution.

The main performance goals that entered in the design considerations are a  $dE/dx$  resolution better than 8%, a relative  $p_t$  resolution better than 1% for momenta below 2 GeV/c and still better than 2.5% for momenta of 4 GeV/c and a two track resolution capable of separating tracks with a relative momentum difference of  $< 5 \text{ MeV}$ .

At the time when the design phase started, the maximum anticipated multiplicity in Pb-Pb collisions at LHC energies was  $dN_{ch}/d\eta = 8000$  at midrapidity, resulting in about 20000 charged primary and secondary particles in the TPC acceptance. This number dictated the granularity of the detector.

The readout is done using multiwire proportional chambers with a segmented cathode plane. The TPC is separated by a central electrode (CE) into two drift regions of 2.5 m length. A schematic picture is displayed in Fig. 3.1.

In the following the functional principle, involved physics processes, the technical design as well as supply and calibration systems of the detector will be described.

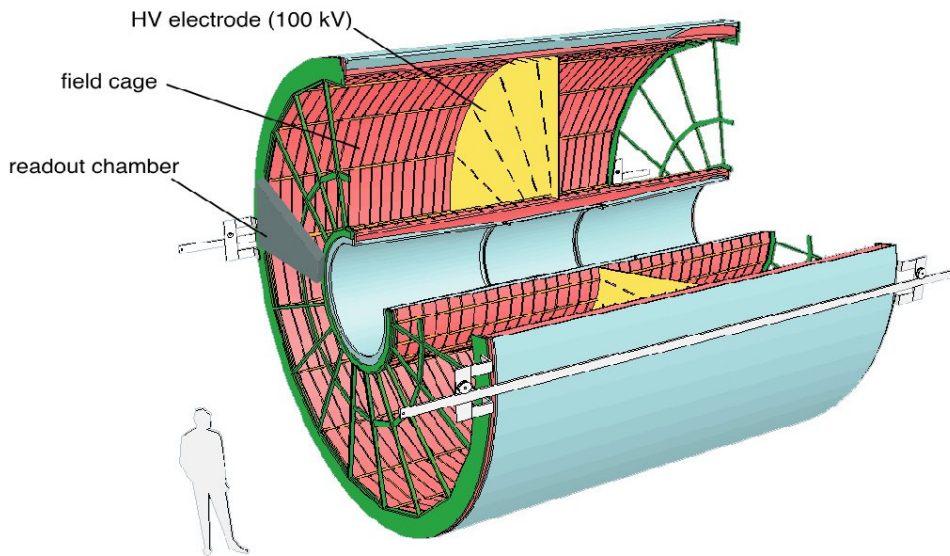


**Figure 3.1:** *View of the TPC*

### 3.1 Functional Principle

Fast charged particles traversing a gas leave a trace of ionisation along their flight path. A TPC is a particle detector which allows for the three dimensional reconstruction of such particle *tracks*. The ionisation electrons drift in an electric fields towards a readout plane, where the projection of the track is measured. Together with the *drift time* information of the electron *clusters* a reconstruction software calculates the origin of the ionisation as three dimensional *space points*. A tracking algorithm afterwards combines the space points to reconstruct the particle trajectories. To be able to measure the momentum and charge of the particles the TPC is placed in a magnetic field. The momentum can then be deduced from the bending radius of the particle trajectory. In the chosen setup electric and magnetic field lines are parallel. The measurement of the mean energy loss per track length  $\langle dE/dx \rangle$  together with the known momentum allows for an identification of the particle (see Sec. 3.2.1).

The TPC has two main components: a *field cage* providing the electric field in which the electron tracks drift towards the *readout detector*, which is the second main component. Both components are placed in a gas tight volume which separates the detector gas from the environment. A sketch of the basic structure of one TPC half is displayed in Fig. 3.2.

The detector gas serves as the ionisation and drift medium for the electrons, but also determines the gas amplification in the readout chambers (see following sections). The exact choice of the gas mixture is therefore extremely crucial for the performance of the detector.

The field cage (FC) is comprised of a high voltage electrode and the readout chambers which build the opposite electrode (0 V). To provide for a sufficiently homogeneous field the active volume is surrounded by *field strips*. A resistor network degrades the potential on the field strips.

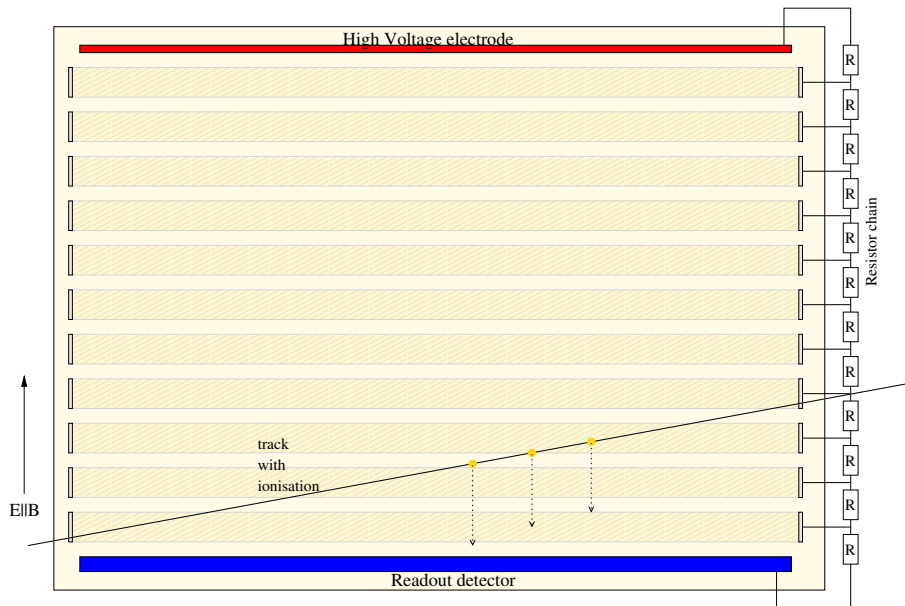
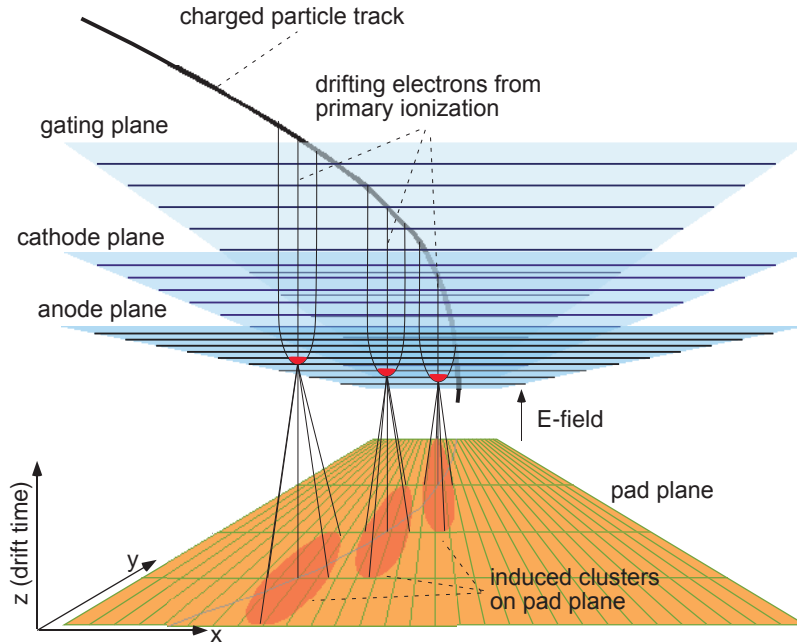


Figure 3.2: Basic structure of a TPC



**Figure 3.3:** Sketch of a multiwire proportional chamber with segmented cathod pads

For the readout multiwire proportional chambers (MWPC) with a segmented cathode plane (*pad plane*) are used. Three wire planes are mounted above the pad plane (see Fig. 3.3) which are called anode (or sense wire) plane, cathode plane and gating plane (or gating grid). A detailed description of the readout chambers can be found in section 3.3.4.

The amplification region is defined by the pad plane, the anode wires and the cathode wires. By gas amplification (see Sec. 3.2.4) the original charge is multiplied by a factor of about  $2 \times 10^4$ . The produced charge induces a signal on the pad plane. The wire geometry is chosen such that on average the signal spreads over three adjacent pads. Determining the centre of gravity of the charge distribution therefore allows for a position resolution much better than the actual pad size.

The gating grid, separating the MWPC from the drift region, can be switched between two modes: closed and open. In the open mode all wires have the same voltage, which is defined by the potential of the drift field at the place of the gating grid. The wires in this case do not influence the field and the grid is transparent for charges drifting either from the drift region towards the MWPC or from the amplification region into the drift region. A permanently open grid (or its absence) has the obvious disadvantage that all ionising events, being of interest or not, will cause gas amplification, resulting in the production of ions. With an open gating grid the produced ions would drift towards the CE, accumulate in the drift volume (ion-feedback) and cause field distortions. To avoid this, the gating grid is closed by default and only opened in case of a triggered event. The opening duration is given by the time the ionisation electrons need to drift over the full TPC length ( $\approx 92 \mu\text{s}$ ). In the closed mode the wires of the gating grid are set alternating to a positive and negative voltage. In this case the drift lines of positive and negative charges end on the gating grid wires.

## 3.2 Physics Processes

### 3.2.1 Energy Loss of Charged Particles in Gases

The mean differential energy loss of fast charged particles due to coulomb interactions with the traversed medium can be expressed by formula 3.1[31], which was derived by Bethe and Bloch in the framework of relativistic quantum mechanics.  $N$  is the Avogadro number,  $m$  and  $e$  are the electron mass and charge,  $Z$ ,  $A$  and  $\rho$  are the atomic number, mass and density of the medium and  $I$  is its effective ionisation potential;  $z$  and  $\beta$  describe charge and velocity (in units of the speed of light) of the projectile.  $\delta(\beta)$  is a correction term to account for the *density effect* (see below).

$$\left\langle \frac{dE}{dx} \right\rangle = \frac{4\pi N\rho Z}{mc^2} \frac{1}{A\beta^2} z^2 \left( \ln \frac{2mc^2}{I} \beta^2 \gamma^2 - \beta^2 - \frac{\delta(\beta)}{2} \right) \quad (3.1)$$

Formula 3.1 shows that the energy loss is not depending on the mass of the particle, but only on its velocity  $\beta$ . Fig. 3.4 shows the energy loss  $dE/dx$  measured as a function of the particle momentum (each point corresponds to a measured particle) as well as the description with the Bethe-Bloch formula (solid lines) for different particle species. For low velocities the energy loss is steeply decreasing, which is described by the  $1/\beta^2$  term. Around  $\beta \approx 0.97$  the ionisation reaches a minimum. Particles in this region are called *minimum ionising particles* (MIP). Towards higher velocities the  $\ln \beta^2$  term starts to dominate, resulting in the *relativistic rise*. This rise, however, does not continue to indefinitely large values, but saturates and ends in the *Fermi plateau*. Fermi calculated the ‘density effect’ as a coherent effect of the surrounding polarisable atoms, which shield the field of the travelling particle [31]. It is accounted for by the  $\delta(\beta)$  term in the Bethe-Bloch formula. Parameter descriptions for this term have been worked out by Sternheimer and others.

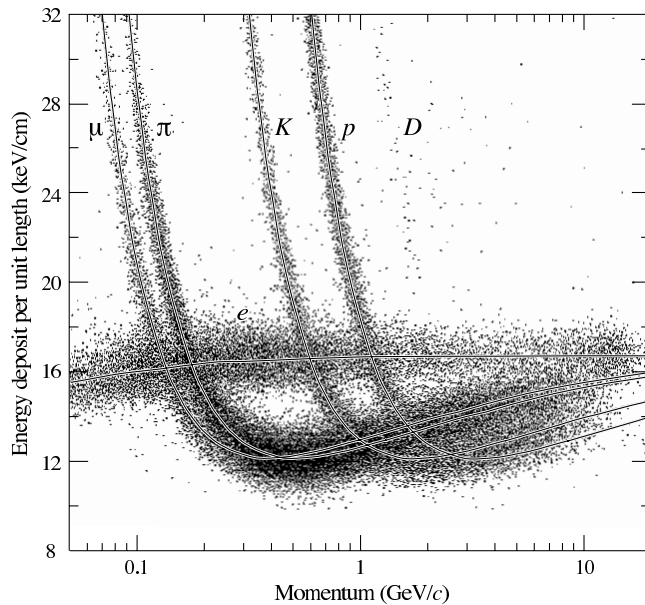


**Figure 3.4:** Energy loss of fast charged particles as a function of their momentum [32]

Particles can be identified by determining the minimum distance to one of the curves.



Obviously the individual PID becomes problematic once the curves begin to overlap. In these regions complementary methods have to be used in addition, e.g., the TOF detector.

### 3.2.2 Two Photon Ionisation using UV Lasers

For calibration purposes a pulsed UV lasers is used to simulate straight ionising tracks in the active volume of the TPC (see Sec. 3.4.1). The laser used has a wavelengths of 266 nm yielding an energy of 4.66 eV. The ionisation potential of the gases used in the TPC, however, is much larger (Ne:  $\approx 22$  - CO<sub>2</sub>:  $\approx 14$  - N<sub>2</sub>:  $\approx 16$ ; all in eV). Obviously not even two photon processes happen to be able to ionise these gases. More than two photon processes on the other hand have a negligible probability to occur. The molecules taking part in the ionisation process are organic impurities in the gas with typical ionisation potentials of 5-8 eV, at a concentration of the order of 1 ppm. Those can be ionised in a two photon process.

A scheme of the transition rates involved in a two step process is given in Fig. 3.5. The rate equations can be written in the following form [31]:

$$\begin{aligned} P_0'(t) &= -k_1 P_0(t) + (k_1 + k_2) P_1(t), \\ P_1'(t) &= +k_1 P_0(t) - (k_1 + k_2 + k_3 + k_4) P_1(t), \\ P_2'(t) &= k_4 P_1(t), \end{aligned} \quad (3.2)$$

where the primes denote time derivatives,  $P_0$ ,  $P_1$  and  $P_2$  are the population densities of the levels and  $k_1 - k_4$  are the transition rates.

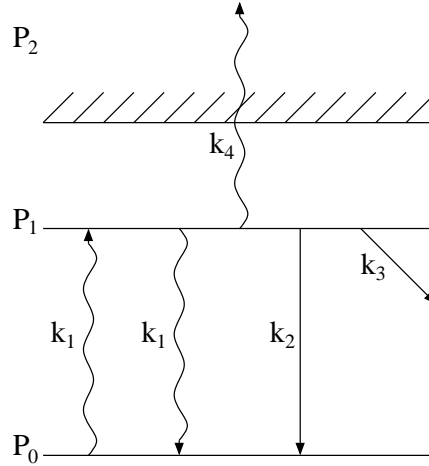


**Figure 3.5:** Transition scheme for the two photon ionisation process

The stimulated transitions  $k_1$  and  $k_4$  are taken to be proportional to the incoming photon flux  $\phi$ , where the constant of proportionality is the respective transition cross-section  $0 \rightarrow 1$  and  $1 \rightarrow 2$ :

$$\begin{aligned} k_1 &= \sigma_{01} \phi \\ k_4 &= \sigma_{12} \phi \end{aligned} \quad (3.3)$$

Under the assumption that during a laser pulse  $P_1(t) \ll P_0(t)$ , implying an excitation of only a fraction of the molecules under consideration, we can set  $P_0(t) = P_0$  to be constant.

This is true if the rate  $k_1$  of the transition  $0 \rightarrow 1$  is small compared with the total rate  $\sum k = k_1 + k_2 + k_3 + k_4$  of transitions from state 1 to other states:  $k_1 = \sigma_{01}\phi \ll \sum k$ .

With this approximation we can solve the second equation of 3.2 and insert it into the third:

$$P_2'(t) = k_4 P_1(t) = \frac{k_1 k_4 P_0}{\sum k} \left(1 - e^{-t \sum k}\right) \quad (3.4)$$

Integration of the above equation over a pulse length  $T$  yields a ionisation density of

$$P_2(T) = \frac{k_1 k_4 P_0}{\sum k} \left(T - (1 - e^{-T \sum k}) / \sum k\right). \quad (3.5)$$

For short laser pulses ( $T \ll 1/\sum k$ ) it is appropriate to expand the exponential function up to second order, resulting in

$$P_2(T) = \frac{1}{2} k_1 k_4 P_0 T^2 = \frac{1}{2} \sigma_{01} \sigma_{12} P_0 \phi^2 T^2, \quad (3.6)$$

where equations (3.3) have been used in the last step.

This result shows, that for constant laser pulse durations, the ionisation rate  $P_2$  is proportional to the square of the photon flux  $\phi^2$ . Therefore it is preferable to use lasers with a high stability in the intensity to obtain a constant ionisation rate.

### 3.2.3 Drift Properties of Electrons in Gases

#### 3.2.3.1 Drift Velocity

In a macroscopic picture the drift of charged particles in a medium under the influence of an electric and magnetic field can be expressed by an equation of motion with a friction term [31]:

$$m \frac{d\mathbf{u}}{dt} = e\mathbf{E} + e[\mathbf{u} \times \mathbf{B}] - K\mathbf{u}, \quad (3.7)$$

where  $m$  and  $e$  are the mass and charge of the particle with the velocity vector  $\mathbf{u}$  experiencing the friction  $K$  in the traversed medium.

The ratio  $m/K$  has the dimension of a time and can be interpreted as the average time between collisions  $\tau$ :

$$\tau = \frac{m}{K} \quad (3.8)$$

For  $t \gg \tau$  a constant drift velocity  $\mathbf{u}$  is observed, which means  $d\mathbf{u}/dt = 0$ . The corresponding equations for the drift velocity that follows from 3.7 is:

$$\frac{\mathbf{u}}{\tau} \frac{e}{m} - [\mathbf{u} \times \mathbf{B}] = \frac{e}{m} \mathbf{E} \quad (3.9)$$

Introducing the cyclotron frequency  $\boldsymbol{\omega} = (e/m)\mathbf{B}$  and  $\boldsymbol{\varepsilon} = (e/m)\mathbf{E}$ , equation 3.9 can be written in terms of a matrix equation which reads

$$M\mathbf{u} = \boldsymbol{\varepsilon}, \quad M = \begin{bmatrix} 1/\tau & -\omega_z & \omega_y \\ \omega_z & 1/\tau & -\omega_x \\ -\omega_y & \omega_x & 1/\tau \end{bmatrix}. \quad (3.10)$$

The solution of 3.10 is then obtained by inverting  $M$ :

$$\mathbf{u} = M^{-1}\boldsymbol{\varepsilon} \quad (3.11)$$


---

Equation 3.11 can be written as:

$$\mathbf{u} = \frac{e}{m}\tau|\mathbf{E}|\frac{1}{1+\omega^2\tau^2}(\hat{\mathbf{E}} + \omega\tau[\hat{\mathbf{E}} \times \hat{\mathbf{B}}] + \omega^2\tau^2(\hat{\mathbf{E}} \cdot \hat{\mathbf{B}})\hat{\mathbf{B}}), \quad (3.12)$$

where  $\hat{\mathbf{E}}$  and  $\hat{\mathbf{B}}$  denote the unit vectors in the direction of the fields. Eqn. (3.12) implies that changes in the drift velocity caused by the magnetic field are governed by the quantity  $\omega\tau$ . This equation also shows, that by changing the polarity of the magnetic field only the term proportional to  $\omega\tau$  changes its sign, while the one proportional to  $\omega^2\tau^2$  does not.

In the case of  $\mathbf{B} = \mathbf{0}$  the above equation reads:

$$\begin{aligned} \mathbf{u} &= \frac{e}{m}\tau\mathbf{E} = \mu\mathbf{E}, \\ \mu &= \frac{e}{m}\tau \end{aligned} \quad (3.13)$$

where  $\mu$  is called the electron mobility.

### 3.2.3.2 $\mathbf{E} \times \mathbf{B}$ Effect

Equation 3.12 shows that as soon as the magnetic field is not parallel to the electric field, the drift velocity vector is not anymore parallel to  $\mathbf{E}$ . This results in a displacement of the measured track with respect to the unaffected one. The effect is called the  $E \times B$  effect. Under a reversal of the magnetic field only the  $E \times B$  term changes sign, or in other words the term proportional to  $\omega\tau$ .

In the case where  $\mathbf{E}$  and  $\mathbf{B}$  are almost parallel, using equation 3.12 and  $\mathbf{E} = (0, 0, E_z)$ ,  $\mathbf{B} = (B_x, B_y, B_z)$  with  $|B_x|, |B_y| \ll |B_z|$  one finds the following ratios of the drift velocity components:

$$\begin{aligned} \frac{u_x}{u_z} &= \frac{-\omega\tau B_y + \omega^2\tau^2 B_x}{(1 + \omega^2\tau^2)B_z} \\ \frac{u_y}{u_z} &= \frac{\omega\tau B_x + \omega^2\tau^2 B_y}{(1 + \omega^2\tau^2)B_z} \end{aligned} \quad (3.14)$$

Over a drift length  $L$  this gives rise to displacements in  $x$  and  $y$  of the size  $\delta_x = Lu_x/u_z$  and  $\delta_y = Lu_y/u_z$ . With equation 3.14 this yields

$$\begin{aligned} \delta_x &= L\left(\alpha_x \frac{\omega^2\tau^2}{1 + \omega^2\tau^2} - \alpha_y \frac{\omega\tau}{1 + \omega^2\tau^2}\right) = (\Delta_x^S + \Delta_x^A) \\ \delta_y &= L\left(\alpha_x \frac{\omega\tau}{1 + \omega^2\tau^2} + \alpha_y \frac{\omega^2\tau^2}{1 + \omega^2\tau^2}\right) = (\Delta_y^A + \Delta_y^S) \end{aligned} \quad (3.15)$$

with  $\alpha_x = B_x/B_z$  and  $\alpha_y = B_y/B_z$ .  $S$  and  $A$  denote the symmetric and antisymmetric part of the equation. The different contributions can be separated by reversing the magnetic field, changing the sign of terms proportional to  $\omega\tau$  (see above):

$$\Delta^S = \frac{1}{2}[\delta(B) + \delta(-B)], \quad \Delta^A = \frac{1}{2}[\delta(B) - \delta(-B)] \quad (3.16)$$

This holds for both the  $x$  and  $y$  displacements.

To correct for this effect it is therefore essential to carry out measurements at the desired magnetic fields and also the reversed fields. The measurements are done preferably with laser tracks, since they have known fixed positions and the statistical error can be practically eliminated. Therefore by comparing results from laser tracks taken with and without magnetic field a measurement of  $E \times B$  effects can be performed.

### 3.2.3.3 Diffusion

Without electromagnetic fields electrons produced in an ionising collision quickly lose their initial energy in multiple collisions with the gas molecules and thermalise. Their average energy is then given by  $\varepsilon_T = 3/2kT$ . A pointlike electron cloud starting to diffuse at  $t = 0$  at the origin of the coordinate system will spread isotropically and assumes after the time  $t$  has elapsed the gaussian density distribution

$$n(r, t) = \left( \frac{1}{\sqrt{4\pi Dt}} \right)^3 \exp\left(-\frac{r^2}{4Dt}\right), \quad (3.17)$$

with  $r$  the distance to the origin and  $D$  the *diffusion constant*.

An electric field breaks the isotropy of eqn. 3.17. It can be shown, that if the collision rate is a function of the electron energy, the drifting electrons assume different mobilities in the leading edge, trailing edge and centre of the cloud [33]. Therefore the diffusion in drift direction and perpendicular to it are different and (3.17) has to be modified accordingly:

$$n(x, y, t) = \left( \frac{1}{\sqrt{4\pi D_l t}} \right) \left( \frac{1}{\sqrt{4\pi D_t t}} \right)^2 \exp\left[-\frac{x^2 + y^2}{4D_t t} - \frac{(z - v_D t)^2}{4D_l t}\right], \quad (3.18)$$

where  $D_l$  and  $D_t$  denote the two different diffusion constants in longitudinal and transverse direction;  $v_D$  is the mean drift velocity.

It can be shown, that by averaging over a large number of collisions the diffusion constant can be written as

$$D = \frac{2}{3} \frac{\varepsilon}{m} \tau. \quad (3.19)$$

Introducing the electron mobility ( $\mu = (e/m)\tau$ ) into (3.19), shows a possibility to determine the electron energy by measuring  $D$  and  $\mu$ :

$$\varepsilon = \frac{3De}{2\mu} \quad (3.20)$$

The total energy of an electron is given by  $\varepsilon = \varepsilon_E + \varepsilon_T$ , with  $\varepsilon_E$  being the part gained in the electric field. Therefore the thermal energy  $\varepsilon_T$  sets a lower limit to the total electron energy. Inserting the thermal energy into (3.20) one obtains the *Nernst-Townsend-Formula*:

$$\frac{D}{\mu} = \frac{kT}{e} \quad (3.21)$$

Equation (3.18) shows, that the width of the density distribution  $\sigma$  in one dimension is given by  $\sigma = \sqrt{2Dt}$ . Together with (3.19) and  $L = v_D \cdot t = \mu Et$  the width can be written as

$$\sigma^2 = 2Dt = \frac{2D}{v_D} L = \frac{2D}{\mu E} L = \frac{4\varepsilon}{3eE} L, \quad (3.22)$$

where  $t$  is the drift time of the electrons and  $L$  the length travelled during that time.

The thermal energy sets a lower limit to the width of the distribution which is given by

$$\sigma^2 = \frac{2kT}{eE} L. \quad (3.23)$$

The result was obtained by inserting (3.21) into (3.22) and is called the *thermal limit*.

As a characteristic measure for the diffusion in a gas, the drift length independent quantities

$$D_L = \frac{\sigma_l}{\sqrt{L}} = \sqrt{\frac{2D_l}{\mu E}} \quad \text{and} \quad D_T = \frac{\sigma_t}{\sqrt{L}} = \sqrt{\frac{2D_t}{\mu E}}, \quad (3.24)$$

are used, given in units of  $[\mu\text{m}/\sqrt{\text{cm}}]$ . Fig. 3.6 shows the results of measurements for Ar and Ne gas mixtures with the two different quenching gases  $\text{CH}_4$  and  $\text{CO}_2$ . One can see that the  $\text{CH}_4$  gas mixture have a significantly larger diffusion coefficient. Mixtures with diffusions close to the thermal limit are called *cold gases* others are called *hot gases*. It is obvious that large TPCs need to be operated with cold gases to obtain a high track resolution over the full drift length.

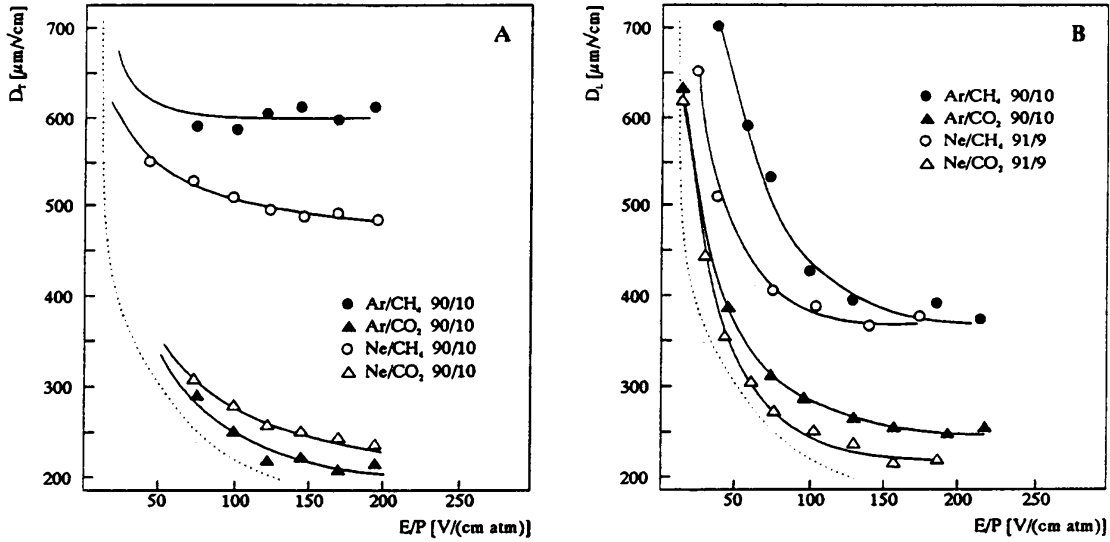


**Figure 3.6:** Transverse (A) and longitudinal (B) diffusion coefficients as a function of the reduced field  $E/P$  for different gas mixtures. The dotted line marks the thermal limit [34].

### 3.2.4 Gas Amplification and Signal Generation

Electrons drifting towards the amplification region see the field

$$E = \frac{\lambda}{2\pi\epsilon_0} \frac{1}{r} \quad (3.25)$$

when approaching one of the anode wires, which has the linear charge density  $\lambda$ . Therefore the field experienced by an electron is increasing with the decreasing distance to the wire. At some point  $r_{L_{min}}$  the energy taken by the electron between collisions is large enough to ionise the gas, producing a second electron. This causes an avalanche to start and the initial charge is amplified by orders of magnitude.

The voltage on the anode wires is chosen such that the produced signal is proportional to the original charge. The proportionality is given as long as the field of the produced ions is negligible compared to that of the wire. This is the case as long as the linear charge density on the wire is much larger than the charge density in the avalanche.

### 3 THE ALICE TPC

In the avalanche not only electrons are produced, but also UV photons, since the relevant cross sections are of the same order of magnitude. A fraction of these photons will be energetic enough to ionise the gas themselves. The situation becomes problematic, if those photons have a mean free path allowing them to loose their energy outside  $r_{Lmin}$ , or to reach the cathode plane and produce photo electrons. In both cases this photon will start a new avalanche which might cause the counter to break down. For this reason a ‘quench gas’ (*quencher*) is needed in the gas mixture. A quencher is a gas of molecules with a large number of rotational and vibrational modes. They have large photoabsorption coefficients over a wide range of wavelength.

Increasing the voltage above the proportional region causes the positive ions produced in the avalanche to start to distort the field close to the wire. Because of the changed field the amplification is not any longer proportional to the initial charge. This is the region of *limited proportionality*. Even higher voltages lead to two different effects, depending on the range photons travel in the medium. If the UV absorption of the quencher is very strong a self quenching streamer occurs (*limited streamer* region). If the photons can travel very far, avalanches are produced all along the full wire and the process can only be stopped by decreasing the wire voltage. This case is called the *Geiger mode*. In both cases the final signal is nearly independent of the initial charge.

The ions produced in the amplification process drift towards the cathode wires. Their field induces a mirror charge on the pads which creates the pad signal. The electrons with their about 1000 times larger drift velocity are immediately after the avalanche process absorbed by the anode wires and do not (or only marginally) participate in the signal creation.

The front end electronics of the TPC (see Sec. 3.3.5) amplifies and shapes the induced signal of each single pad. A schematic drawing is displayed in figure 3.7. The signals of the individual electrons (blue curve) are integrated by the pre-amplifier (dashed magenta curve). Afterwards the shaping circuit performs a differentiation of the signal (red curve).

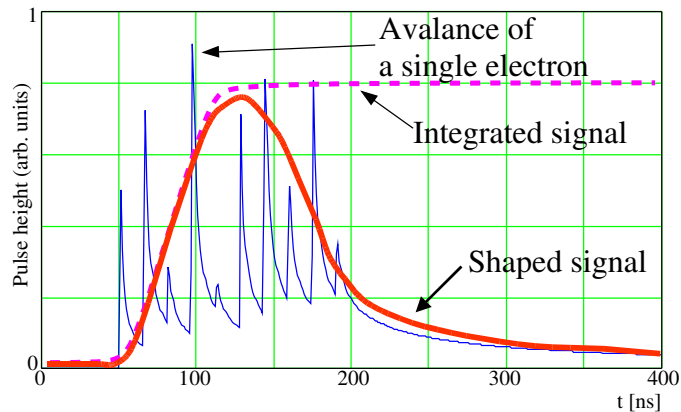


**Figure 3.7:** Sketch of a pad signal. The blue curve shows the signal directly at the pad. The avalanches of each single electron is clearly visible. The magenta curve shows schematically the integrated signal after the pre-amplifier and the red curve shows schematically the shaped (final) signal [35].

### 3.3 Technical Design

#### 3.3.1 Mechanical Structure

In radial direction the TPC is separated from the environment by two 5.1 m long cylinders, called the inner ( $r \approx 0.60$  m) and outer ( $r \approx 2.8$  m) containment vessel. In order to minimise the radiation length in the full acceptance range of the TPC ( $|\eta| < .9$ ) the inner containment vessel has a central part composed of a light weight compound material. The outer parts are made of 3 mm aluminium and widen conically towards the ends ( $r \approx 0.68$  m). Two further cylinders, the inner ( $r \approx 0.80$  m) and outer ( $r \approx 2.58$  m) field cage vessels, confine the active drift volume of the TPC. A side view of the TPC is given in Fig. 3.8.

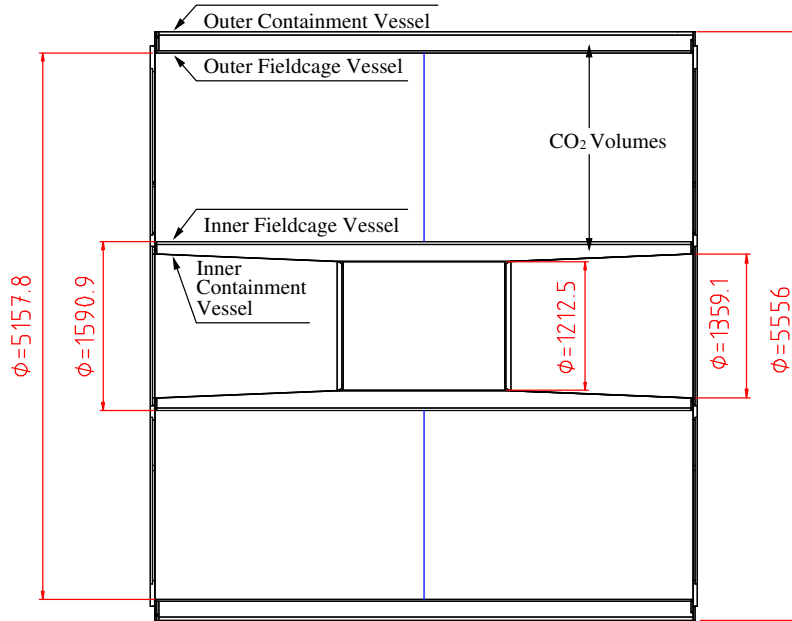


**Figure 3.8:** Side view of the TPC

The space between the containment and field cage cylinders is filled with  $\text{CO}_2$  to provide a good high voltage stability for the field cage (see Sec. 3.3.2). For the same reason the material needs to be a good isolator. To minimise the effect of electron attachment<sup>1</sup> the oxygen and water content have to be kept below 5 and 10 ppm, respectively. Also the gas mixture has to be very stable over time<sup>2</sup> and must not be influenced by the surrounding  $\text{CO}_2$  volume. Therefore high demands in terms of gas tightness are required for the field cage vessels. In addition those cylinders should not evaporate gases which could lead to aging of the readout chambers.

The ends of the TPC are closed by two end-plates, each containing 36 trapezoidal holes: 18 in phi direction, subdivided in two parts in radial direction (see Fig. 3.1). The readout chambers (see Sec. 3.3.4) are mounted into the end-plates.

<sup>1</sup>Electron attachment degrades the physics performance of the detector in terms of position and  $dE/dx$  resolution.

<sup>2</sup>For a Ne- $\text{CO}_2$  [90% - 10%] mixture the  $\text{CO}_2$  needs to be kept within  $(10.000 \pm 0.013)$  % [36]

### 3.3.2 Field Cage and Field Cage Rods

The TPC field cage (FC) is comprised of the central electrode (CE), the field strips which are connected by a voltage divider network and the readout chambers, defining the ground potential. A schematic drawing is given in Fig. 3.9.

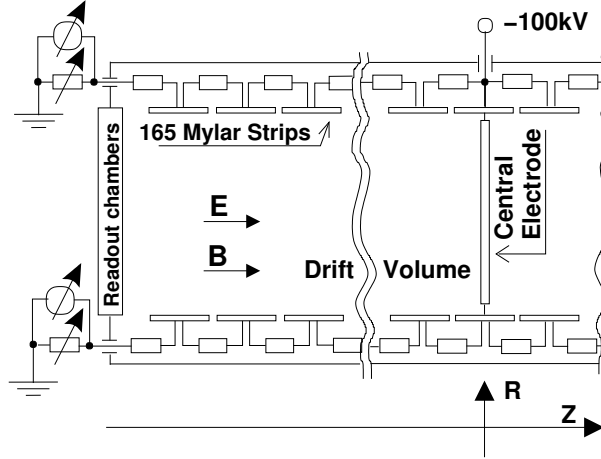


**Figure 3.9:** Schematic drawing of the TPC field cage components

18 rods are installed on each side, close to the inner and outer fieldcage vessel. They are used to keep the field strips in position (see Fig. 3.10). On both sides of the CE 165 strips on the inner and outer part, placed with a precision of  $< 50 \mu\text{m}$ , provide for an electric field homogeneity of  $E_r/E_z < 10^{-4}$  after a distance of a few cm [37], where  $E_r$  and  $E_z$  are the radial and longitudinal component of the E-field. In addition, the parallelism of the central electrode and the readout chambers needs to be better than  $100 \mu\text{m}$ .

The desired drift field of  $400 \text{ V/cm}$  is obtained by applying a voltage of  $100 \text{ kV}$  to the CE. On both readout sides one field cage rod on each of the inner and outer part of the field cage is used to keep a voltage divider<sup>3</sup> ('resistor rods'). The voltage divider degrades the potential such that the centre of each field strip lies on the potential it would have in an ideal field. To increase the high voltage stability, the resistor rods are flushed with  $\text{CO}_2$ .

To maintain electric field distortions below a residual fraction of  $10^{-4}$ , given as overall TPC design constraint, the stability of the currents in the resistor chains have to be kept below this value. Charge produced in the vicinity of the potential strips is absorbed by the strips, thus influencing the current of the voltage divider [38]. Between two field strips a resistance of  $7.5 \text{ M}\Omega$  was chosen. For stability and security reasons two  $15 \text{ M}\Omega$  resistors are connected in parallel. The current of  $80 \mu\text{A}$  resulting from this choice is large enough to satisfy the condition required above.

To avoid the accumulation of static surface charges, the highly insulating walls of the field-cage vessels are equipped with 23 equally spaced potential strips ('guard rings', GR, see Fig. 3.10) which are directly glued to the inner and outer surfaces of the vessels. A resistor chain connects the potential strips to remove charge produced in the containment volumes and close to the walls on the drift volume side of the field cage vessels. The resistance between the rings is  $1000 \text{ M}\Omega$ .

<sup>3</sup>The numbering convention for the FC rods as well as their additional function is displayed in Fig. 3.17



Fig. 3.11 summarises the resistor scheme of one fourth of the field cage (corresponding to one resistor rod). The total resistance of one resistor rod chain is  $1249\text{ M}\Omega$  and in the parallel guard ring chain it is  $11.9\text{ G}\Omega$ . An additional resistance is introduced by the demineralised cooling water of the resistor rod. The overall current of the TPC FC high voltage system resulting from this scheme is  $355\text{ }\mu\text{A}$ . In each chain a last resistor of  $14$  and  $100\text{ k}\Omega$ , respectively, allows for measuring the current in the chain.

The outer field cage strips are mounted on the outside of the rods thus introducing a space between the chambers and strips. To define the potential in this gap and minimise field distortions electrodes (‘skirts’) have been installed between the rods (see inset in figure 3.10). Electrostatic calculations demonstrating the need for the skirts can be found in [39].



Figure 3.10: Picture of the inner field cage rods, field strips and inner containment vessel with guard rings. The inset shows field strips of the outer field cage and the skirts between the rods.

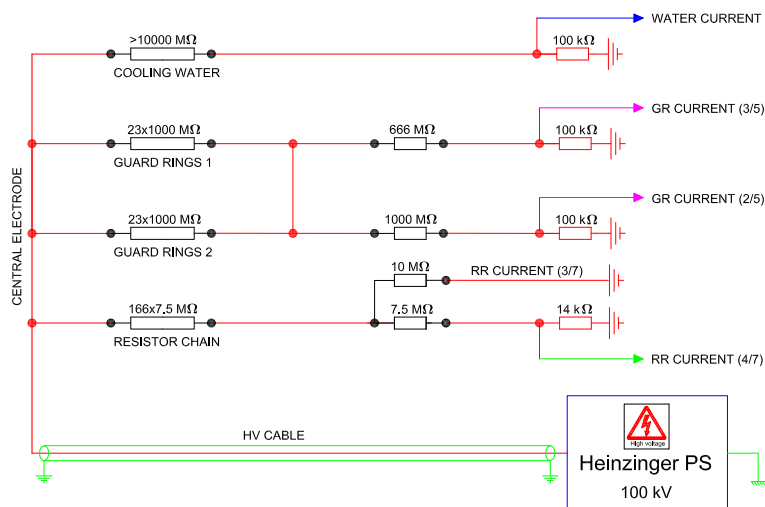


Figure 3.11: Resistor scheme of one fourth of the field cage. Taken from [40].

### 3.3.3 Service Support Wheel

To minimise the mechanical stress and thus possible sources of deformation from the end-plates, the front end electronics (cf. Sec. 3.3.5) as well as all its supply services are mounted on a separate support structure. The ‘Service Support Wheel’ (SSW) is placed in about 21 cm distance from the end-plates. For each sector along one spoke in radial direction the power supply lines (‘bus bars’) for the digital and analog low voltage of the front end cards and readout control units are mounted. Along the inner circumference of each sector pipes distribute water for the cooling of the electronics. A completely equipped sector is displayed in Fig. 3.16.

In addition splitter boxes which serve different purposes, gas and water distribution pipes, ADC boxes and further components are mounted on the SSW.

### 3.3.4 Readout Chambers

The TPC readout chambers (ROCs) are multiwire proportional chambers with a segmented cathod plane (‘pad plane’). To account for the radial dependence of the track density two different chamber types an inner (IROC) and an outer (OROC) readout chamber with different pad sizes as well as wire geometries were built.

The mechanical stiffness of the ROCs is provided by an aluminium body onto which an insulation plane and a pad plane is glued. The pad plane is a three layer printed circuit board with the pad structure etched onto its front side. The pads are connected by traces and vias with sockets on the back side.

A group of pads at the same local  $x$  (see Sec. 2.2.2) is called a pad row (cf. Fig. 3.13b). The size of the pads, as well as the number of pad rows and the total number of pads is summarised in table 3.1.

	Pad size [mm <sup>2</sup> ]	Number of rows	Number of pads
IROC (81.1 - 132.1 cm)	4 × 7.5	63	5504
OROC (134.6 - 198.6 cm)	6 × 10	64	5952
OROC (198.6 - 246.6 cm)	6 × 15	32	4032
TPC total		159	557568

**Table 3.1:** *Size and number of readout pads.*

Above the pad plane three wires layer are stretched in azimuthal direction. For this reason the wire length increases with the distance from the beam axis. Frames made of fiberglass-epoxy keep the wires, which were placed with a precision of 10 μm, in position. The anode wires are gold plated tungsten wires with a diameter of 20 μm, cathode and gating wires are made of copper-beryllium and have a diameter of 75 μm. The wire geometries of IROC and OROC are displayed in figure 3.12.

To minimise the ion-feed back along the edges of the chambers the surface of the wire frames as well as the surface of the chamber closure (‘edge strip’) at the long and short edge are covered with copper electrodes [41]. In addition the two edge anode wires have a larger diameter (75 μm) and their voltage can be set independently from the other anode wires to provide a lower gain in this region. The voltage of the surrounding electrodes, called ‘cover’, can be tuned to minimise field distortions close to the amplification region.

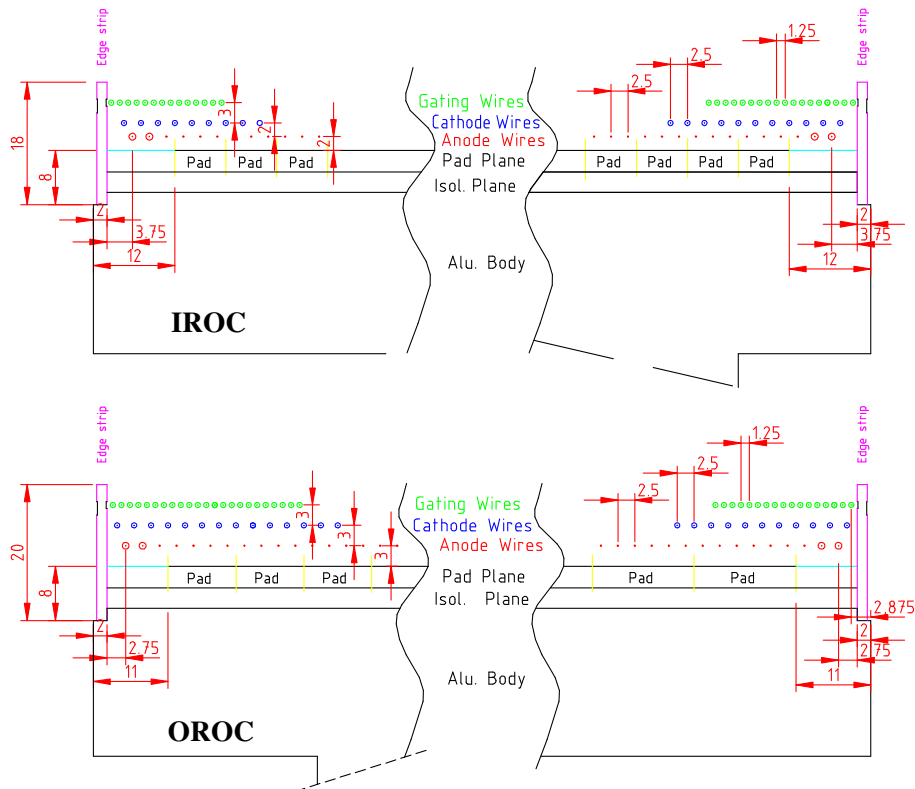
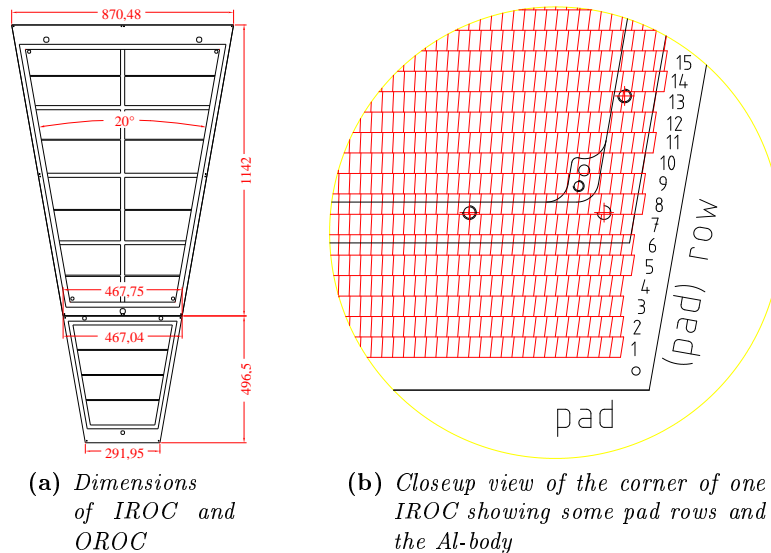


Figure 3.12: Wire geometry of the inner and outer readout chambers. Taken from [40].



(a) Dimensions of IROC and OROC

(b) Closeup view of the corner of one IROC showing some pad rows and the Al-body

Figure 3.13: ROC details. Taken from [40].

### 3.3.5 Front-end Electronics

The charge induced on the 557568 readout pads is read out by front end electronics (FEE) [42] connected to the sockets on the pad plane. The FEE can be divided into

### 3 THE ALICE TPC

two parts, the front end cards (FECs) and the readout control units (RCUs).

One FEC has 128 readout channels and does the actual signal processing. It is connected to the pad plane by six capton cables. The main parts of the card are eight Pre-Amplifier and Shaper chips (PASAs) and eight Alice TPC Readout Chips (ALTROs) each of which handles 16 channels. A scheme of the data flow of one channel is displayed in Fig. 3.14.

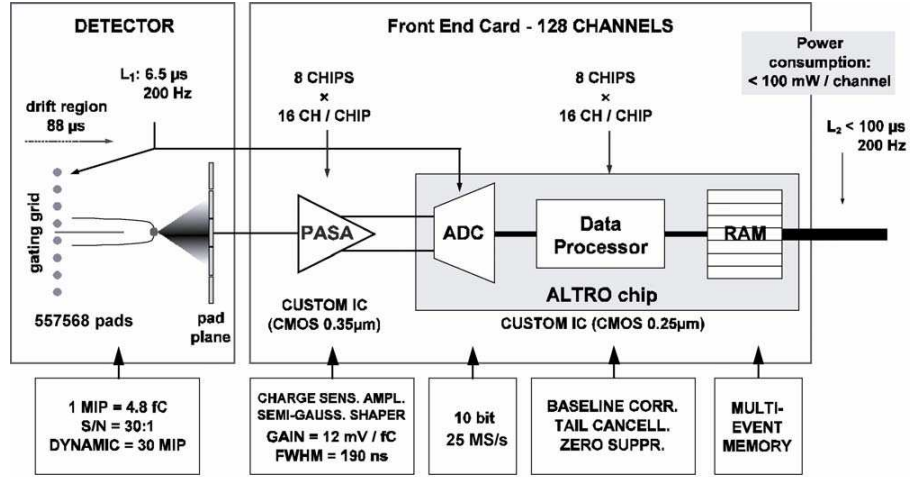


Figure 3.14: Main components of the front end cards [42]

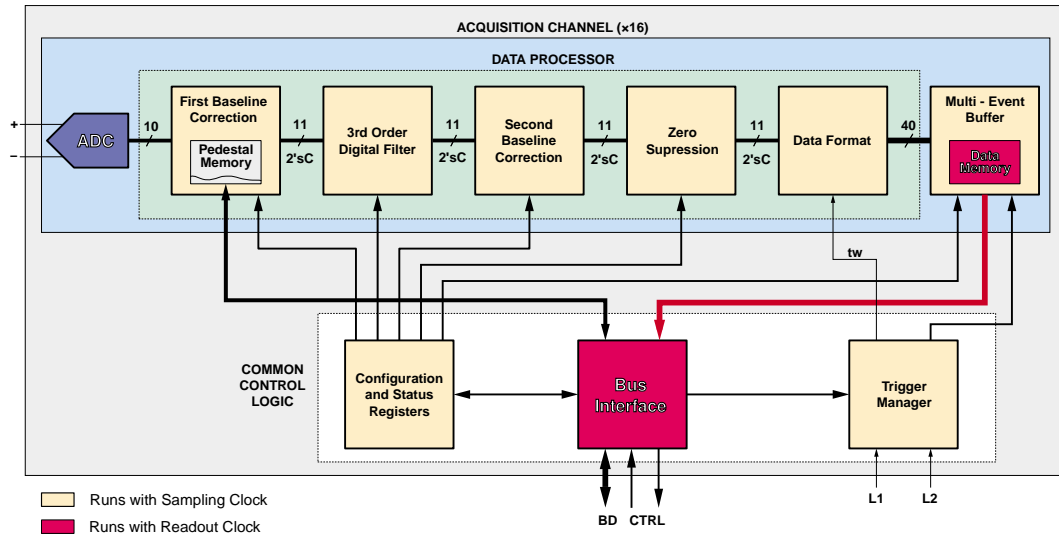


Figure 3.15: Block diagram of the ALTRO chip [43]

The PASA chip is a low impedance, charge sensitive amplifier followed by a semi-gaussian pulse shaper of the 4<sup>th</sup> order. The circuit has a conversion gain of 12 mV/fC and an output dynamic range of 2V at a power consumption of 11 mW/channel. The single channel noise is below an Equivalent Noise Charge (ENC) of 276 e<sup>-</sup> (RMS) for 0 pF input capacitance. Its shaping time (FWHM<sup>4</sup>) is 190 ns. To minimise pickup noise the PASAs and the immediately following ALTRO chips are connected via differential lines.

<sup>4</sup>Full Width at Half Maximum

Each channel of the ALTRO chip has three components, a 10 bit 25 MSPS<sup>5</sup> ADC, a digital circuit with several digital filters and a multi event buffer (Fig. 3.15). If a Level-1 trigger is received a predefined number of samples is read out and stored temporarily in the buffer. Only upon the arrival of the Level-2 trigger this event will be frozen in memory and shipped to the data acquisition system. Otherwise the data will be overwritten.

Because of the extremely high raw data volume ( $\approx 700$  MByte/event<sup>6</sup>) it is mandatory to perform a zero suppression already on the level of the FEE. In order to preserve the full resolution on the signal features (amplitude and time) a very accurate cancellation of the signal tail and correction of the baseline have to be performed before zero suppression is applied. This is done in the highly configurable digital filter circuit, which comprises the following steps:

**Baseline Correction I:** In this step a first baseline correction is performed, needed to apply the tail cancellation filter in a proper way. Three possibilities are offered for this filter. A *fixed pedestal* subtraction mode which means one value per channel, for all time bins. A *time dependent pedestal* subtraction mode which uses the pattern memory and provides one value per time bin. And a *self calibrated pedestal* subtraction mode, which calculates the cumulative average of the signal outside the data processing window.

In addition this step can be used in a *conversion mode* where a (static) conversion  $y_n = F(x_n)$  is applied. This feature can be used to perform an equalisation of the response across different channels. The conversion mode can work concurrently to the self calibrated subtraction mode and to the fixed subtraction mode.

For test purposes the pedestal memory can be used as a lookup table to generate a pattern to be injected into the processing chain instead of input signals.

**Tail Cancellation Filter:** To minimise the pile-up effect of subsequent signals, caused by the ion tail of the gas amplification, a tail cancellation filter can be applied. In the filter process the signal is approximated by the sum of four exponential functions. The six parameters of the filter can be adjusted for each channel separately.

**Baseline Correction II:** A second level of baseline subtraction can be applied after the tail cancellation filter. This correction is done during the signal readout and calculates a moving average in a configurable acceptance window around the baseline.

The pedestal value to be subtracted from the current sample is the average of the signal itself and the previous seven. If the signal is outside the acceptance window the average that was calculated for the last sample in the acceptance window is used. This filter is also called the *moving average filter*.

**Zero Suppression:** The aim of the zero suppression is to discard samples which do not carry information, this means e.g. samples close the baseline only containing noise. The filter is comprised of several steps, configurable for each channel.

The basic step is to apply a fixed threshold. Only values above this threshold are kept. To remove glitches the minimum number of consecutive samples needed to define a valid signal can be configured. A number of pre- and post-samples can be defined, that should be kept before and after a peak independently of the threshold. Sets of samples closer than three samples will be merged to one set.

**Data Formatting:** Due to the removal of a variable number of samples in the zero suppression step two extra words, coding the start time and length of the cluster, are added at the end of each data set. Sets of samples closer than three samples will be merged to one set, for obvious reasons. Since the ALTRO data bus has a width of 40 bit

<sup>5</sup>Meaga Samples Per Second

<sup>6</sup> $557568 \text{ channels} \times 1000 \text{ timebins/channel} \times 10 \text{ bit/timebin} / 8 \text{ byte/bit} = 696960000 \text{ byte}$

### 3 THE ALICE TPC

the 10 bit ADC values and the two extra words are packed in 40 bit words. At the end a trailer is added to the data packet, containing the hardware address identifying the readout channel and the number of 10 bit words in the packet.

The complete functionality of the ALTRO is described in great detail in the ALTRO manual which can be found on the ALICE TPC front end electronics homepage [44, 43].

Monte Carlo studies have shown [20] that a signal to noise ratio (SNR) of 30:1 is required to reach the detector resolution limit. A minimum ionising particle produces a typical maximum charge of 4.8 fC ( $3 \times 10^4$  electrons) in one pad and time bin. This leads to a maximum acceptable noise of 1000 electrons, corresponding to one ADC channel<sup>7</sup>.

The FECs are grouped in *patches* (or *partitions*) of up to 25 cards, controlled by one RCU [45, 44] which interfaces the FECs to the Data Acquisition System (DAQ), the trigger and the Detector Control System (DCS). One TPC sector has six patches, two in the IROC and four in the OROC giving a total of 216 readout partitions. Each partition is connected via optical fibres, the Detector Data Links (DDL), to the DAQ. DCS communication is provided by means of standard 100 Mbit ethernet connections. The number of cards in each patch is summarised in table 3.2.

Patch	Number of FECs	Chamber type
0	18	IROC
1	25	IROC
2	18	OROC
3	20	OROC
4	20	OROC
5	20	OROC
total	121	

**Table 3.2:** *Number of front end cards in each readout patch.*

In figure 3.16 one completely equipped TPC sector is displayed. The density of the electronics is very high, especially at the inner sector. The FECs sit behind the data bus ('backplanes'). They are inserted into aluminium frames which are mounted on the service support wheel. Flexible silicon hoses connect groups of six FECs in series with the sector cooling pipes.

#### 3.3.6 Sector Naming Conventions and Usage of the Field Cage Rods

The naming conventions [46] for the readout sectors (one IROC + one OROC) and the individual readout chambers (each IROC or OROC) are not obvious at first view. In addition often different presentations of the C-Side data exist, depending on the software that was used for visualisation and results from the symmetry of the TPC setup. This chapter is intended to shed some light on this issue.

<sup>7</sup>One ADC channel corresponds to  $\approx 2$  mV (2 V/10 bit). The PASA conversion gain is 12 mV/fC. Therefore one ADC channel corresponds to about 0.16 fC or an ENC of 1000  $e^-$ .

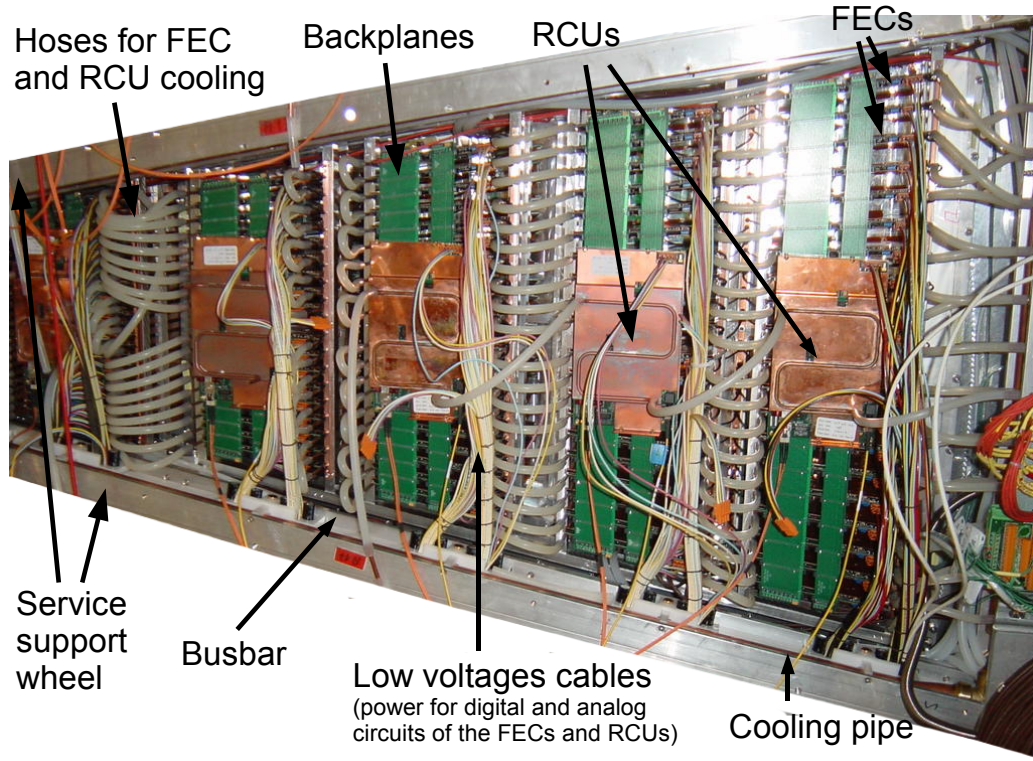


Figure 3.16: A completely equipped sector. The first patch is outside the view.

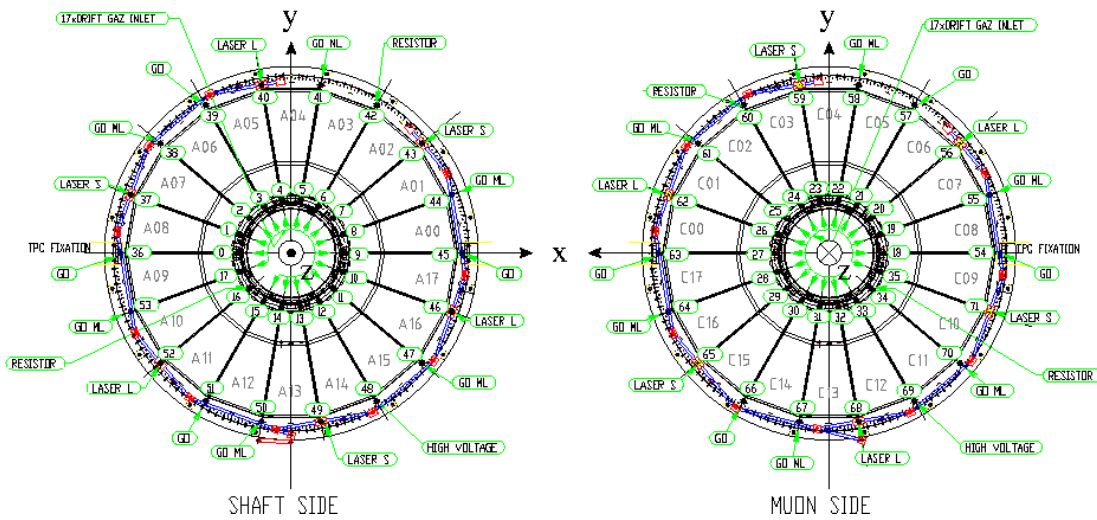


Figure 3.17: Technical drawing of the end-plates (front-view) showing the numbering conventions for the sectors and also the FC rods. In addition the purpose of each rod is denoted. The blue lines and red boxes show the LASER distribution system. Taken from [40]

The TPC readout has mainly a 3-fold segmentation: a division in two *readout sides* (A and C or also called Shaft and Muon, cf. Sec. 2.2); each readout side is subdivided in 18 trapezoidal *sectors*; each sector is subdivided in radial direction into one IROC and one

OROC. A further subdivision exist of course for the readout electronics (cf. Sec. 3.3.5). The numbering which is not discussed here can be found in [46].

As defined in [30] the numbering is done in  $\phi$  direction, starting from 0 and separately for A- and C-Side, where mirror sectors have the same number. Therefore sectors are numbered A00 to A17 and C00 to C17 as displayed in Fig. 3.17. The ROCs are then called e.g. IROC A10, OROC C12 . . . .

In the offline software code, however, for historical reasons ROCs are also referred to as sectors and have a continuous numbering from 0 to 71. The numbering runs over all IROCs first, first A- then C-Side, followed by all OROCs. ‘Sector’ 0 therefore is IROC A00, 18 corresponds to IROC C00, 36 to OROC A00 and 54 to OROC C00.

In technical drawings and also the slow control software of the TPC, information of each readout side is for obvious reasons presented as a front-view like in Fig. 3.17. This is also done in 2D online software monitors. Contrary to this offline data are always presented looking from the A-Side towards the C-Side, which means that the C-Side representation is mirrored along the  $y$ -axis wrt. to Fig. 3.17.

Some of the FC support rods house the voltage dividers (‘resistor rod’) and the mirror bundles of the laser system (‘laser rods’). The gas inlet and outlet is also provided through a part of the FC rods. The different functions are denoted in Fig. 3.17.

## 3.4 Auxiliary Systems

### 3.4.1 Laser Calibration System

Narrow beams of pulsed UV laser light can be used to simulate ionising tracks in the active volume of the TPC [47]. For calibration purposes a laser system has been integrated into the detector [48]. 336 laser rays illuminate the TPC, 168 on each side. They are deflected into the active TPC volume by micro mirror bundles which are mounted inside the laser rods (cf. Sec. 3.3.6). Each rod carries four bundles of seven micro mirrors distributed along the  $z$  direction. Fig. 3.18 shows a sketch of the system.

With the help of the straight laser tracks it is possible to study and correct for residual misalignments of the readout chambers. Further goals are to correct drift velocity variations in space and time, which are caused among other effects by temperature variations, understand the influence of space charge and address  $E \times B$  effects.

To ionise the gas two pulsed Nd:YAG laser (1064nm) equipped with two frequency doublers are used, generating pulses of 266 nm and 5 ns pulse duration. The lasers are placed in a hut outside the L3 magnet. Each delivers a 25 mm wide beam with an energy between 70 and 150 mJ, which is guided to the A- and C-Side, respectively. In case of a failure of one laser, the remaining beam can be split. On both end-plates a prism/mirror system distributes the beam such that it is injected into the laser rods.

The micro-mirror bundles (see Fig. 3.19) reflect the laser light perpendicular to the beam axis into the active volume of the TPC. They are placed at  $z \approx \pm 130, 850, 1690, 2470$  mm for odd laser rods (counted in  $\phi$  direction) and  $z \approx \pm 100, 790, 1630, 2410$  mm for even rods. Each bundle contains seven quartz fibres of 1 mm diameter, cut at an angle of  $45^\circ$  and coated for full reflectivity of 266 nm UV light. The bundles are placed such that they do not shadow each other. At the end of the rod a CCD camera allows for checking the alignment of the beam within the rod (see bottom right in Fig. 3.18).

The laser rays resulting from the micro-mirror reflections have approximately gaussian cross sections with a transverse size of  $\sigma_{\text{ray}} \approx 400 \mu\text{m}$ . Due to the quadratic nature of the



ionisation process the track, however, will have a width of  $\sigma_{\text{track}} = \sigma_{\text{ray}}/\sqrt{2} = 280 \mu\text{m}$ . The pulse length of 5 ns causes an additional smearing in drift direction. Assuming a square time distribution and a drift velocity of 2.8 cm/ $\mu\text{s}$  this effect is  $\sigma_{z,\text{track}} = 5 \cdot 10^3/\sqrt{12} \cdot 2.8 = 40 \mu\text{m}$ .

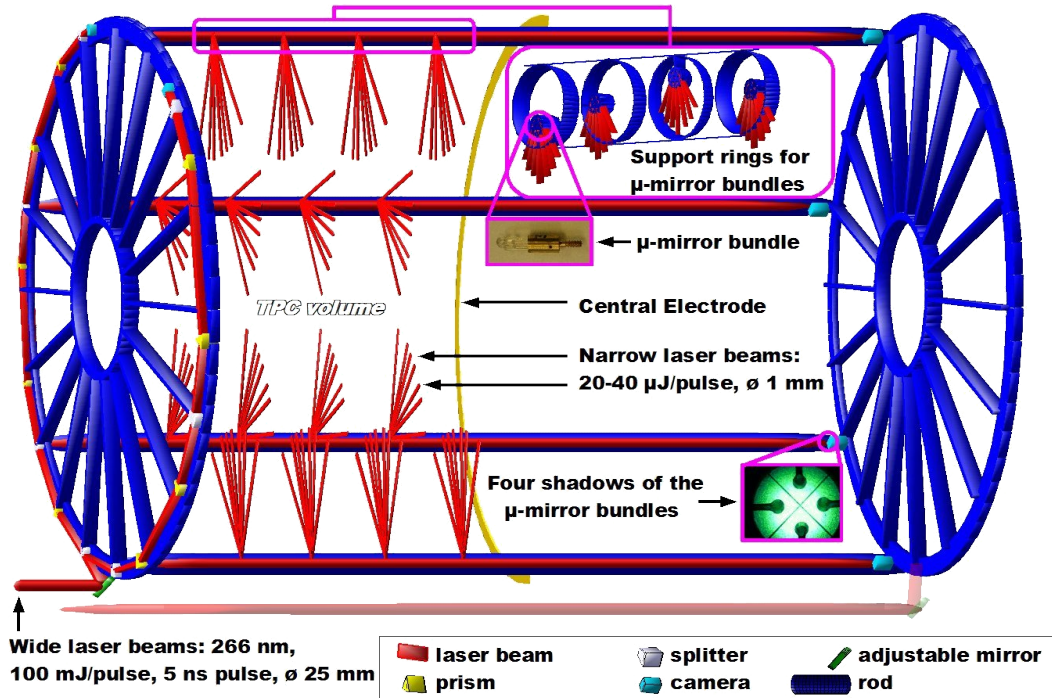


Figure 3.18: Principle of the TPC laser system. Taken from [49]

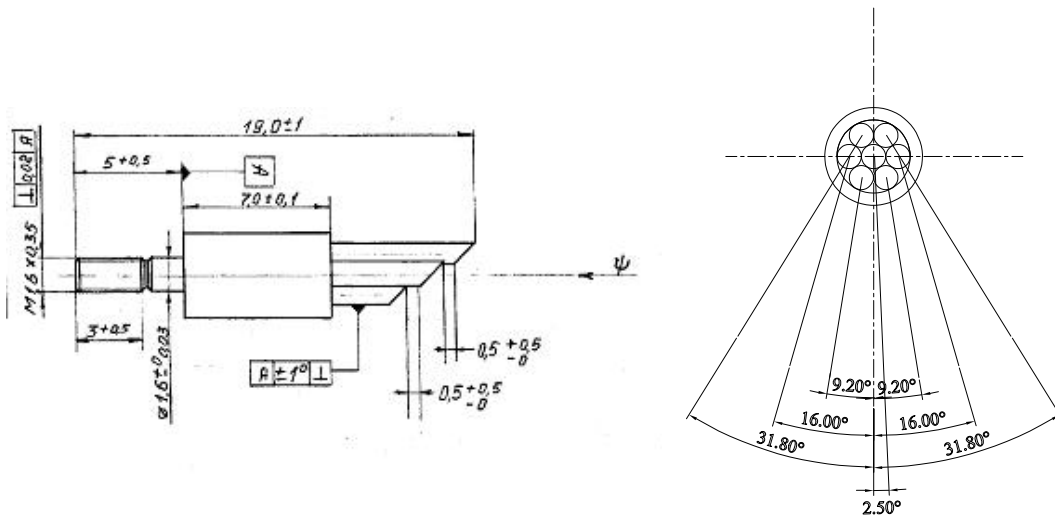


Figure 3.19: Design of the micro-mirror bundles [48]

### 3.4.2 Choice of the Gas Mixture and the Gas System

The basic gas mixture chosen for the ALICE TPC is Ne-CO<sub>2</sub> [20]. Argon is ruled out as a noble gas for two main reasons: The number of produced electron-ion pairs is about two times larger than in Neon and the Ar<sup>+</sup> mobility is a factor 2.5 lower than that of Ne<sup>+</sup>. Using Argon in the expected high flux environment at LHC would therefore lead to the accumulation of space charge resulting in intolerable ( $>10^{-4}$ ) field distortions.

For the quencher gas hydrocarbons cannot be used. This is a consequence of the high doses expected at the anode wires for the lifetime of the experiment (11 mC/cm), safety regulations and the production of thermal neutrons. Dedicated tests with P10 gas (Ar-CH<sub>4</sub>) on a full size readout chamber prototype showed dramatic gain degradation and Malter breakdown after the equivalent of 1-2 year operation. CF<sub>4</sub> in contact with aluminium still leaves open questions and therefore has not been taken into consideration [50]. Therefore, the only choice left is CO<sub>2</sub>.

The exact mixture is defined by the constrain of the maximum tolerable drift time to cope with the required event rate. This leads to a maximum CO<sub>2</sub> concentration of 10 %. This gas mixture, however, has the undesirable property that at the nominal drift voltage (400 V/cm) the drift velocity is strongly dependent on the gas parameters such as pressure, temperature and exact mixture<sup>8</sup> [36]. A direct consequence is the need of a temperature stability and homogeneity of  $<0.1^{\circ}\text{C}$  in order to exhaust the intrinsic detector resolution and meet the desired physics performance.

Studies [50] showed that adding a few percent of N<sub>2</sub> to the Ne-CO<sub>2</sub> gas mixture improves the stability of the readout chambers which are operated at a relatively high gain of  $2 \times 10^4$ . N<sub>2</sub> has a larger photon absorption cross section than CO<sub>2</sub> at the main excitation state of Ne (16.8 eV). Therefore, N<sub>2</sub> supports CO<sub>2</sub> to quench this excited state.

The finally chosen gas mixture which is used in the TPC, is Ne-CO<sub>2</sub>-N<sub>2</sub> in proportions [90-10-5].

The large volume of the TPC and the usage of an expensive gas mixture ( $\approx 90\%$  Ne) makes it mandatory to use a recirculating gas system. As a consequence gases from the ambient air, mainly N<sub>2</sub>, O<sub>2</sub> and H<sub>2</sub>O will accumulate in the system. O<sub>2</sub> and H<sub>2</sub>O have the very unfavourable effect of causing electron attachment and therefore have to be removed from the gas. This is done by routing the recirculated gas through a purging station which uses activated copper and a molecular sieve to remove these two components. The N<sub>2</sub> content is controlled by the fresh gas rate, which is in standard operation about 40 l/h and can be adjusted between 0 and about 90 l/h.

To constantly monitor the gas quality a dedicated device ('Goofie') had been developed for the NA49 experiment [51] and was adapted for the requirements of the ALICE TPC [52]. Two alpha-sources ionise the gas in a distance of  $\approx 20$  cm. *Start counters* register an ionisation event. The electrons drift in the TPC gas towards a *pickup counter*. With the difference in arrival time and the known distance of the sources, the drift velocity in the gas is calculated. In addition the pickup counter allows to measure the gas gain. Using the functional dependences of drift velocity and gas gain on CO<sub>2</sub> and N<sub>2</sub> changes in Ne, together with a precise calibration of the device, allows for monitoring small changes in the gas mixture.

---

<sup>8</sup>To obtain the required drift velocity stability of 1% in a Ne-CO<sub>2</sub> [90-10] mixture at T=300 K and P=1 bar the CO<sub>2</sub> concentration has to be kept stable within  $10.000 \pm 0.013\%$

### 3.4.3 Cooling System

To maintain a temperature stability and homogeneity of  $< 0.1^\circ\text{C}$ , a complex cooling scheme has been worked out for the TPC [53]. The main heat sources considered are the front end electronics with a total heat dissipation of  $\approx 30$  kW and the neighbouring detectors (ITS, TRD).

On the detector side the system is comprised of two thermal screens (inner and outer), a sector by sector distribution system for the FEE cooling (see Fig. 3.21a), four distribution circuits for the cooling of the Al-bodies of the ROCs and four distribution circuits for the bus bar and cover cooling (see Fig. 3.21b).

The inner screen covers the cones of the inner containment vessel, while its central part was omitted in order to maintain a low radiation length in the full TPC acceptance. This screen is supposed to remove residual heat from the ITS power cables, which is not taken away by the ITS cooling system. The outer screen is installed in the clearance between the TPC and the TRD.

To remove the heat dissipated by the FEE the front end cards and RCUs are wrapped in water cooled copper plates (see Fig. 3.20). Copper pipes in the SSW installed along the inner circumference of each sector supply the cooling water for FEC and RCU cooling. Six FECs each are connected in series as well as all six RUCs of one sector (see Fig. 3.16).

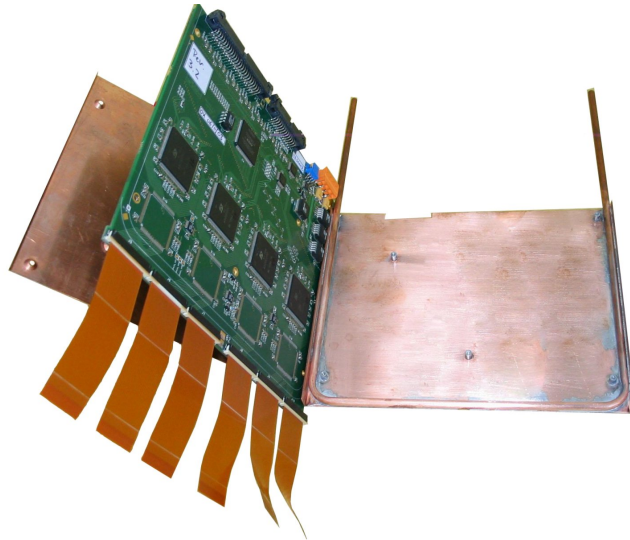


**Figure 3.20:** *Front end card wrapped in copper plates*

Although the FECs are wrapped in cooled copper plates not all heat will be removed. A fraction of the energy escapes and will heat up the air in the space between the FEE and the chambers. In addition the capton cables connecting the readout plane with the electronics act as heat bridges [54]. To minimise the influence on the TPC gas temperature the Al-bodies of the chambers have embedded cooling pipes. On each readout side the nine top and nine bottom sectors belong to one cooling circuit (see Fig. 3.21b).

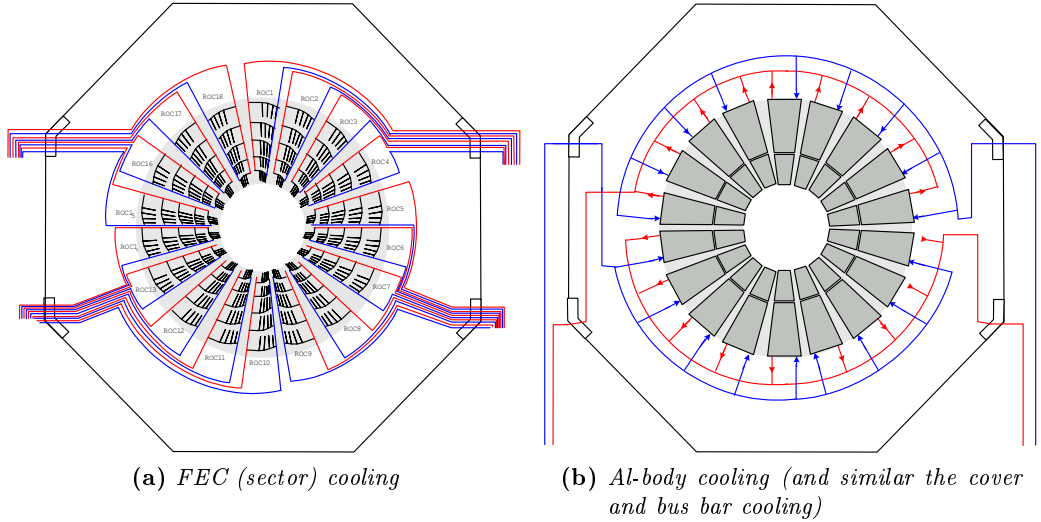


Figure 3.21: Cooling circuit schematics

Another heat source are the bus bars which distribute the power for the FEE. They are cooled by pipes attached to the same spoke of the SSW. Finally the SSW is closed by cooled covers. The covers and bus bar cooling pipes of nine top and bottom sectors, respectively, share a cooling circuit.

The cooling plant used allows for operating the complete system in the so-called “leakless”<sup>9</sup> mode. This is achieved by ensuring that the water pressure within the detector is below atmospheric pressure. It is possible to adjust the water flow as well as the temperature of each circuit individually. The precision of the temperature regulation is 0.1°C. A detailed description of the complete system can be found in [53].

### 3.4.4 Temperature Monitoring System

To measure the temperature inside and outside the TPC, a temperature monitoring system with about 500 Pt-1000 sensors has been installed [55]. The system will help to set the proper cooling circuit temperatures to ensure the desired temperature stability and homogeneity.

Temperature sensors are placed on the hull of the TPC (outer containment vessel), the inner hull (inner containment vessel, cones and centre part), inside the TPC close to the end-plates, on the readout chamber bodies and on the inlet and outlet of each sector cooling circuit.

The sensors are read out with ELMB<sup>10</sup> ADCs [56], which are mounted on the outer circumference of the SSW, nine on both side. Each ELMB can read out 32 sensors.

The sensors are calibrated with an absolute precision better than 10 mK. The relative precision of the sensors at the calibration temperature ( $\approx 22^\circ\text{C}$ ) is better than 2 mK [55].

### 3.4.5 Gating Grid Pulser System

The *gating grid pulser* system is responsible for opening and closing the gating grid. Fast FETs are used to switch between the two voltage settings. In the open mode all wires have

<sup>9</sup>“Leakless” systems were developed by M. Bosteels, CERN ST/CV

<sup>10</sup>Embedded Local Monitor Board

the same (offset) voltage of -100 V. In the closed mode neighbouring wires are switched to the offset voltage  $\pm 90$  V.

Although the switching voltage is quite large, the differential voltages compensate quite well in the far field. For that reason the signal induced on the pads does not saturate the electronics.

### 3.4.6 Calibration Pulser System

In order to test the response of the electronics independently from gas amplification, a signal pulse can be injected on the cathode wires of the readout chambers. The *calibration pulser*, responsible for this task, produces a step function with a maximum amplitude of 8 V, chosen to be able to cover the full dynamic range of the ADCs in the ALTRO chips.

While the rising edge of the step function can be shifted in time and lies always in the data acquisition time window, the falling edge is outside the data taking. Due to the capacitive coupling between the cathode grid and the pad plane, the differentiated signal of the step function (a narrow peak, ideally a spike) is induced in the electronics. The signal is then shaped by the pre-amplifier/shaper (PASA) chips and further processed in the ALTROs.

Since the induced signals should be the same in all pads, it is possible to determine differences in the shaping behaviour of the PASA chips. Those differences arise from the manufacturing tolerances.



## 4 The TPC Commissioning in SXL2

In this chapter the TPC commissioning on surface level is described. It took place in the clean room in building SXL2 at point 2 at CERN. Here the TPC had already been assembled. After an introduction about the commissioning schedule and its objectives, results of the analyses of pedestal, calibration pulser and laser data will be presented and discussed.

### 4.1 Introduction

The assembly of the TPC at Point 2 began in March 2002 with the delivery of the inner field cage vessel. During 2002 and 2003 the outer field cage vessel as well as the inner and outer containment vessels were delivered and set up. From October to December 2003 the end plates as well as the central electrode were assembled. The mounting of the field cage (FC) took place in the first months of 2004 until the TPC was closed in April for the first leak tests. For these measurements the end plates were sealed with aluminium plates in the places where the readout chambers (ROCs) would be installed later.

The production of the multiwire proportional readout chambers started in March 2001 and was finished in May 2004. The installation of the readout chambers began end of August 2005 and took slightly more than one month. After all chambers were installed, in December 2005 a mechanical alignment had been performed. The aim of this alignment was to position the gating grid planes of all ROCs in one plane parallel to the central electrode. Mounting and connecting the front end electronics was done in the period from January to March 2006.

After the assembly has been finished successfully, the planned first commissioning began in June 2006. In January 2007 the TPC was transported to SX2 to go underground to the experimental area.

The main objectives of the commissioning at surface level were to perform the mechanical alignment of the readout chambers and test the functionality and performance of all chambers in their final place. This included intense testing of the front end electronics. For a “burn in” of the electronics, all sectors had been operated for 48 hours.

If against expectations a chamber would not perform within specifications it would be much more secure and easier to exchange it in the clean room than in the final position underground where the space is much more restricted. Also the performance of the TPC laser system was tested for the first time. All mirrors of the guiding system had to be aligned.

A functional check of the test setup was carried out end of May 2006 with the first two sectors (4 and 13, A-Side). They were connected to the essential services (s. 4.2), powered up and the nominal drift voltage of 100 kV was applied on the field cage. Due to a leak in sector A04 the cooling system had to be revised before the measurements went on.

End of June the commissioning was re-started including all sectors. In the period from June 27th to August 11th 2006 sectors on the A-Side were operated, followed by the

commissioning of sectors on the C-Side in the period from August 18th to October 5th. A second round of testing for both sides was started on October 9th.

During this commissioning services for only two sectors at a time were available, the equipment which was used is described in Sec. 4.2.

This procedure also implied that for each pair of sectors the conditions such as gas temperature, ambient pressure and gas composition changed, resulting in a change of the electron drift velocity in the gas and also the gas gain. This effect has to be taken into account when comparing different measurements.

Four types of measurements were supposed to be carried out for all sectors:

1. Pedestal and Noise measurements
2. Calibration Pulser measurements (study the shaping properties of the electronics)
3. Measurements with the TPC Laser system (for alignment purposes)
4. Gain measurements (using a cosmics trigger)

The results of points 1-3 are discussed below. The gain measurements are summarised in Ref. [57].

## 4.2 Setup

For the surface commissioning services were installed to power up only two sectors at a time. The main reason why only two sectors could be tested simultaneously is that the front end electronics (FEE) needs to be cooled during operation. Setting up a secure cooling system for more than two sector would have been much too complex and could not have been justified in terms of man power and expense.

The cooling system used was operated in a *leakless mode*. The hydraulics of such a system is adjusted such, that the pressure within the detector is below atmospheric. A sketch of the system is given in figure 4.1. A vacuum pump connected to the water reservoir keeps the system under underpressure. If a leak occurs in the system, the pressure in the reservoir rises. If the pressure rises above a threshold, the system stops the circulation pump. In this case both inlet and outlet are exposed to the full underpressure of the reservoir, such forcing the water to flow back to the tank.

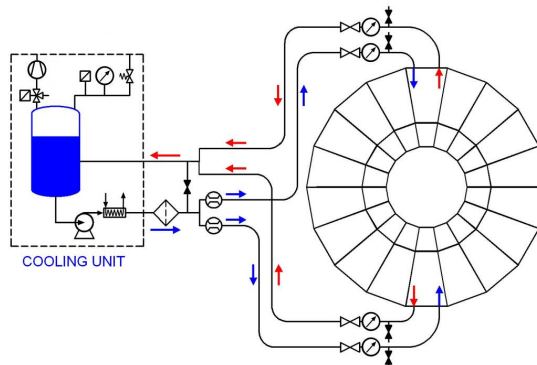


**Figure 4.1:** Schematics of the cooling system used during the commissioning. Taken from [40].

The system was adjusted to a flow of about 10 l/min in both circuits.



Two *Plein & Baus* ‘*Wiener PL508*’ power supplies were used to provide the low voltage for the FEE. They have similar specifications as the finally used PL512. The FEE was connected to the power supplies using  $\approx 40$  m long cables with a cross-sectional area of  $200 \text{ mm}^2$ . This corresponds in good approximation to the final configuration.

The high voltage for the readout chambers was provided by *ISEG EHQF025p* modules. In the final operation similar devices (*ISEG EHQF025p*) will be used. In contrast to the final setup, the voltages of the anode wires for the two different pad size of the OROC were not set individually but together. Both the low voltage as well as the ROC high voltage was operated and controlled through the detector control system (DCS).

Laser data were taken with a Nd:YAG 1064 nm laser (Spectron Laser Systems Ltd, model SL805-UPG) equipped with two frequency doublers, which is already one of the two final devices. It was placed in front of the A-Side. The beam optics could be adjusted to deliver the beam to the laser distribution system either on the A- or the C-Side.

The cosmic trigger was set up using ACORDE<sup>1</sup> [58] modules. Those are plastic scintillators, read out by photo-multiplier tubes. The modules are part of the ALICE cosmic ray trigger. They will be mounted on the top of the L3 magnet.

Data taking was provided by the final DAQ system. Trigger sequences were defined for cosmic, laser, pedestal and calibration pulser events. The data was transferred through dedicated glass fibres, which had been laid from the clean room to the DAQ counting room. During the night the data was automatically migrated to CASTOR<sup>2</sup>, a system for permanent data storage.

For the supply of the detector gas long copper pipes have been laid from the ALICE gas building to the clean room. This allowed to commission and understand the final TPC gas system.

The calibration pulser and gating grid pulser system was set up using the final modules.

---

<sup>1</sup>A COsmic Ray DEtector for ALICE

<sup>2</sup>CERN Advanced STORage manager

## 4.3 Results

### 4.3.1 Mechanical Alignment of the Readout Chambers

In order to maintain distortions of the electric field below a residual fraction of  $10^{-4}$ , which is the overall design constraint [20], the parallelism of the CE with all gating grid wires of the readout chambers has to be of this order. For a drift length of 250 cm this requires a global alignment better than 250  $\mu\text{m}$ , where the planarity of each electrode (CE and gating grid wire plane) should be of the order of 100  $\mu\text{m}$ .

The relative position of the central electrode and the end-plates is given by six reference points on each of the inner and outer diameter of the end-plates, which have been surveyed after their installation. To determine the relative position of the ROCs to the reference points, each IROC and OROC was equipped with three and four survey points, respectively. For those the distance to the gating grid wire plane is known. The exact position of the ROCs in each end-plate is defined by three shims. These are brass cylinders with a diameter of 13 mm (IROC) and 18 mm (OROC) and an initial length of  $\approx 22$  mm. For the determination of the final size of each shim surveys have been carried out on the A- and C-Side using a photogrammetric measurement.

A first survey of the A-Side [59] revealed that the inner and outer ring of the end-plate had a relative offset of 2.1 mm along the  $z$ -axes. For this reason it was decided to use the I-Bars<sup>3</sup> to pull the end-plates into the correct shape. A force of  $2 \times 2.6$  kN is needed to compensate for the difference.

The results of the surveys reported in Ref. [60, 61] have been used to determine the size of each shim. After their exchange another survey has been performed [62, 63] to verify the result. Fig. 4.2 shows the outcome of the alignment. Displayed are the deviations of the survey points from the ideal case (perfect plane), separately for the IROCs and OROCs of A- and C-Side. All points are distributed within a narrow peak around zero. The RMS values of the distributions, being all smaller than 90  $\mu\text{m}$ , are given in the legends of the histograms. Considering the error stated for the survey measurements of 100  $\mu\text{m}$  (sigma), which is also the required precision discussed above, all chambers were aligned as desired.

The distances of the gating grid planes to the CE were calculated to be 2497.25 mm and 2496.98 mm for the A- and C-Side, respectively.

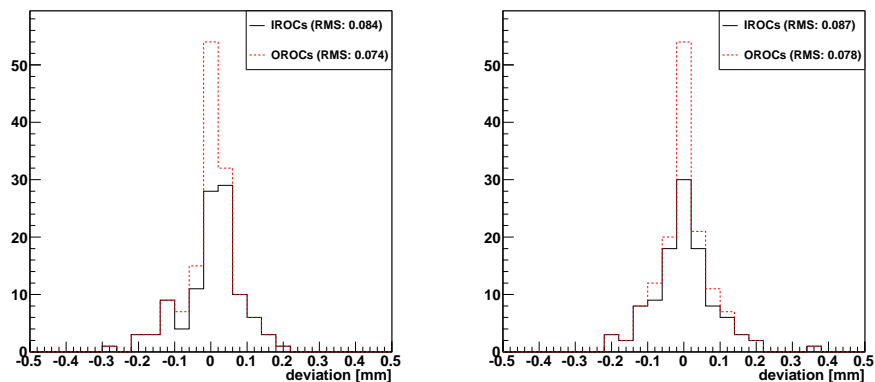


**Figure 4.2:** Deviations of the survey points from the ideal case (perfect plane) after the tuning of the shims for the A-Side (left) and C-Side(right).

<sup>3</sup>A mechanical structure which was originally planned to be used to balance the slope of the LHC tunnel, under which the end-plates would deform under their own weight.

### 4.3.2 Pedestal Distribution and Detailed Noise Studies

As described in Sec. 3.3.5 the large data volume of the TPC requires a zero suppression (ZS) of the data already on the level of the front-end electronics. In order to perform the ZS for each channel the electronic baseline (pedestal) has to be known. The ZS threshold is naturally determined as a multiple of the width of the baseline distribution (noise). Therefore both values have to be measured precisely. This of course also implies to monitor the stability of both values.

To achieve the required SNR of 30:1 the noise level has to be kept below about 1 ADC channel (cf. Sec. 3.3.5). The exact value of the noise is also needed in the offline reconstruction algorithm. During the final operation both values will be evaluated in special pedestal calibration runs and stored in an offline calibration database (OCDB).

The typical baseline of one electronic channel is displayed in Fig. 4.3a. To calculate the pedestal and noise value, the baseline is projected to the ordinate between time bins 60 and 1000 (Fig. 4.3b). Several events are summed up to get a statistically better value. A gaussian function is fit to this distribution. Its mean defines the pedestal value, the sigma corresponds to the noise.

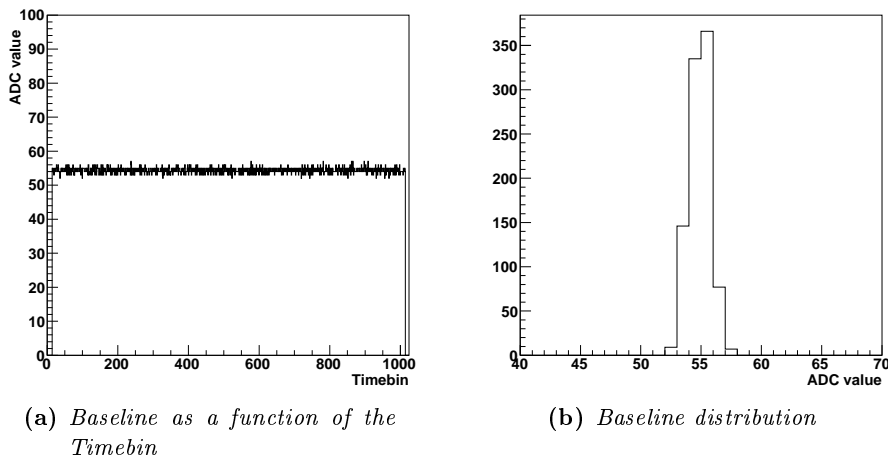


**Figure 4.3:** *Typical electronic baseline of one channel*

A calibration class (AliTPCCalibPedestal) has been developed which analyses raw data and calculates the pedestal and noise value for each channel. It can be found in the TPC directory of the ALICE offline framework AliRoot [64]. A detailed description and an example of use is given in appendix A.

Extensive noise studies have been carried out during this first commissioning of which a large part is discussed below.

#### 4.3.2.1 Noise with Switched-off Field Cage and Readout Chamber Voltages

The pedestal and noise data discussed in the following were taken with the field cage high voltage switched off and also the readout chambers had not been powered up. No special configuration was chosen for the FEE. Data exist for all sectors but A00, C03 and C04. The influence of applied voltages will be discussed in Sec. 4.3.2.4.

Fig. 4.4 shows the distribution of the measured pedestal (a) and noise (b) values in all chambers. The pedestal values follow a gaussian distribution around a mean value of 51.4

with a sigma of 9.2 and lie in the expected range, given by the manufacturing tolerances.

The noise values are distributed non-symmetrically. They have a maximum at 0.69 and a very long tail towards higher values. As shown in Fig. 4.5 the noise is different in the IROC, the inner part of the OROC (short pads) and the outer part of the OROC (long pads), corresponding to different pad sizes and hence different input capacitance. For this reason noise analysis will be done separately for the different pad sizes. It is found that the maximum noise increases from the IROC to the outer part of the OROC and the width of the distribution also broadens. Table 4.1 summarises the maximum as well as the truncated mean between 0 and 2 ADC-channels and its RMS for the different pad sizes.

In Fig. 4.5 two presentations of the noise distribution are given. In pad (a) the histograms are given in a log scale to demonstrate the long tail of the distributions, while in pad (b) a linear representations was chosen, and the histograms have been normalised by the number of entries. This is used to illustrate the different width of the distributions.

In the two-dimensional noise distributions (Fig. 4.5, pads (c)-(f)) no distinct hotspots are found in the IROC, whereas in the OROC one can clearly see regions of high noise<sup>4</sup>: along the edge it is higher than at the centre of the chambers, towards the outer corners the noise increases even more and at the edges of pad rows 52 to 54 one can also see an increase.

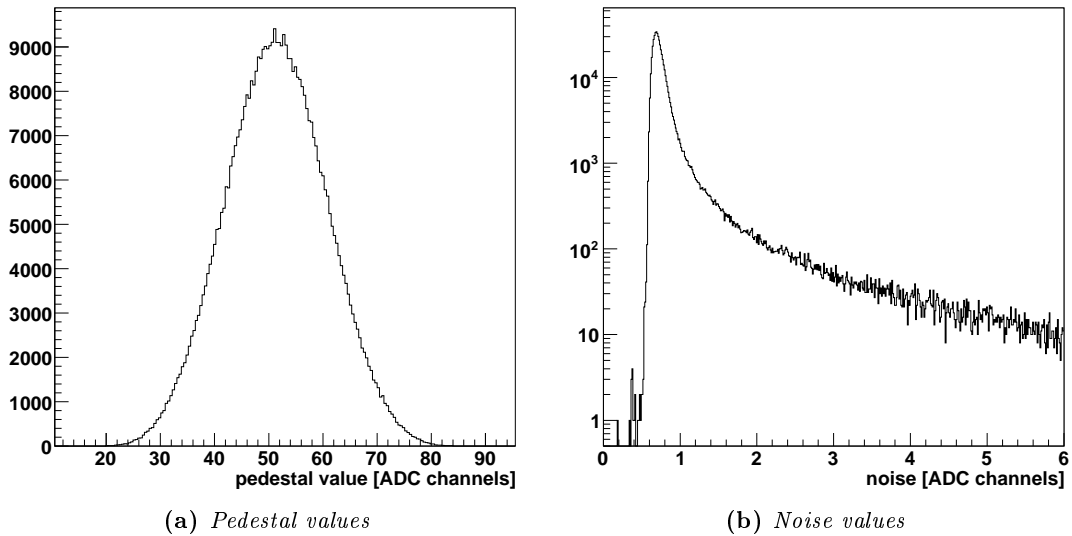
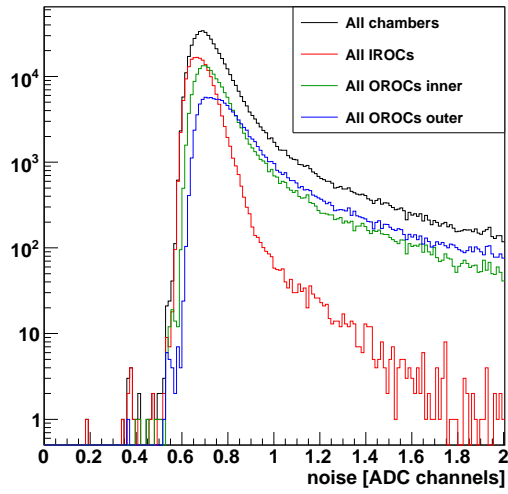


Figure 4.4: Pedestal and noise distribution of all sectors

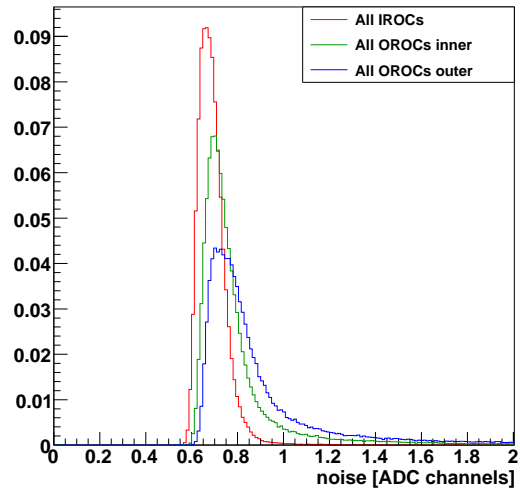
pad size [mm <sup>2</sup> ]	maximum	mean <sub>0</sub> <sup>2</sup>	RMS <sub>0</sub> <sup>2</sup>	> 1 ADC [%]
4 × 7.5	0.67	0.69	0.07	0.6
6 × 10	0.69	0.79	0.19	11
6 × 15	0.71	0.87	0.24	24

Table 4.1: Maximum noise and truncated mean between 0 and 2 ADC-channels and its RMS for the different pad sizes. In addition the fraction of pads above 1 ADC channel is given.

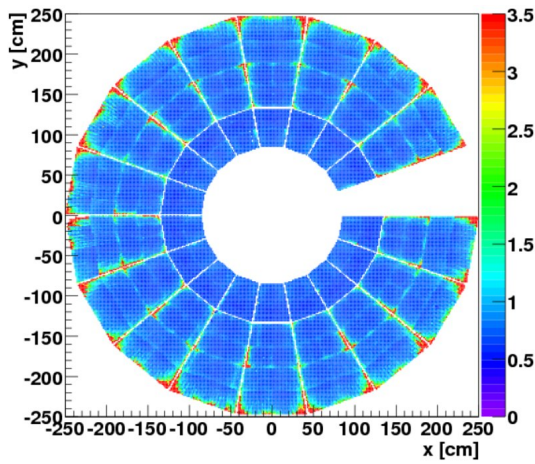
<sup>4</sup>Noise levels larger than 1 ADC channel will be denoted as “high noise”.



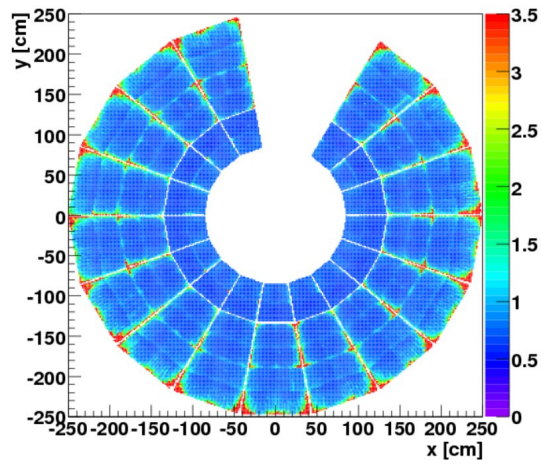
(a) Noise distribution both for all chambers and separately for the different pad sizes (note the log scale!).



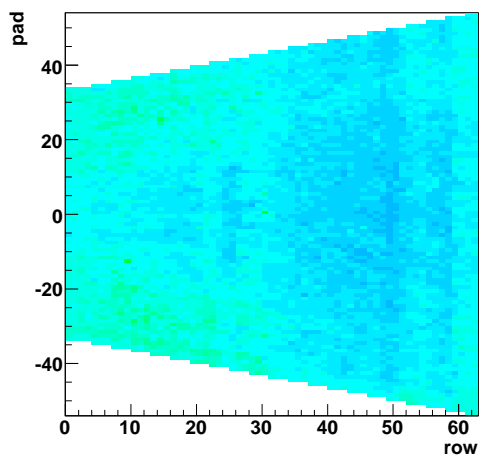
(b) Noise distribution for the different pad sizes, normalised by the number of entries.



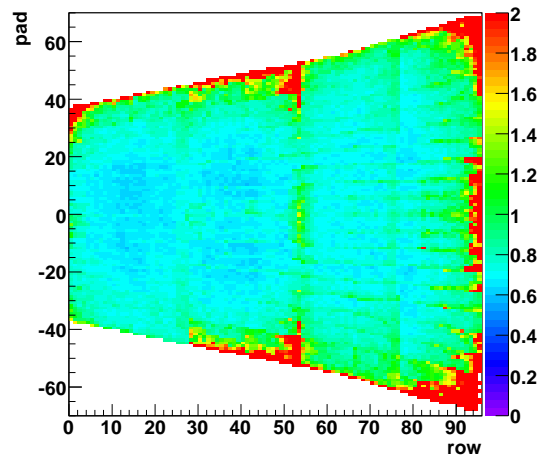
(c) 2D noise distribution on the A-Side



(d) 2D noise distribution on the C-Side



(e) 2D noise distribution in one IROC



(f) 2D noise distribution in one OROC

Figure 4.5: 2D noise distribution in the TPC

In addition a clear pattern is seen for IROC and OROC: The noise within one readout partition increases from the centre to the edges of the partition. It was found that the major part of this effect is due to the increasing track length on the PCB board, connecting the readout pads with the connectors on the backside of the pad plane (see below).

The data shows that a substantial fraction ( $\sim 10\%$ ) of the pads have noise values larger than the quoted acceptable maximum noise level of 1 ADC channel. The last column of Tab. 4.1 shows this fraction separately for the different pad sizes. The largest fraction of high noise pads is found in the outer part of the OROC. In terms of the SNR this is less critical since the larger pads also pick up larger signals. This is, of course, only true if the HV of the sense wires is the same for the inner and outer pads of the OROC, as was the case during the commissioning. Still it is favourable to achieve a noise level as low as possible.

#### 4.3.2.2 Discussion of the Noise Situation

In the final operation one of the main concerns is the data volume produced. To perform zero suppression a threshold is set. Only signals above this threshold will be read out. However, it is only possible to set one threshold for one complete ALTRO chip (16 channels). Therefore, to perform an optimum zero suppression this threshold has to be oriented on the pad with the highest noise level. On the other hand the threshold has to be kept low enough that signals on pads adjacent to the one with the maximum signal are not cut. Cutting the tails of the pad response function (PRF) significantly deteriorates the resolution of the affected space point. Being able to only set the threshold for a group of channels renders more than the 10% of high noise channels problematic.

The discussion above clearly shows the need of a lower overall noise level in the TPC. A detailed understanding of the noise sources is necessary. Towards the end of the commissioning the grounding scheme of the FEE was revised in order to minimise the noise level. However, this was only done after the bulk data taking and for this reason a part of the pads will be excluded from the analysis of the commissioning data, if necessary.

#### 4.3.2.3 Noise Dependence on the PCB Track Length

The noise of charge sensitive amplifiers depends linearly on the input capacitance. The capacitance seen by the PASA chips should in good approximation be given by the capacitance of the readout pad plus the capacitance of the PCB track and the capacitance of the capton cable, which connects the FEE and pads. The capacitance of the PCB track is assumed to increase linearly with its length. Therefore a linear dependence of the noise with the PCB track length is expected.

The correlation of noise vs. track length for the three different pad sizes is shown in Fig. 4.6. The expected linear dependence is seen. A few pads do not follow this trend. In the following those will be quoted as *outliers* (see also below). A few outliers are seen in the IROC, whereas in the OROC the number of outliers increases with the track length. To be able to fit the result with a line a robust option was used. This was chosen to find a subset of 70% of the data giving the best fit result. The results of the fit are listed in table 4.2. The histogrammed deviations from the line fits normalised by the number of entries are shown in Fig. 4.6d.

In order to classify the distance of the datapoints to the line fit, a “truncated sigma” was calculated for each distribution. This was done by applying a gauss fit in a region of  $\pm 0.1$  ADC channels around its maximum. More precisely, in the following a data-point

will be denoted as an outlier if it is more than three sigma away from the line fit in the direction of higher noise values. The sigma values, as well as the maximum accepted noise for the three different pad sizes is summarised in table 4.2.

With this definition 3.8% of the readout channels in the IROCs and 18.7% and 27.0% in the inner and outer part of the OROCs are classified as outliers<sup>5</sup>, respectively. This definition is, of course, more stringent than requiring a value above 1 ADC channel. It demonstrates how many channels suffer from noise sources other than the expected dependence on the input capacitance.

Fig. 4.7 shows the 2D noise distributions of the outliers on the A- (a) and C-Side (b) as well as in how many IROCs (c) and OROCs (d) a pad has been regarded as an outlier.

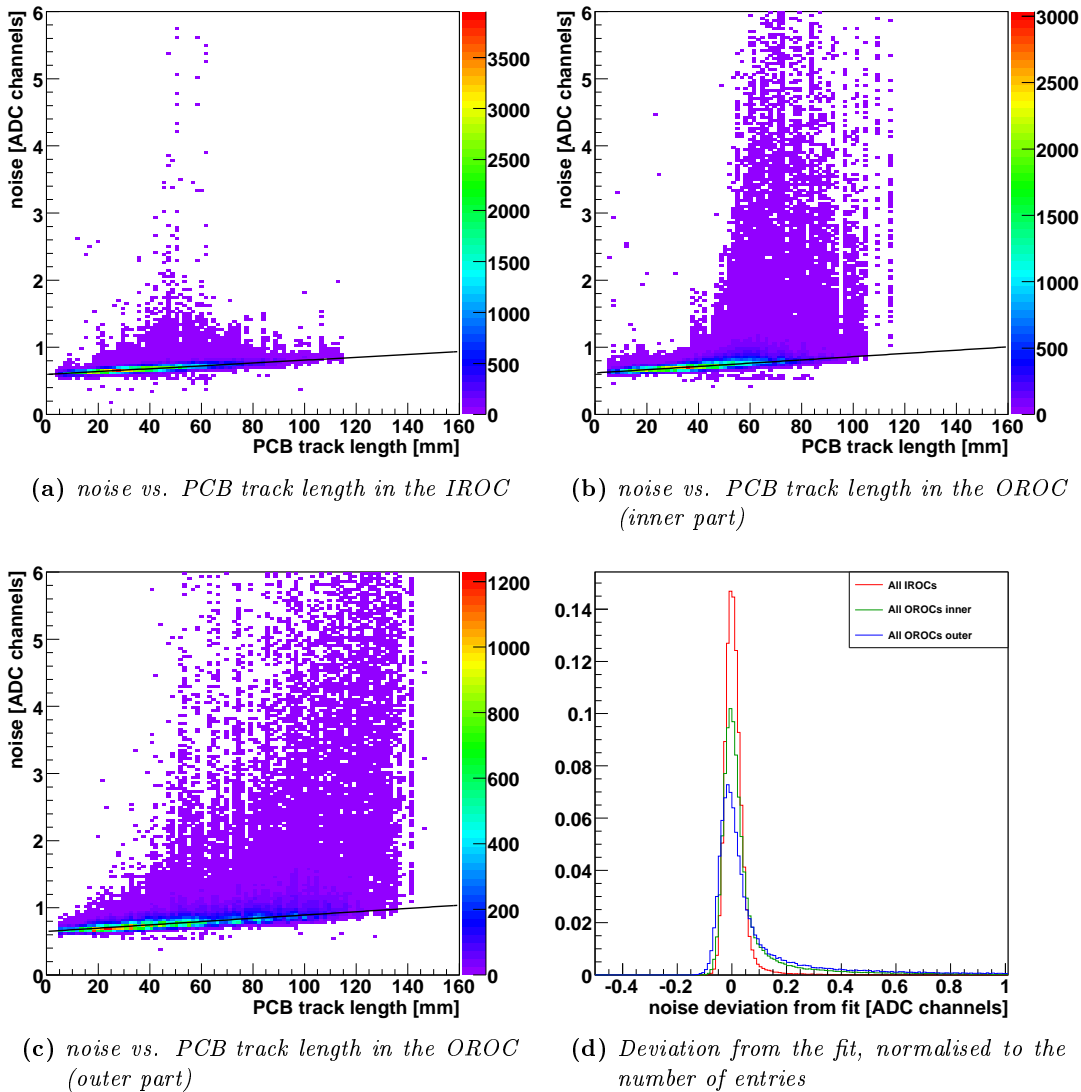


**Figure 4.6:** *Correlation of noise and PCB track length. The black lines show a line fit with robust option.*

<sup>5</sup>For an ideal gaussian distribution one would expect 0.3% of the data to be outside a range of  $\pm 3\sigma$ .

pad size [mm <sup>2</sup> ]	ordinate intersection	slope	sigma	max. noise allowed
$4 \times 7.5$	$5.97 \cdot 10^{-01}$	$2.12 \cdot 10^{-03}$	$2.57 \cdot 10^{-02}$	0.9
$6 \times 10$	$6.19 \cdot 10^{-01}$	$2.42 \cdot 10^{-03}$	$3.15 \cdot 10^{-02}$	1.0
$6 \times 15$	$6.48 \cdot 10^{-01}$	$2.44 \cdot 10^{-03}$	$4.00 \cdot 10^{-02}$	1.1

Table 4.2: Fit parameters of the line fits in Fig. 4.6, sigma of the distributions in Fig. 4.6d and the resulting max. allowed noise ( $3\sigma$  above line fits) for the different pad sizes

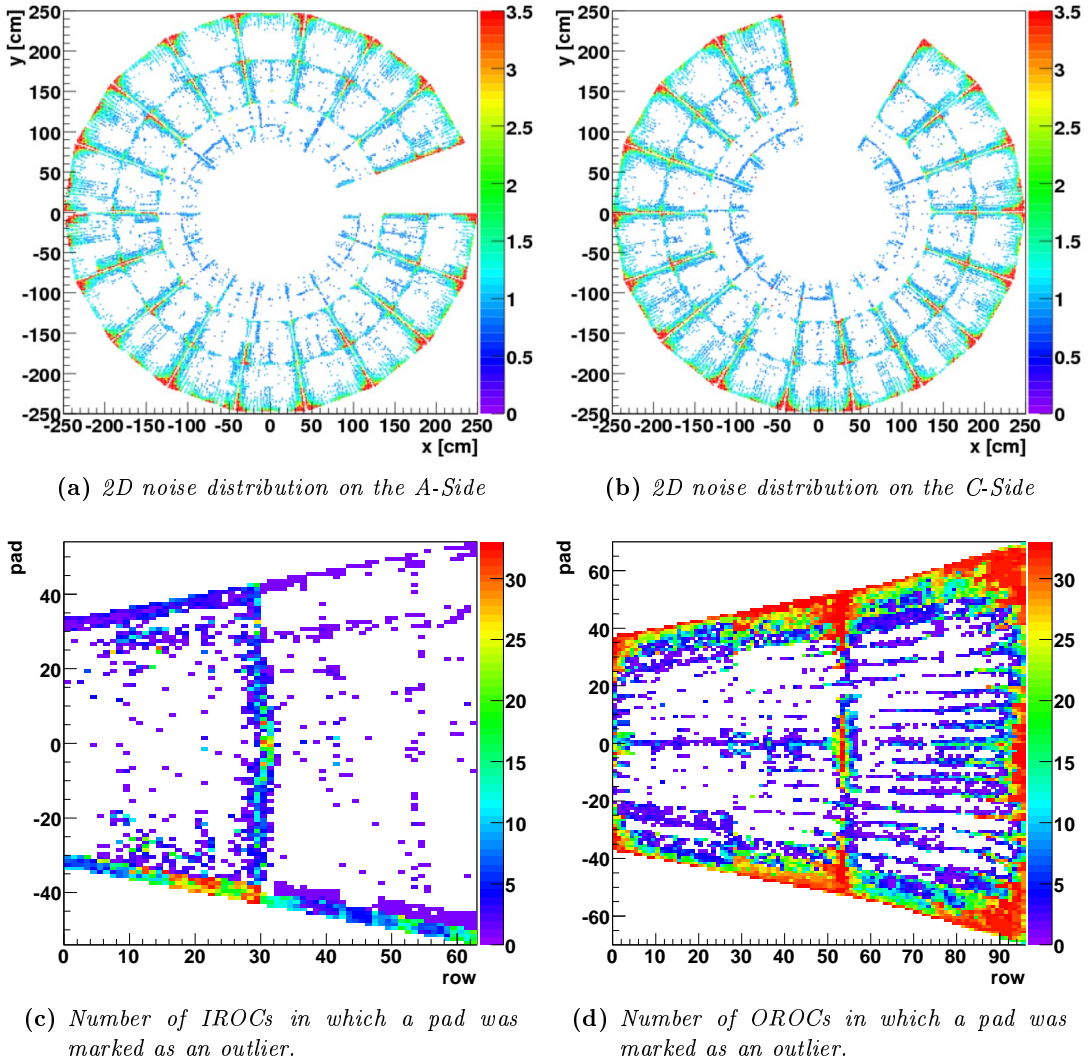


Figure 4.7: 2D noise distribution in the TPC. Shown are only those pads in which the noise is more than  $3\sigma$  away from the line fit shown in Fig. 4.6



For the IROCs three regions with higher noise can be identified (cf. Fig. 4.7c):

- Along the edges in radial direction, generally more pronounced on the side. On this side the capton cables used to connect the last FEC in each of the two readout partitions is longer for technical reasons.
- for nearly all chambers a few pads in the centre,
- for about 30 % of the chambers pads in rows 28 to 32.

For the OROCs one can classify five regions of higher noise (cf. Fig. 4.7d):

- along the edges in radial direction
- in all corners, but much more pronounced at the long edge
- around the centre of rows 92 to 96 (long side of the chamber)
- in the centre of the chamber (row 52 to 55, pads -10 to +10)
- at the edges of rows 52 to 55 (pads 32 to 52 and -32 to -52)

#### 4.3.2.4 The Influence of the Field Cage Voltage on the Noise Behaviour

To determine the influence of the field cage (FC) high voltage (HV) power supply on the noise level of the ROCs, a detailed noise study has been performed for sectors A02 and A03<sup>6</sup> regarding the following configurations:

1. All high voltages turned off
2. Field cage at 1 kV, ROCs turned off
3. Field cage at 10 kV, ROCs turned off
4. Field cage at 20 kV, ROCs turned off
5. Field cage at 50 kV, ROCs turned off
6. All high voltages as in final conditions (FC 100 kV, ROC  $\approx$  1.5 kV)

To classify the overall noise level its maximum, mean and RMS (the last two for a truncation between 0 and 2) as introduced above were calculated. The results are summarised in table B.1 in the appendix and the mean and RMS values are plotted in Fig. 4.8 separately for each pad size.

For all pad sizes the mean and RMS rise with the FC HV, saturating at about 50 kV. For the measured point at 100 kV FC voltage also the ROC voltages are switched on to the nominal values, what does not seem to introduce a further increase in the noise level. The increase of the mean from 0 kV on the FC up to its nominal value of 100 kV is about 11 % for the IROC and inner part of the OROC and 15 % for the outer part of the OROC. The RMS increases by about 15 % for all pad sizes.

To visualise the pad positions where the noise increases, Fig. 4.8 shows the ratios of the different FC high voltage settings above 0 kV (configurations 2-6) to the one at 0 kV (configuration 1). Shown are only pads for which the change was larger than 10 %.

For the OROC of sector A03 (left sector) one can clearly see that the increase in noise is highest in the top left corner, stretching more and more towards the centre of the chamber the higher the voltage is. This strong behaviour is, however, not seen for the OROC of

<sup>6</sup>The naming convention for counting sectors is discussed in Sec. 3.3.6

sector A02 where the noise increases symmetrically from the edges of the outer part towards the centre.

In the IROC of both sectors it is found that with increasing FC voltage a cross-like structure shows up more and more prominently. Along the edges in radial direction as well as on the short side of the chamber the noise also increases slightly with the rising FC voltage.

The noise patterns appearing with the increase of the FC HV are not understood. Obviously they are restricted to some areas within the chamber, instead of showing an increase on all pads simultaneously.

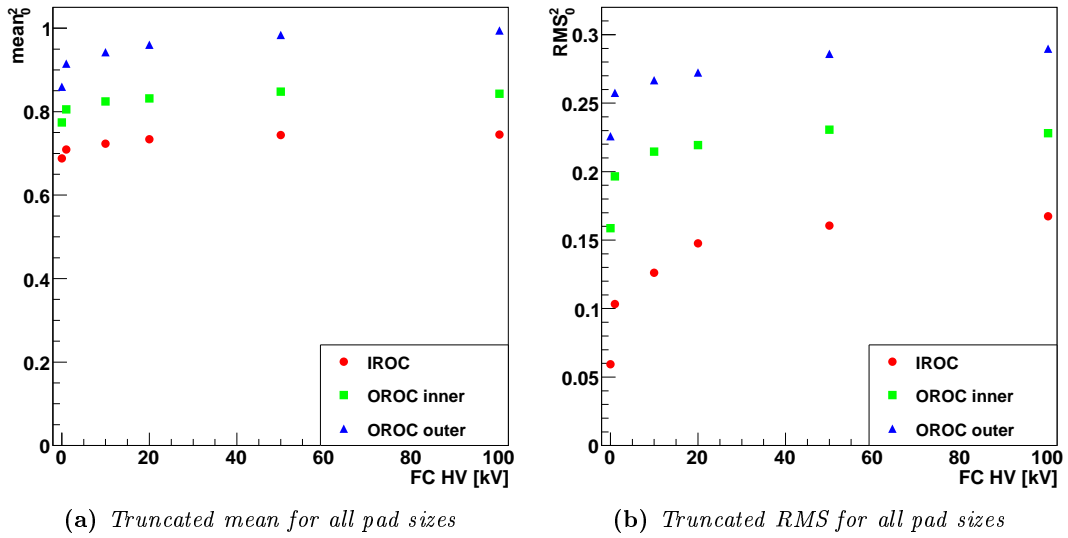
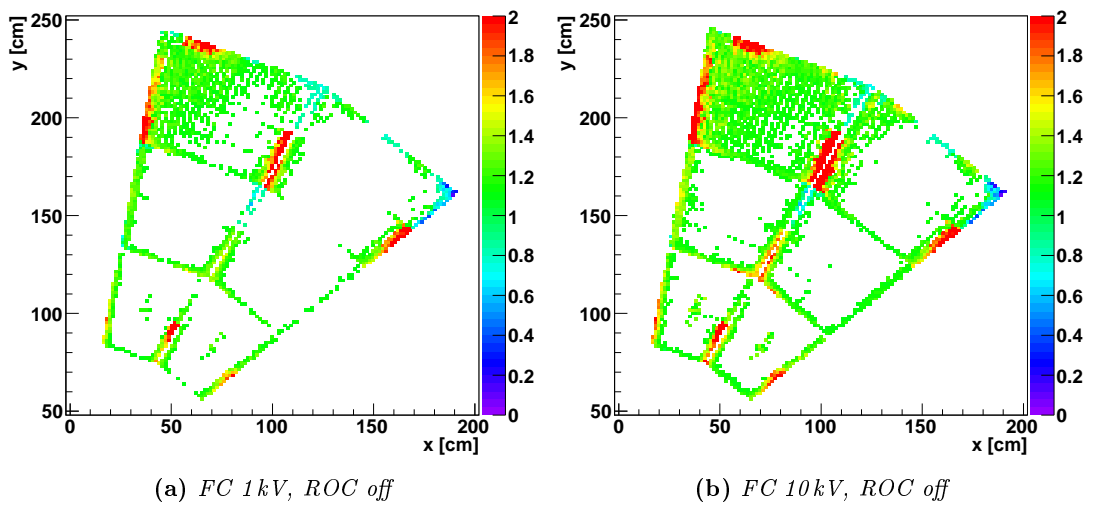
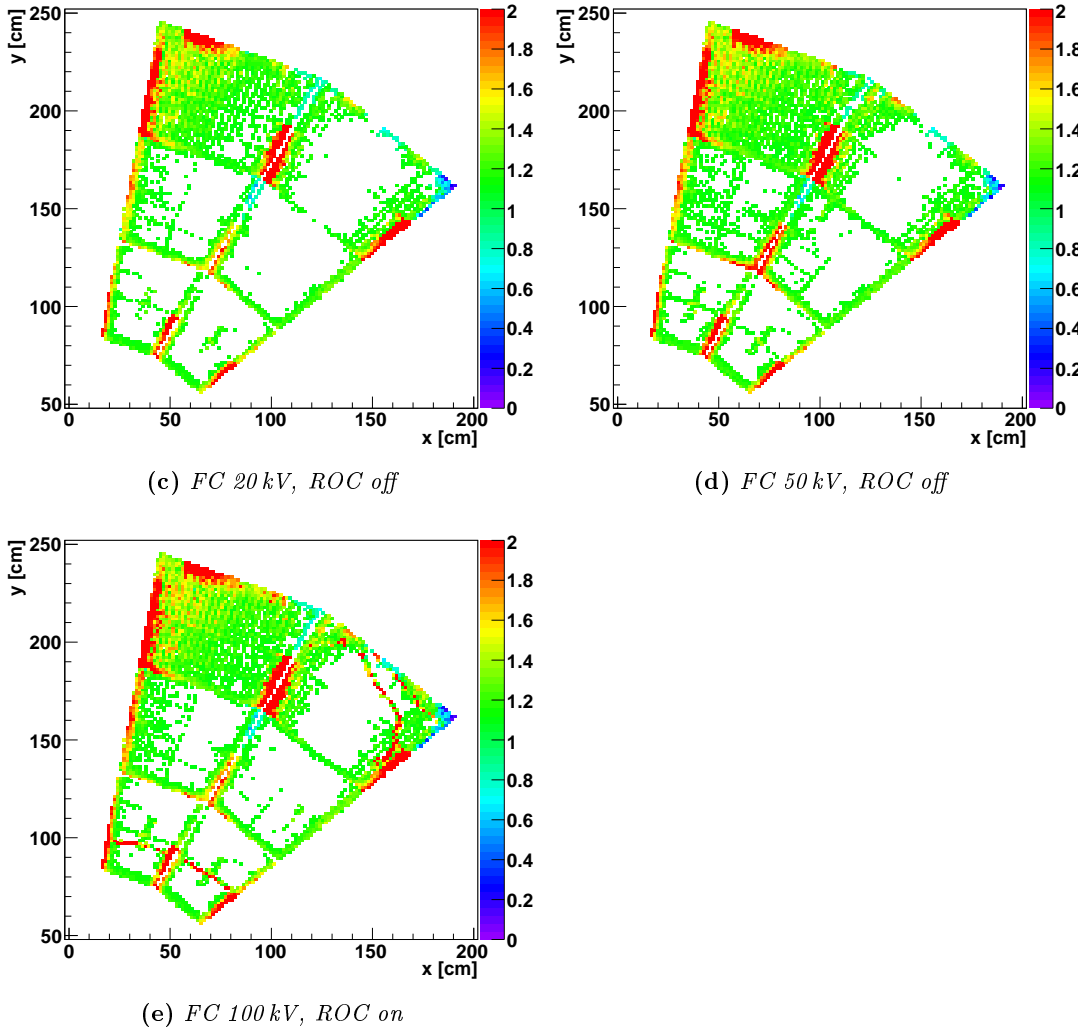


Figure 4.8: Noise as a function of the field cage high voltage





**Figure 4.8:** *Normalised 2D noise distributions. As a reference the data with switched off FC and ROC voltage was used. Shown are only those pads which have a change large than 10 %.*

#### 4.3.2.5 Desynchronisation and the Revision of the FEE Grounding scheme

One expected source of noise results from the CMOS technology used in the front end electronics. The phenomenon is called ‘ground bounce’. In the FEE it occurs when the recorded data is written to the ALTRO memory and causes a large current, which results in a change of the ground potential of the digital circuit. Since the reference ground point on the FEC is the same for the digital and analogue part, the analogue part can be influenced as well. This happens if the impedance between the FEC reference ground and the common reference ground is too large.

The ground bounce effect is of course most dominant if all TPC channels start writing into the memory at the same time. Therefore it was foreseen to be able to desynchronise the start point in time for groups of channels. After optimising the desynchronisation, the coupling to the analogue part can be minimised by optimising the grounding scheme of the FECs.

Towards the end of the commissioning time was reserved to optimise both schemes. Different desynchronisation patterns have been tested. For the optimisation of the grounding scheme measurements were performed in between which only single grounding cables have been removed or exchanged with more massive ones<sup>7</sup>. The tests were performed on a single sector. Afterwards the optimum scheme was adopted for all other sectors.

The lowest noise was obtained with the following configuration:

Desynchronisation scheme:

- First group (ALTRO chips 0 and 2 of each FEC): 0 timebins offset
- Second group (ALTRO chips 1 and 3 of each FEC): 1 timebin offset
- Third group (ALTRO chips 4 and 6 of each FEC): 2 timebins offset
- Fourth group (ALTRO chips 5 and 7 of each FEC): 3 timebins offset

Changes on the grounding scheme:

- in readout partition three the grounding cables of the first and last four FECs have been exchanged
- in readout partition four the grounding cables of the first and last five FECs have been exchanged
- in readout partition five the grounding cables of the first and last six FECs have been exchanged and all other cables were removed

The obtained 2D noise distribution after the modification is displayed in Fig. 4.9.

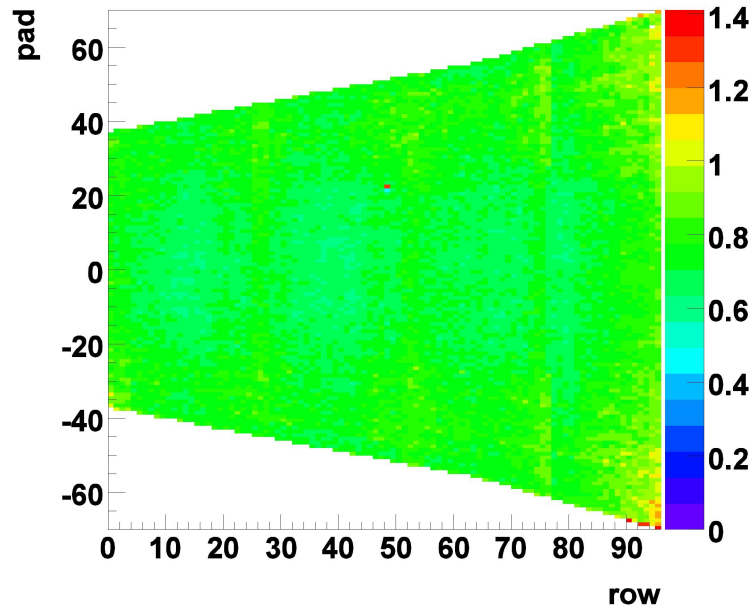


**Figure 4.9:** *2D noise distribution after the change of the FEE grounding scheme*

With the new configuration only single pads show noise values above 1.1 ADC count. The bulk of the pads have values below 1 ADC channel. The high noise regions of the

---

<sup>7</sup>The standard grounding cables are insulated with the dimensions  $10\text{ cm} \times 1.5\text{ mm}^2$ . The alternatively used cables are flat cables with the dimensions  $5\text{ cm} \times 1\text{ cm} \times 3\text{ mm}$ .

corner have vanished. The only structure which is left results from the different PCB track length.

### 4.3.3 Calibration Pulser

To determine the shaping characteristics of the front-end electronics used, which determines the exact timing and gain of each pad signal, it is possible to inject a pulse on the cathode wire plane. This induces directly a signal on the pads, without gas amplification. Therefore the measured signal of same sized pads should occur at the same time and have the same integrated charge. However due to manufacturing tolerances of the PASA chips the shaping of the signal may vary, resulting in the detection of different arrival times and integrated charges.

In order to correct for these effects, from time to time so called ‘‘Calibration Pulser Runs’’ will be taken to monitor the chip characteristics. The results will be stored in the OCDB and used in the offline reconstruction.

Fig. 4.10 shows a typical pulser signal of one channel. To analyse raw data taken with the Calibration Pulser a calibration class (‘AliTPCCalibPulser’, see appendix A) has been developed. This class accumulates a number of pulser events and calculates the position, width and area for each pad signal. The timing information for pads within one chamber is shifted by their mean time in order to get the relative timing differences within one ROC. For the same wire geometry the integrated signal depends linearly on the pad size. To allow for this trivial effect the integral is scaled by the pad area.

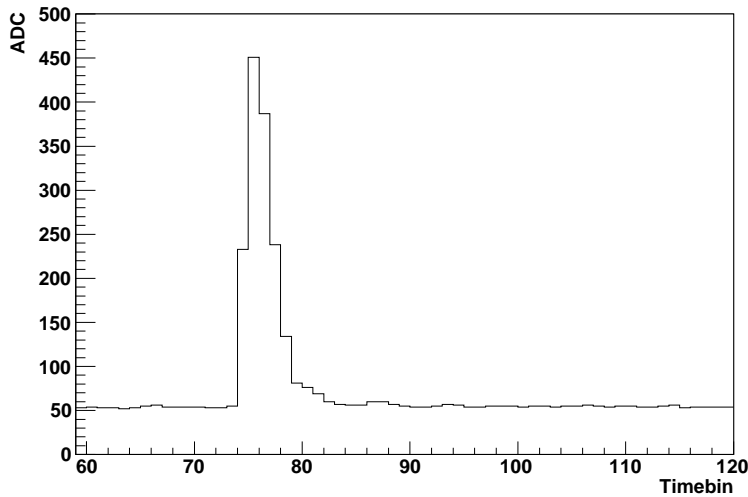


Figure 4.10: *Typical Calibration Pulser signal shape in one readout channel*

#### 4.3.3.1 Timing Differences

Fig. 4.11 shows the timing differences within one IROC (a) and OROC (b), respectively. Clear patterns can be seen: Groups of 16 pads are found, showing nearly the same values. The differences between the groups can be larger. It turned out, that each group corresponds to one PASA chip. This becomes evident when looking at (c) and (d) of the same figure, where pads which belong to the same chip are shown with the same colour.

In Fig. 4.12 the timing differences for all sectors are shown. A clear peak around zero can be seen with a small shoulder on the right side. To determine the width of the distribution it was fit with a gauss function in the range of  $\pm 0.2$ . A sigma of 0.062 was found, corresponding to 6.2 ns. Considering a drift velocity of about 2.7 cm/ $\mu$ s, this would yield an error in the position resolution of about 170  $\mu$ m. Since this effects the clusters assigned to a track only randomly and considering the intrinsic cluster position resolution of 300-800  $\mu$ m (given by the diffusion and therefore depending on the  $z$ -position) this is a second order effect.

The red lines in the plot mark a  $\pm 4\sigma$  range around the peak. Points outside this range will be denoted as outliers. Figure 4.13 shows a 2D view of outlier pads for the A-Side (a) and C-Side (b), respectively. The outlier pads are nearly all distributed along the radial edges of the chambers.

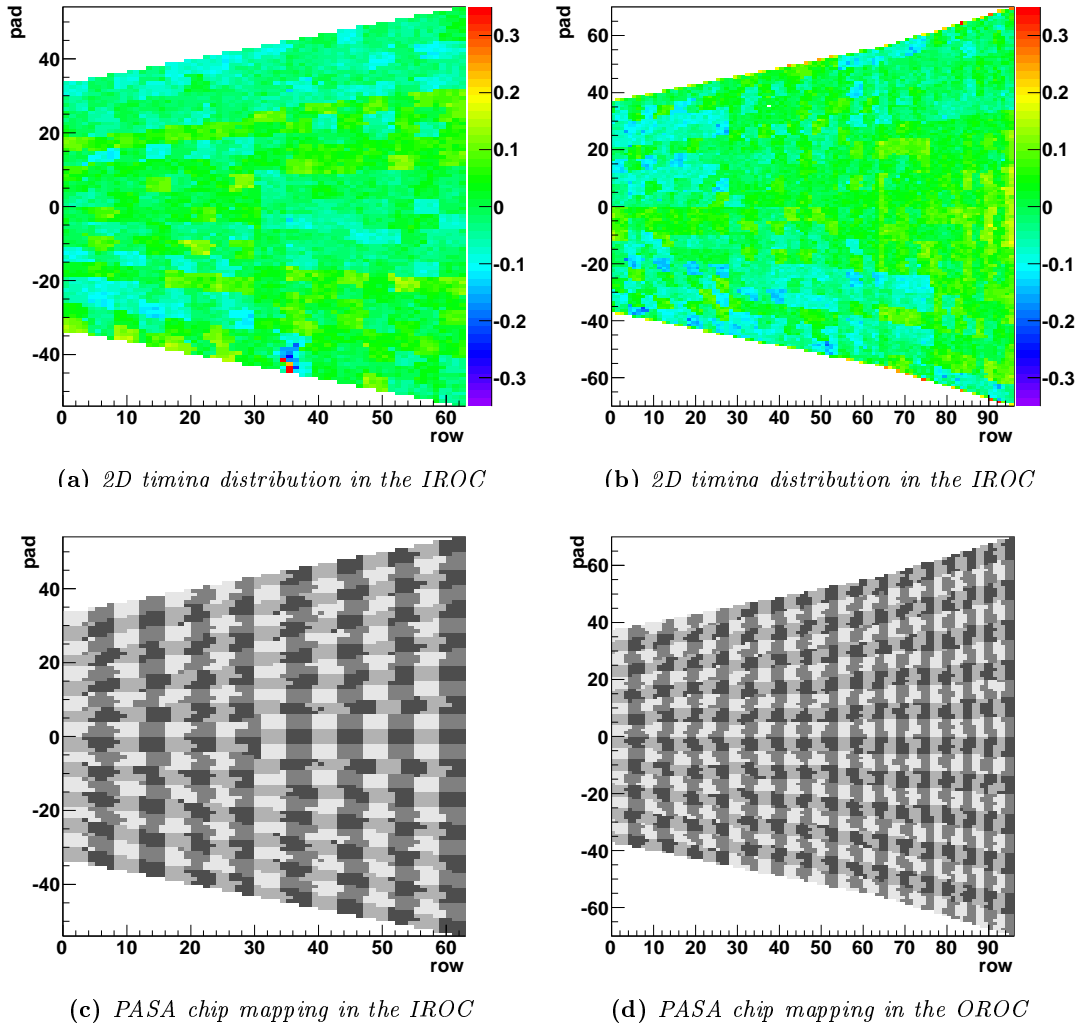
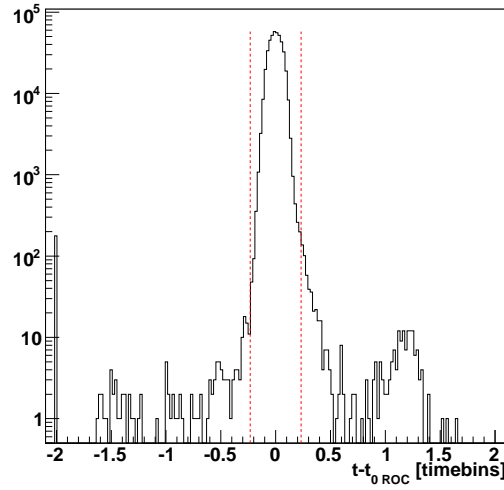
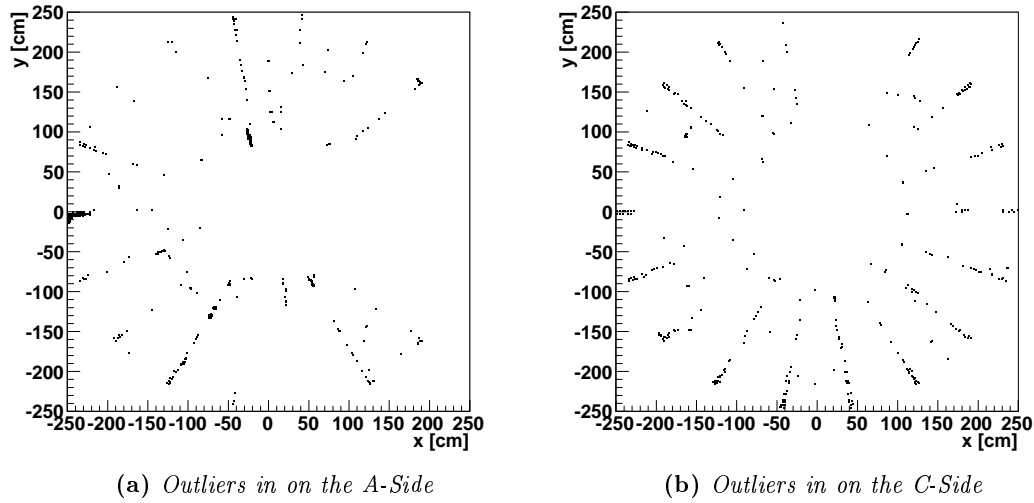


Figure 4.11: Relative timing differences within one ROC in units of timebins.



**Figure 4.12:** *Distribution of timing differences within all sectors. The red dashed lines mark the cuts for outliers.*



**Figure 4.13:** *2D Outlier distribution from the Calibration Pulser time analysis*

#### 4.3.3.2 Charge Differences

In Fig. 4.14 the measured charge normalised by the mean charge per chamber is shown. Plots are given for the A-Side (a) and the C-Side (b) as well as for one IROC (c) and OROC (d). Conspicuous are complete padrows with higher and lower gain, respectively. Those were identified to have an improperly connected anode or cathode wire, called “floating wire” in the following. The PASA structure already discussed above, is also seen in the charge information for the IROC and OROC.

The normalised charge distribution for all sectors is displayed in Fig. 4.15. A peak around one is seen with a small shoulder on its right side. A gaussian function was fit in a window of  $\pm 0.1$  around the maximum of the distribution. The obtained sigma is 0.028, corresponding to gain variations of 2.8%. Considering the aimed  $dE/dx$  resolution of 6% this effect has to be taken into account.

The red dotted lines in Fig. 4.15 correspond to a  $4\sigma$  window around the peak. Pads outside this range will be, as also described in the case of the timing distribution, regarded as outliers. The positions of pads such marked as outliers are displayed in Fig. 4.16. It shows that nearly all pads along the radial edges are regarded as outliers. In addition those padrows with a floating wire lie out of the four sigma range.

In sector A15 a lot of pads in the outer part of the OROC are also marked as outliers. The reason is that during the measurement on this sector the drift voltage and chamber high voltages had been turned on, resulting in an increase in the noise (see 4.3.2.4). This obviously influenced the pad signal significantly and demonstrates the need of a low noise (<1 ADC channel) behaviour.

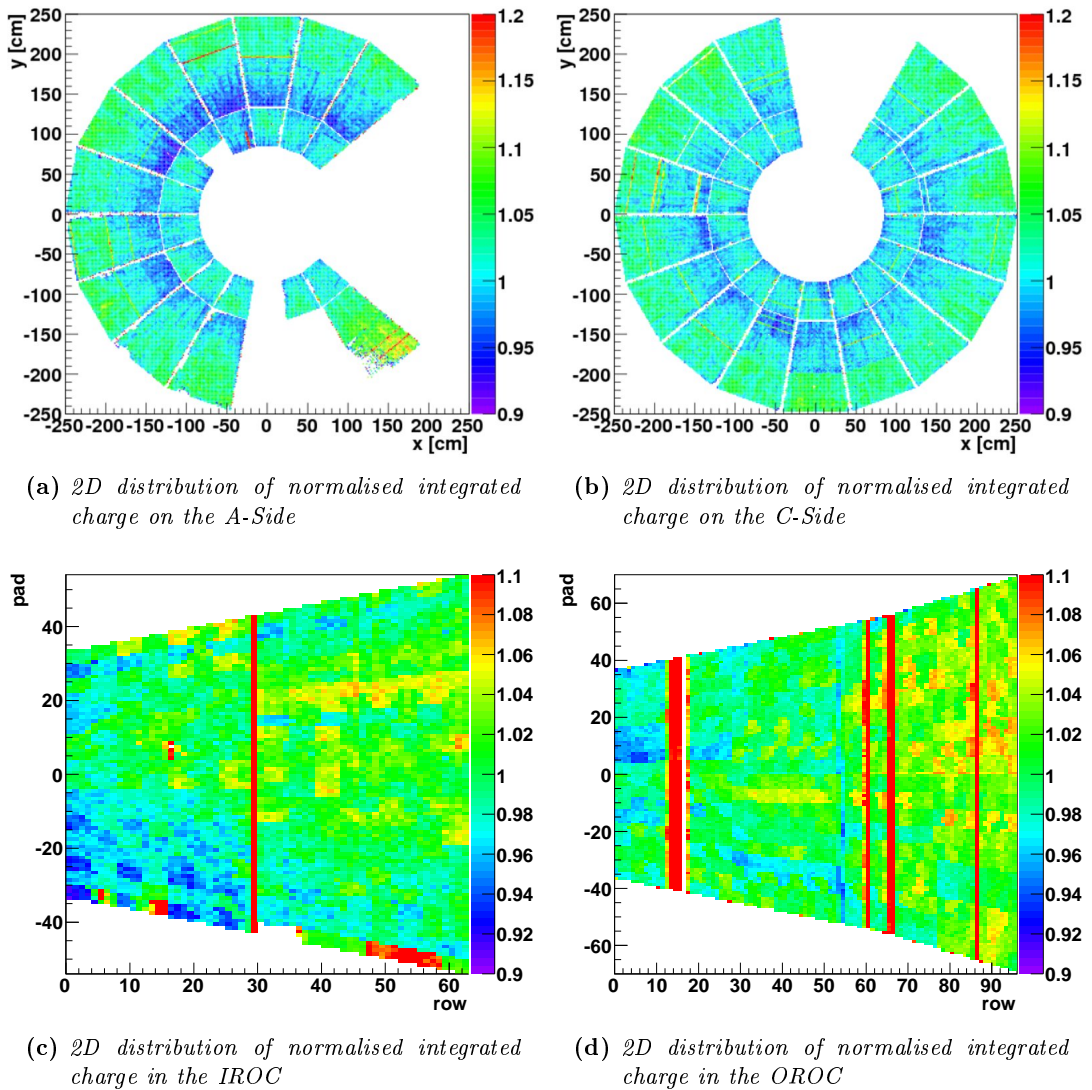
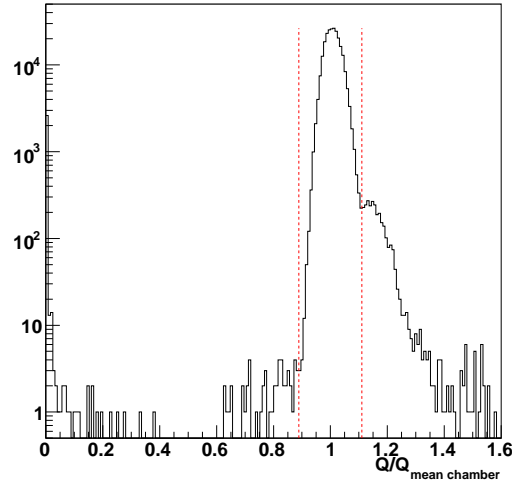
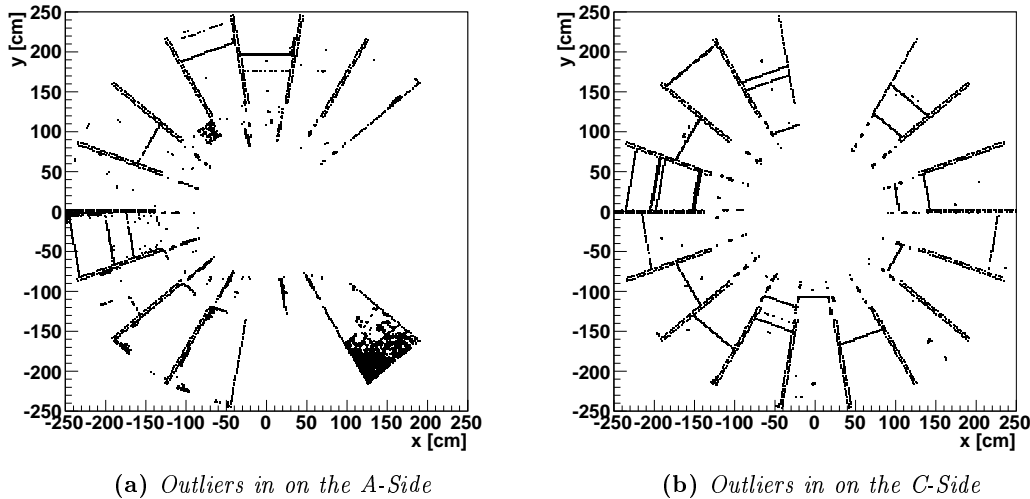


Figure 4.14: Normalised charge distributions





**Figure 4.15:** Normalised charge distribution for all sectors. The red dashed lines mark the cuts for outliers.



**Figure 4.16:** 2D Outlier distribution

#### 4.3.4 Laser Events

Most metallic surface have work functions below the photon energy (4.66 eV) of the laser used for the laser calibration system. Thus, if a photon hits the aluminised central electrode, a photo electron is emitted which starts to drift towards the readout chambers in the electric field. Due to the large amount of diffusely scattered photons the complete central electrode emits photo electrons that can be measure on each pad of the ROCs.

The information from the central electrode, as well as the laser rays themselves can be used to measure the misalignment of the ROCs. Data from the CE will also be used to monitor the drift velocity, being a very sensitive indicator for the gas quality.

As described in the introduction one objective of this commissioning was to put the laser system (see Sec. 3.4.1) into operation. Thus a large part of the data was taken with a laser trigger. The projection of the design positions and measured rays of the system to the  $xy$ -plane are displayed in Fig. 4.17.

In the course of this work a calibration class ('AliTPCCalibCE', see appendix A) was developed, which analyses the signals from the central electrode. A number of events is accumulated and for each pad the arrival time, signal sum and signal width is calculated. The stored timing information is the difference of the drift time measured on each single pad to the mean drift time of the corresponding readout side. In addition for each event and each readout chamber the results of a two dimensional linear and parabolic fit are stored, as well as the mean arrival time and mean signal sum.

The analyses of the laser rays is discussed in Ref. [65]. Results of the CE signal analysis is given below.

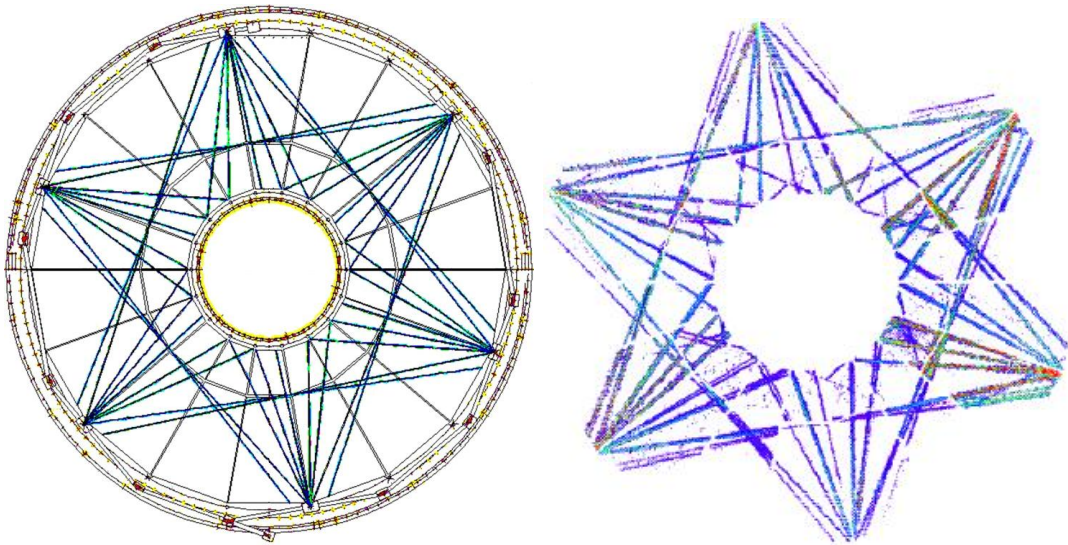


**Figure 4.17:** *Laser ray positions - design [48] (right) and measurements (left).*

#### 4.3.4.1 Corrections with the Timing Information from the Calibration Pulser Analysis

Fig. 4.18 shows the effect of correcting the CE arrival times with the results from the previously discussed Calibration Pulser events. In pad (a) the uncorrected time signal within one OROC is displayed as a function of row and pad. The PASA structure mentioned in the Calibration Pulser section is clearly visible. After the corrections have been applied (b) the structure has vanished and the arrival times show a smooth surface. A plane function was fit to both results. Pads (c) and (d) show the distribution of the residuals to the fit for both cases. After the timing corrections the width of the distribution is about 35 % smaller, showing its success.

The 2D histograms of the OROC also show that nearly all edge pads in the pad rows have lower values than the surrounding pads. These have already been determined as outliers in the Calibration Pulser analyses and will be excluded in the further analysis.

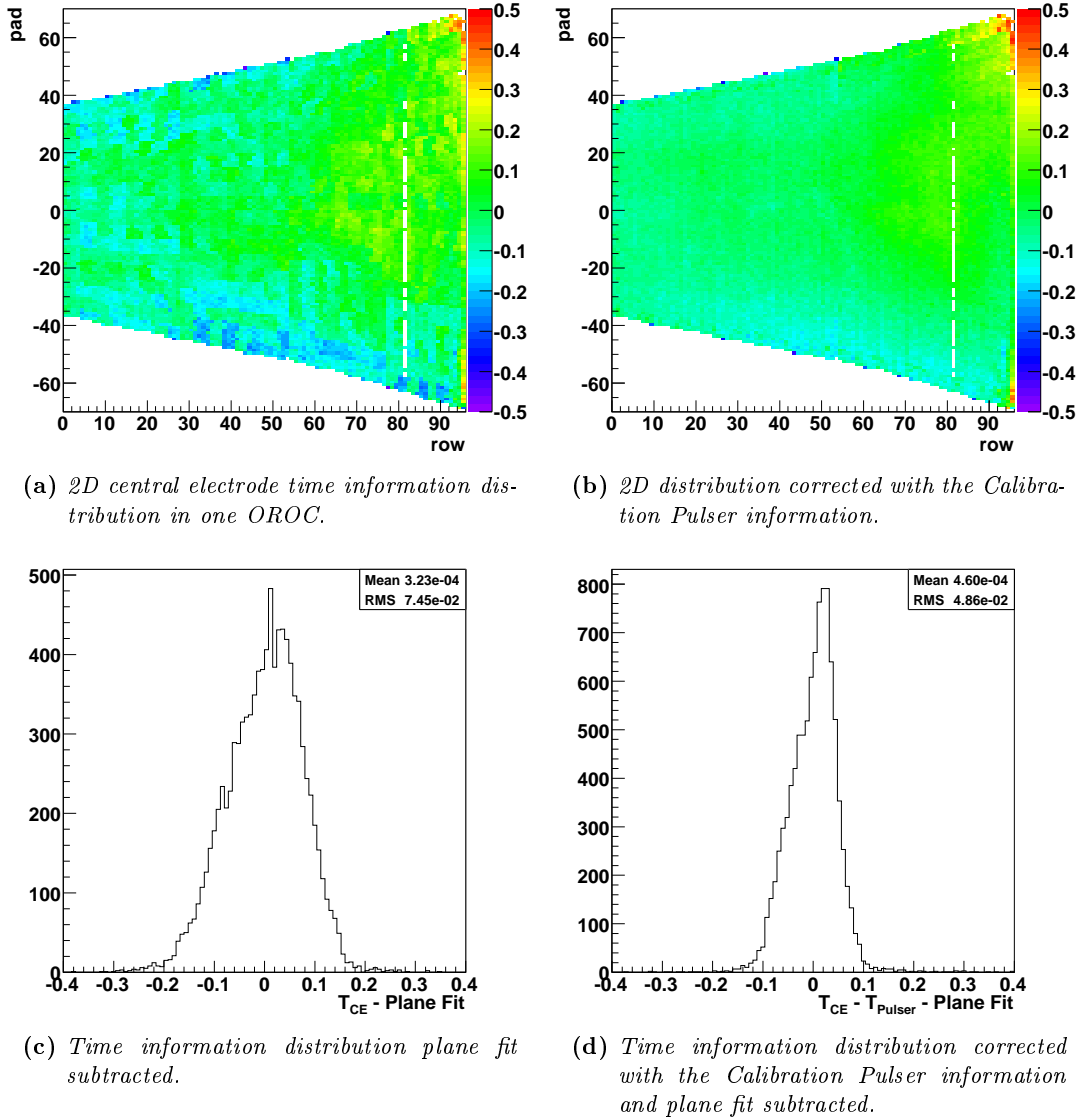


**Figure 4.18:** Central electrode time information in one OROC. Effect of Calibration Pulser corrections.

#### 4.3.4.2 Charge Distribution

The charge distribution measured in laser events is displayed in Fig. 4.19 for the A- and C-Side. Six sectors clearly show a different behaviour than the others: A08,A09 and C11-C14. A08,A09,C13 and C14, having about a factor of three larger signal, were taken with a higher laser intensity. Sectors C11 and C12 do not show any signal. The reason is that for these sectors the gating grid has been close to check its efficiency.

On the A-, and less prominent on the C-Side, bands of lower signals are observed. This is due to the fact, that the central electrode is made out of three pieces, glued together in overlap regions. These regions seem to have a different work function and will be excluded from further analysis. Mathematical conditions describing the geometry of the regions are summarised in table 4.3. Side A has three narrow and two wide regions, Side C two narrow and two wide. They are numbered from top to bottom and named by the pattern <side><width><num>. E.g., CN1 is the first (top) narrow region on the C-Side.

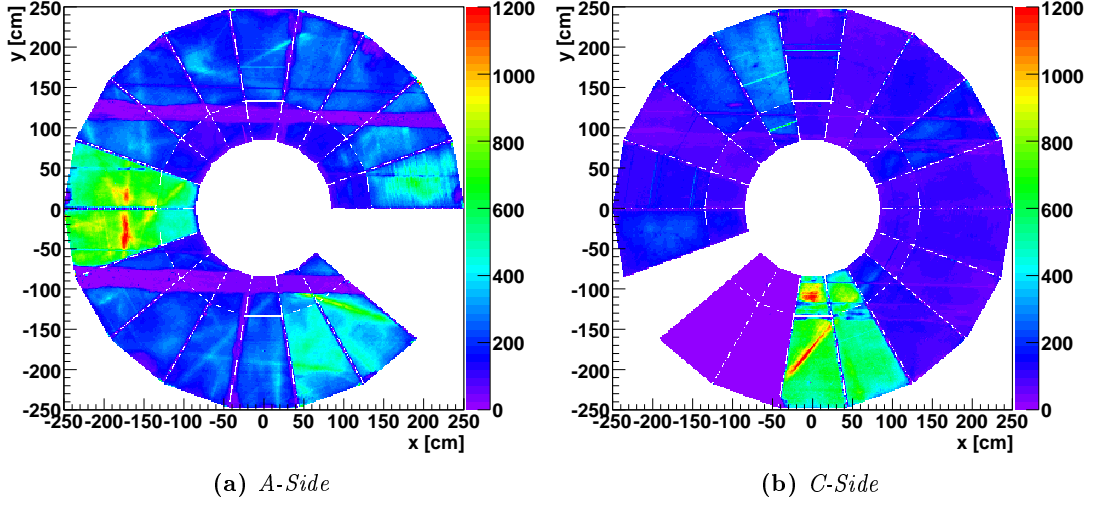


Figure 4.19: Signal sum on the A- and C-Side

cut name	condition
AN1	$ gy - (149.5 - 0.028 * gx)  < 1.5$
AN2	$ gy - (45.4 - 0.023 * gx)  < 1.5$
AN3	$ gy - (-56.8 - 0.026 * gx)  < 1.5$
AW1	$ gy - (115.6 - 0.032 * gx)  < 12$
AW2	$ gy - (-91.8 - 0.029 * gx)  < 13$
CN1	$ gy - (115.80 - 0.024 * gx)  < 1.5$
CN2	$ gy - (-90.88 - 0.024 * gx)  < 1.5$
CW1	$ gy - (82.50 - 0.027 * gx)  < 12$
CW2	$ gy - (-125.4 - 0.024 * gx)  < 12$

**Table 4.3:** Mathematical conditions for the outlier strips of the central electrode.  $gx$  and  $gy$  denote the  $x$  and  $y$  position in the global coordinate frame, the unit is cm. For a description of the cut names see text.

#### 4.3.4.3 Missalignment of the Readout Chambers

To study the misalignment of the readout chambers the time information from the central electrode can be used. Since the CE is a smooth surface, the observation of discontinuities in the arrival times measured by the ROCs is interpreted as a misalignment of the chambers. In addition the CE and end plates might not be parallel, changing the drift field as well as the drift length.

On top of the mechanical alignment, the drift time is influenced by the drift velocity. In the large volume of the TPC temperature gradients might play a role, as well as a barometric pressure gradient from top to bottom of the detector.

Field distortions also influence the drift time. Especially for the setup of the commissioning systematic effects are expected. Since only two sectors were powered at a time, their anode wire high voltage as well as the voltages on the cover and gating grid change the position of the zero volt equi-potential plane with respect to all other chambers and cause a global distortion of the drift field. In addition in the proximity of the chamber edges local field distortions can occur.

Summarised the following factors are identified to influence the drift time:

- Mechanical alignment of the ROCs in the end-plates,
- relative mechanical alignment of central electrode and end-plates,
- drift velocity differences due to temperature and pressure gradients,
- field distortions.

While for the first point a smooth behaviour is expected only within the local readout chamber coordinate system (“local misalignment”), points two and three are expected to be smooth functions of the global coordinates and cannot be distinguished easily (“global misalignment”). For this reason these two will be treated as one effect.

**Global Misalignment** Fig. 4.20 shows the mean drift time of all chambers on the A- and C-Side as a function of the row number (radius). On the A-Side the arrival time increases with the row number, whereas on the C-Side nearly no slope is seen. The slope is an indicator for a relative conical misalignment of the CE and the ROCs (or end-plate). Another possible explanation is a global distortion of the drift field. A more detailed analysis is given below.

The gap between IROC and OROC results from their different wire geometry (cf. Sec. 3.3.4). While the gating and cathode wires have the same distance to the CE for both chamber types, anode wires and the pad plane of the IROC are 1 cm and 2 cm closer to the CE, respectively.

In addition edge effects are observed for the innermost and outermost padrows. This is interpreted as local field distortions caused by not yet properly tuned cover, skirt and edge wire voltages. For the following analysis the first eight padrows of the IROC and last eight padrows of the OROC will therefore not be used.

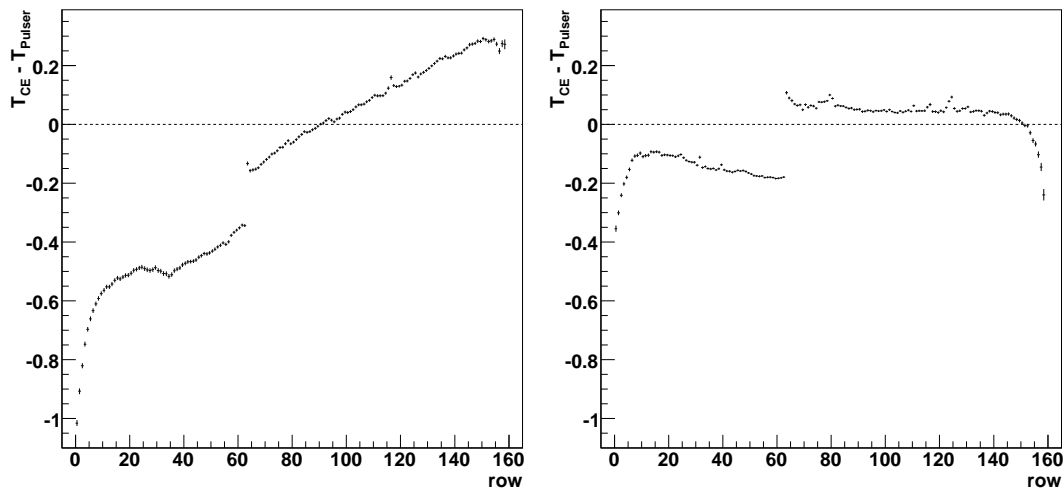


**Figure 4.20:** Mean radial dependence of the central electrode drift time of all chambers on the A-Side (left) and C-Side (right).

The global misalignment can be described by the following function:

$$z = z_0 + m_{xg} \cdot x_g + m_{yg} \cdot y_g + m_{xl} \cdot x_l + m_{yl} \cdot y_l, \quad (4.1)$$

where  $z$  are the  $z$ -coordinates of central electrode, given by  $z = v_{drift} * (T_{CE} - T_{Pulser})$ ,  $m_{xg}$  and  $m_{yg}$  are slopes in global x ( $x_g$ ) and global y ( $y_g$ ) direction, describing a relative trapezoidal misalignment of the CE and the end-plates and  $m_{xl}$  is the slope in local x ( $x_l$ ) direction, describing a relative conical deformation.  $m_{yl}$  would describe a common rotation of each individual chamber around the local x-axis and is expected to be zero within the estimated error.

Due to the two sector tests during the commissioning the relative alignment in between the measured pairs of sectors is lost (change of the environment variables). For this reason it does not make sense to fit the data of all sectors at once with equation 4.1. Instead each sector will be fit with a 2D parabolic function and the slope parameters from the linear part ( $\partial z/\partial x_l$  and  $\partial z/\partial y_l$ ) will be analysed. A parabolic function was used to fit the data, because the second derivative in local  $x$  and local  $y$  direction was observed to be non-zero. The reason could be an electrostatic wire sag and local field distortions. This would cause a slightly different distance of the wire centres to the pad plane (and CE) compared to the wire edges.

In order to perform this analysis eqn. (4.1) is transformed to the local coordinate system of each sector. This is done by a rotation with the angle  $\alpha = \text{sector} \times 20^\circ$  :

$$\begin{aligned} x_g &= x_l \cdot \cos(\alpha) - y_l \cdot \sin(\alpha) \\ y_g &= y_l \cdot \cos(\alpha) + x_l \cdot \sin(\alpha) \end{aligned}$$

Inserting these into 4.1 and building the derivatives with respect to  $x_l$  and  $y_l$  yields:

$$\begin{aligned} \frac{\partial z}{\partial x_l} &= +m_{xg} \cdot \cos(\alpha) + m_{yg} \cdot \sin(\alpha) + m_{xl} + 0 \\ \frac{\partial z}{\partial y_l} &= -m_{xg} \cdot \sin(\alpha) + m_{yg} \cdot \cos(\alpha) + 0 + m_{yl} \end{aligned}$$

To obtain the values for the slopes  $m$ , the results from the parabolic fits ( $\partial z/\partial x_l$  and  $\partial z/\partial y_l$ ) will be fit with one common function:

$$f(\xi_1, \xi_2, \xi_3, \xi_4) = m_{xg} \cdot \xi_1 + m_{yg} \cdot \xi_2 + m_{xl} \cdot \xi_3 + m_{yl} \cdot \xi_4 \quad (4.2)$$

Where  $\xi_1, \xi_2$  and  $\xi_3, \xi_4$  has to be replaced by  $(\pm)[\sin(\alpha)|\cos(\alpha)]$  and  $[1|0]$ , respectively.

In figures 4.21 and 4.22 the measured slopes in local x and local y direction are displayed for the IROCs and OROCs of the A-Side and C-Side separately. Clear patterns caused by the two-sector testing procedure are visible.

The error bars given correspond to the measurement error (100  $\mu\text{m}$ ) of the geometer measurements (cf. Sec. 4.3.1). Due to the different distances of the survey points, the errors are different for the two chamber types and the derivatives in local  $x$  and  $y$  direction. The statistical errors

Obviously the systematic errors introduced by the testing procedure are larger than the precision of the mechanical alignment. For this reason no conclusive results can be obtained about the local misalignment.

As described above, a function of the form 4.2 was fit to the results, to obtain the values for the global slopes. The solid lines in the figures show the results of the fits. On each readout side one function was fit to the OROCs and IROCs separately. Table 4.4 summarises the results of the global misalignment.

Two effects can be distinguished:

1. A top bottom effect, described by the  $m_{gy}$  parameter. This effect is symmetric with

reference to the CE and is interpreted as a temperature and pressure gradient inside the TPC volume. Over the full height of the TPC (5 m) this would correspond to an  $\Delta z$  of about 4.3 mm. This result is obtained by using the average value of the A- and C-side which was calculated for the OROCs. Over the full drift length (2500 mm) this corresponds to a deviation of about 1.7‰. It can be explained by a temperature difference of about 570 mK.

2. A (virtual) conical deformation, described by the  $m_{lx}$  parameter. This effect is non symmetric wrt the CE. It can either be interpreted to be caused by a slightly too high force on the I-bars, which had been installed on the A-Side during the commissioning, or a global distortion of the drift field. For the A-side the results correspond to a  $\Delta z$  between the inner and outer radius of the end-plate (1.6 m) of about 2.5 mm. A mechanical misalignment of this size can be safely excluded by the precision of the geometer measurements. Therefore a distortion of the drift field is much more probable.

Within the estimated errors no common effect in either global x or local y is observed. This is within expectations.

The results of this study support the importance of the aimed temperature stability and homogeneity of 0.1 K in the final environment. It is also obvious that a systematic study for different voltages on the cover, edge wires and gating grid has to be carried out in order to minimise field distortions.

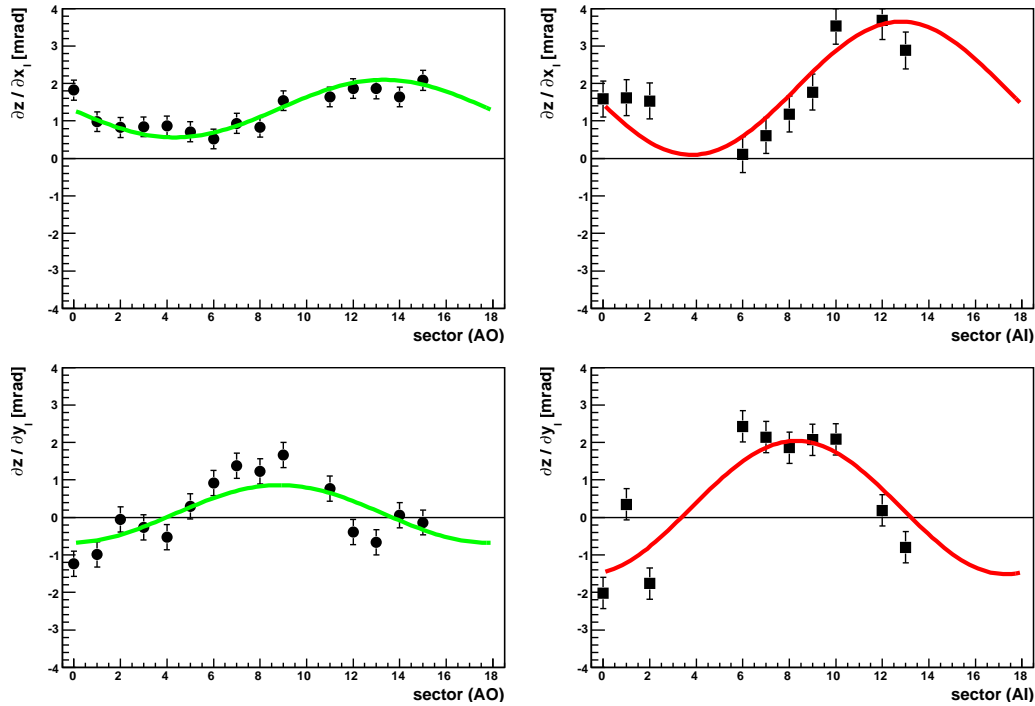


**Figure 4.21:** Measured derivatives in local  $x$  and local  $y$  on the A-side. The left figures show the results for the OROCs, the right figures for the IROCs. Solid lines show the results of a fit with eqn. 4.2

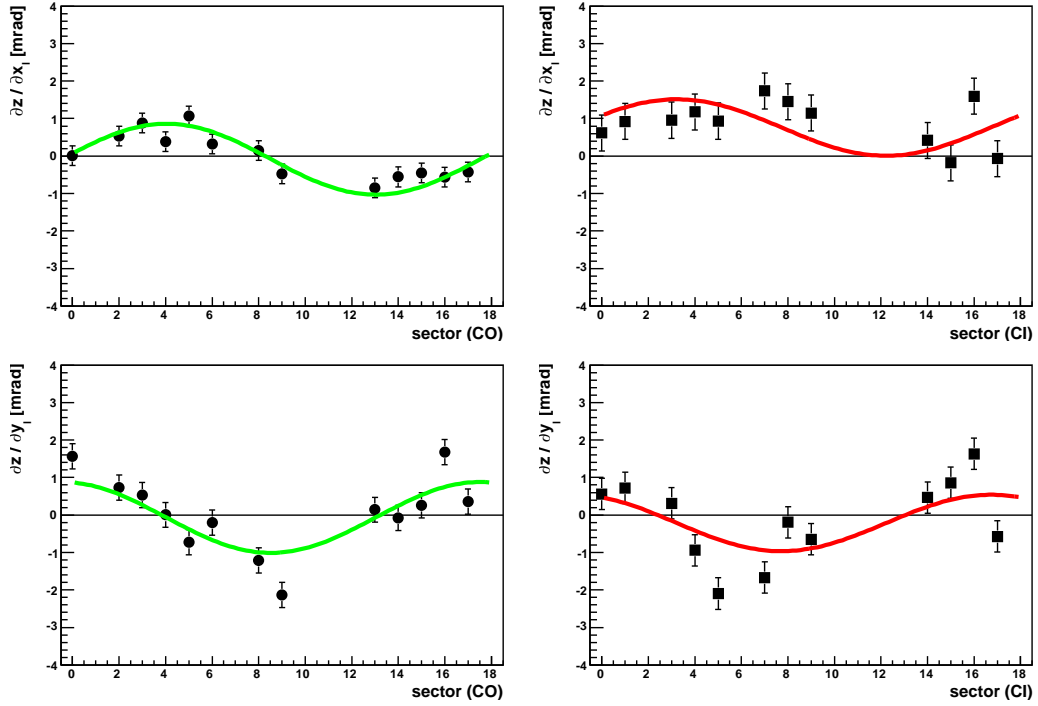


**Figure 4.22:** Measured derivatives in local  $x$  and local  $y$  on the C-side. The left figures show the results for the OROCs, the right figures for the IROCs. Solid lines show the results of a fit with eqn. 4.2

parameter (given in mrad)	A-Side		C-Side	
	OROC	IROC	OROC	IROC
$m_{xg}$	$0.088 \pm 0.104$	$-0.126 \pm 0.427$	$-0.010 \pm 0.118$	$0.202 \pm 0.362$
$m_{yg}$	$-0.763 \pm 0.101$	$-1.773 \pm 0.418$	$0.946 \pm 0.117$	$0.725 \pm 0.355$
$m_{xl}$	$1.330 \pm 0.092$	$1.873 \pm 0.455$	$-0.085 \pm 0.106$	$0.761 \pm 0.385$
$m_{yl}$	$0.093 \pm 0.117$	$0.264 \pm 0.395$	$-0.065 \pm 0.134$	$-0.213 \pm 0.336$

**Table 4.4:** Results of the global misalignment study

#### 4.3.4.4 Driftvelocity Measurements

The electron drift velocity is very sensitive to changes in the TPC gas properties such as temperature, pressure and composition. In order to be able to reconstruct space points with a high resolution, it is essential to know the drift velocity with high precision. To monitor the drift velocity a dedicated device ('Goofie' [52]) has been developed.

Another possibility is to use the drift time information from the central electrode. Together with the known distance from the readout chambers to the central electrode the drift velocity can be calculated. This method is appropriate to monitor changes in the drift velocity. For an absolute value the exact offset between the laser trigger and start of the readout has to be known. Together with one of the four layers of laser rays it is also possible to calculate the absolute drift velocity without this knowledge.

Fig. 4.23 shows the drift velocity calculated using the method described last as a function of the date the data were taken. For a comparison the results from the Goofie is also



shown (triangular symbols). Unfortunately no overlap exists. For both data sets the raw (closed symbols) as well as pressure and temperature corrected values (open symbols) are displayed, the latter referring to a pressure of 970 mbar and a temperature of 295 K.

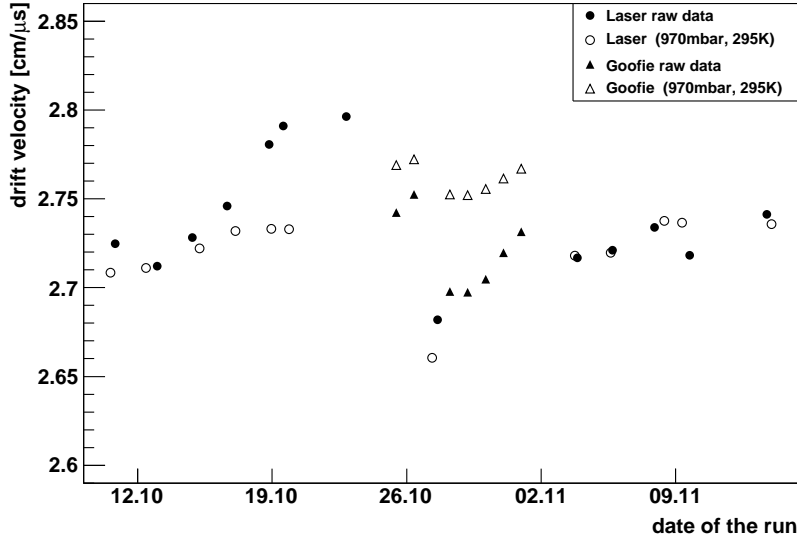


Figure 4.23: Drift velocity as a function of the date

The results from the Goofie and the laser measurements differ by  $\approx 2\%$ . This, however, cannot be understood from the measurement errors, which are well below 1%. It could not be settled conclusively where the difference arises from.

The most probable source of error is the absolute value of the pressure sensor used to correct the laser data. During the commissioning no pressure sensor was available in place. Instead the measurements of a sensor installed at another CERN site was used. The values are available from the internet.

Another potential source of error is the exact knowledge of the micro-mirror positions. The values used are the result of precision measurements after the assembly of the laser system. The quoted precision is  $\approx 150\ \mu\text{m}$ , which results at a drift distance of  $\approx 250\ \text{cm}$  in an error less than 1‰.

One goal for the next laser runs is therefore to have data taken in parallel with both approaches, and to understand in detail the correlations in measurements from the Goofie and the laser system.

#### 4.3.5 Floating Wires

Floating wires have already been introduced above (cf. Sec. 4.3.3.2). They are characterised by pad rows which have a difference in the measured charge to the neighbouring pad rows of more than 10%. Rows with a floating wire are easily identified by eye. An example can be found in Fig. 4.14.

In each of the three wire layers (anode, cathode and gating) floating wires may occur. However, most of the floating wires were identified to be anode wires. By analysing data produced with the calibration pulser and the gating grid pulser system it is possible to distinguish the wire type.

## 4 THE TPC COMMISSIONING IN SXL2

Analysing the signal peaks from calibration pulser events, floating wires in the anode and cathode wire plane can be found. A floating anode wire is identified by a higher signal in the row where the wire is placed above. Since the potential of one wire is missing the signal coupling to the pad in the corresponding row is better, thus resulting in a higher signal. Floating cathode wires in opposite are identified by a lower signal in the pad row. The reason is that one signal inducing wire above the pad row is missing in that case.

Floating gating grid wires could easily be identified by analysing the induced signal of the gating grid pulser. The gating grid pulser switches neighbouring wires to  $\pm 90$  V with an offset voltage of -100 V. The differential switching leads to a fairly good cancellation of the far field. Therefore the signal induced on the pads does not exceed the signal of the calibration pulser which has an amplitude of 7 V. If, however, one wire is not properly connected, the cancellation of the neighbouring signals cannot happen anymore, thus resulting in an increase in the signals measure in the pad row. In the course of this work, however, gating grid signals have not been analysed.

Table 4.5 summarises the pad rows above which floating wires were found in the calibration pulser analysis of the commissioning data. The numbers in brackets denote rows in which the effect is smaller. These rows are always direct neighbours to another affected row. The interpretation is the floating wire is placed at the edge between the two pad rows (cf. Fig. 3.12).

sector	ROC	rows with fl. anode wires	rows with fl. cathode wires
C00	18	24 (23)	
C05	23	32 (31)	
C12	30	47 (48)	
C13	31	29	
C16	34	40 (39)	
A04	40	41 (40), 61, 62	
A05	41	73, 91 (90)	
A07	43	34	
A09	45	37 (38), 63 (64), 93	
A10	46	65 (66)	
A15	51	74, 83	
C00	54		6
C02	56	47 (48)	6
C05	59	37 (38), 48 (47)	
C06	60		91
C07	61	(48)	47
C08	62	13, 14, 15 (12, 17), 60 (59), 65, 66, 86	16
C09	63	73 (72)	
C10	64	47 (48)	
C11	65	62	
C12	66	6, 16	
C14	68	32	
C17	71	81 (82)	

**Table 4.5:** *Floating anode and cathode wires found in the calibration pulser analysis.*

## 5 The TPC Commissioning Underground

In January 2007 the TPC was transported to SX2 to go underground to the experimental area. After the TPC was successfully brought into the parking position<sup>1</sup> the complete electronics was retested to be sure that none of the capton cables, connecting the FECs with the pad plane, went loose during the transport. Following the installation of the ITS the TPC was moved to its final position. All supply and communication systems had to be connected.

The first data that were taken were pedestal and noise measurements. The relevance of these measurements has already been described above.

### 5.1 Noise Measurements

#### 5.1.1 First Noise Measurements at the Final Position

The first noise measurements after the complete C-Side of the TPC had been connected showed that about 24% of the readout pad have a noise larger than 1 ADC channel. In comparison to the measurements in the clean room before the revision of the FEC grounding scheme ( $\sim 10\%$ ). This is an increase of a factor more than two. As can be seen in Fig. 5.1 there are large regions of high noise<sup>2</sup> in the outer part of the OROC. Table 5.1 summarises the maximum, mean and RMS of the noise distributions (Fig. 5.1b) for the different pad sizes. In addition the fraction of pads with noise larger than 1 ADC channel is given.

A major problem with high noise especially at the outer diameter of the TPC is, that the track finding algorithm starts seeding in that region. Neighbouring high noise pads can unintentionally be identified as a cluster. Therefore the seeding algorithm has to loop over many more possibilities, thus slowing down the process. In addition the tails of a real signal get hidden in the noise and deteriorate the position resolution of the cluster.

A second problem is that with the rising number of high noise channels the data volume increases. This in return limits the event rate due to the limited available band width, a situation, which is clearly unfavourable. Therefore the noise level is very problematic and its origin has to be understood and a solution needs to be found.

The short black lines in Fig. 5.1a, which are placed around the outer circumference of the noise data, illustrate at which side of the chamber the bus bar<sup>3</sup> is positioned. A clear correlation of the intensity of the noise with the busbar position is visible.

In contrast to the measurements in the clean room, the intensity of the noise does not depend on the field cage high voltage. The large fraction of high noise channels is already present if the LV power supplies are switched on and the FEE is powered up.

---

<sup>1</sup>A position close to the final one, in which the ITS is accessible and was also installed.

<sup>2</sup>A noise level larger than 1 ADC channel is denoted as “high noise”.

<sup>3</sup>Copper bars mounted along the spokes of the service support wheel (cf. Sec. 3.3.3), which supply the power for the FEE (cf. Fig. 3.16)

These observations in combination with measurements with the power supply used during the commissioning in the clean room (PL508) led to the conclusion, that the new power supplies (PL512) are responsible for this noise situation.

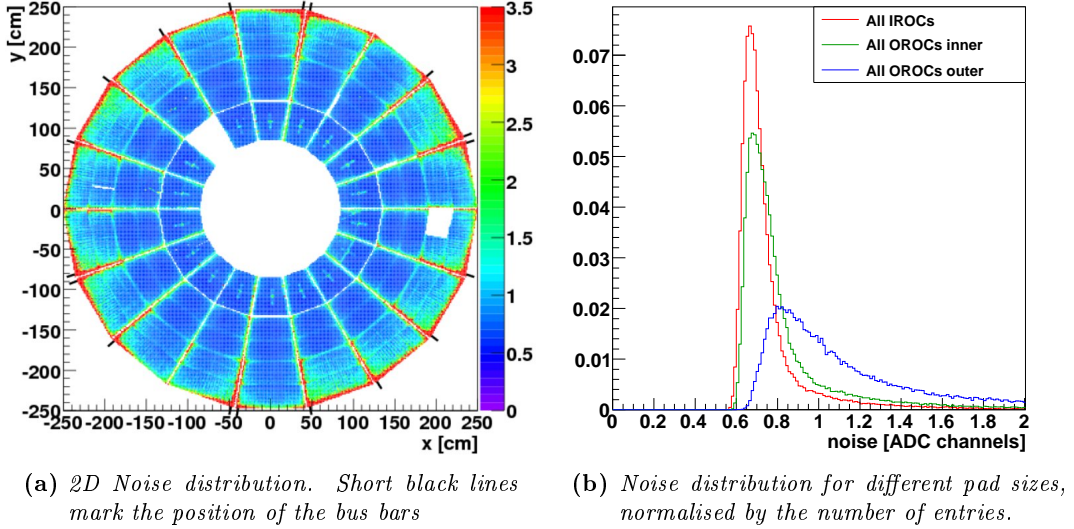


Figure 5.1: Noise distribution of sectors on the C-Side

pad size [mm <sup>2</sup> ]	maximum	mean <sub>0</sub> <sup>2</sup>	RMS <sub>0</sub> <sup>2</sup>	> 1 ADC [%]
4 × 7.5	0.67	0.75	0.18	8
6 × 10	0.68	0.82	0.23	16
6 × 15	0.80	1.08	0.31	57

Table 5.1: Maximum noise and truncated mean and its RMS between 0 and 2 for the different pad sizes. In addition the fraction of channels above 1 ADC channel (high noise) is given.

### 5.1.2 Measurement of the Common Mode Current

The LV power supplies (PS) provide a floating direct current. Therefore the power source is decoupled from the common grounding potential. The decoupling is done by means of capacitors (Y Caps, see Fig. 5.2). Up to 50 m long cables are laid from the racks in which the PS are mounted to patch panels close to the FEE. To be independent of the voltage drop along these cables, the voltage which is measured at the FEE is fed back to the PS by *sense lines* (see Fig. 5.2). The PS can then regulate the voltage accordingly.

The common-mode current is measured by means of a coil, which is surrounding both LV cables at the output of the PS (see sketch). The result of the measurement is display in Fig. 5.3. It shows the measured common-mode current as a function of the frequency. At 300 kHz a stron peak is visible, which shows, that a common-mode current of about 85 dBuA<sup>4</sup> (18 mA) is induce by the low voltage power supplies.

The company which produces the PS suggested to exchange the standard Y Caps (10 nF,

<sup>4</sup>A logarithmic (dB) scale of the current in  $\mu\text{A}$ .  $1 \mu\text{A} = 10^{\text{dBuA}/20}$

500 V) by  $1\ \mu\text{F}$ , 50 V SMD capacitors and in addition use ferrite toroids to damp the common-mode current.

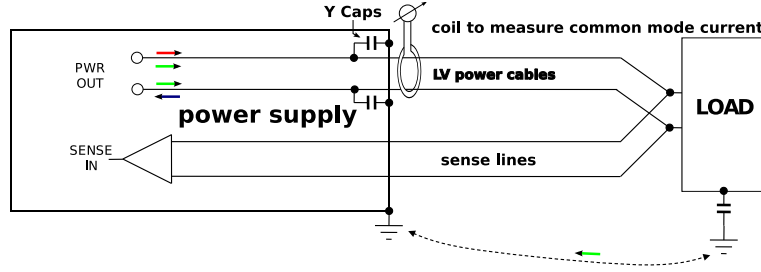


Figure 5.2: Sketch of one channel of the LV power supply to illustrate the common-mode current.

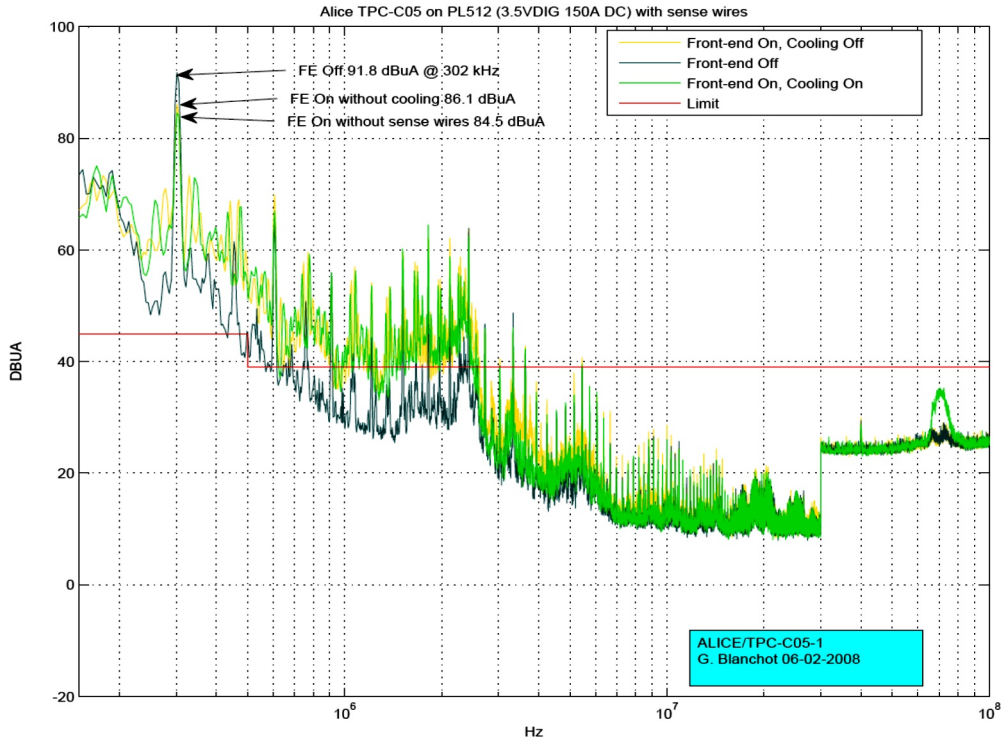


Figure 5.3: Common-mode current at the output of the LV power supply. Taken from [35].

### 5.1.3 Noise Measurements with Ferrite Toroids

Following the suggestions from the company different combinations with two toroids<sup>5</sup> have been investigated. To measure the noise behaviour one PS was modified and tested in one sector (C05). In Fig. 5.4 a sketch of one channel of the PS and the different positions of the toroids is displayed.

<sup>5</sup>1. Small toroid: Steward 28B1000-000 ( $Z=3@0.5\ \text{MHz}$ ,  $Z=109@100\ \text{MHz}$ )  
 2. Large toroid: Steward FB259128-000 ( $Z=51@0.5\ \text{MHz}$ ,  $106@1\ \text{MHz}$ ,  $62@5\ \text{MHz}$ )

Fig. 5.5 summarises the results in terms of the mean and RMS of the noise distributions for the different pad sizes, calculated in a window of 0-5 ADC channels. The abbreviations of the configurations stand for:

S: Small; L: Large; N: No; I: Internal; E: External and the T means toroid. Thus the combination ‘SLIT - NET’ denotes a configuration with Small and Large Internal Toroids and No External Toroids.

In comparison with the unmodified PS (unmod.) all modifications show an enormous improvement. The mean of the distributions after the modifications went down by a few (IROC) to up to 40 % (outer OROC) and the RMS decreased by factors up to about 8. The best results are obtained with a combination of small and large internal toroids. Combining this configuration with a large external toroid makes nearly no difference with respect to no external toroid. In Fig. 5.6a the noise ratio of ‘SLIT-NET’ over ‘SLIT-LET’ is displayed, combined for the IROC (row<63) and OROC (row>=63). Smaller changes (<5 %) are only seen for a few pads along the long edge of the OROC.

For the combination ‘SLIT - LET’ an additional measurement with the field cage high voltage set to 10 kV was carried out. Fig. 5.6b shows the noise ratio ‘SLIT-LET; FC HV: 10kV’ over ‘SLIT-LET’. Only a few pads in the center of the IROC, along the long edge of the OROC and in the top left corner of the OROC show changes larger than 5 %. Compared to the measurements in the clean room (cf. Sec. 4.3.2.4), where a major part of the pads showed an increase in the noise of 20 % up to a factor 2, this is only a small effect.

The results of the noise measurements presented were used as a basis for the decision of the final configuration of the PL512 power supplies. It was decided to use the

- small and large internal toroids,
- no external toroids and
- 1  $\mu$ F, 50 V SMD Y-Caps.

The large external toroids have not been installed since no obvious improvement is seen and it would include to modify all the bins which keep the PS. This would have been a delicate procedure, including a mayor delay.

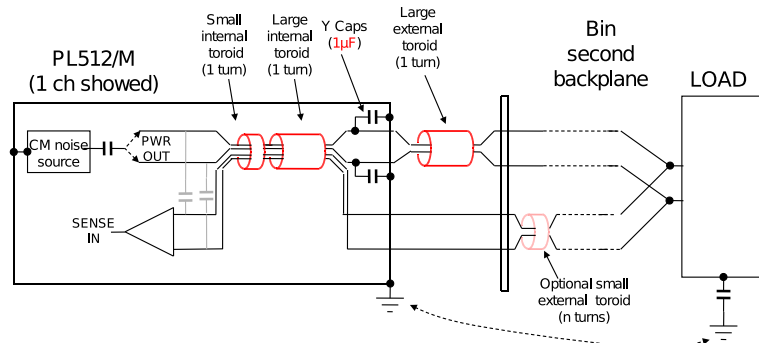


Figure 5.4: Sketch of one channel of the LV power supply with ferrite toroids. Taken from [35].

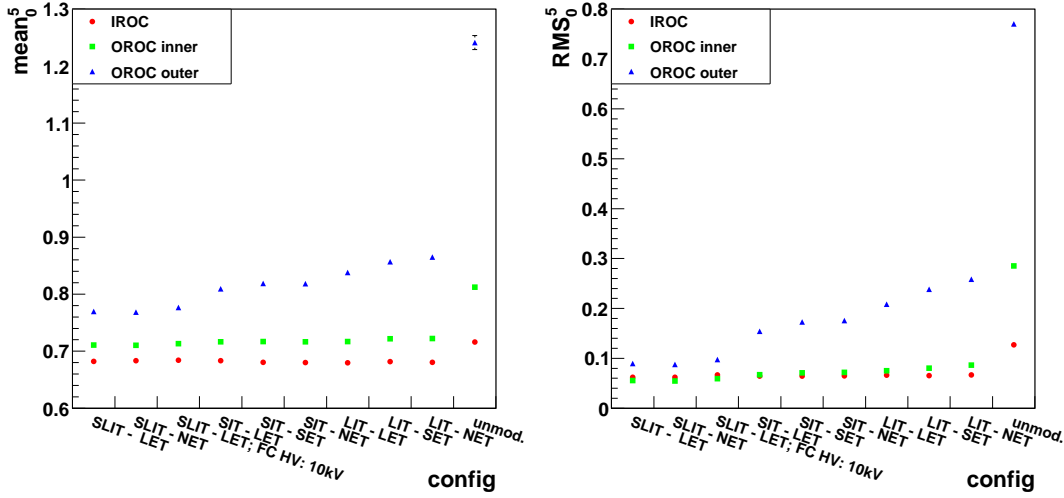


Figure 5.5: Mean and RMS of noise distributions for different configurations with ferrite toroids. S=Small, L=Large, N=No, I=Internal, E=External, T=Toroid. For details see text.

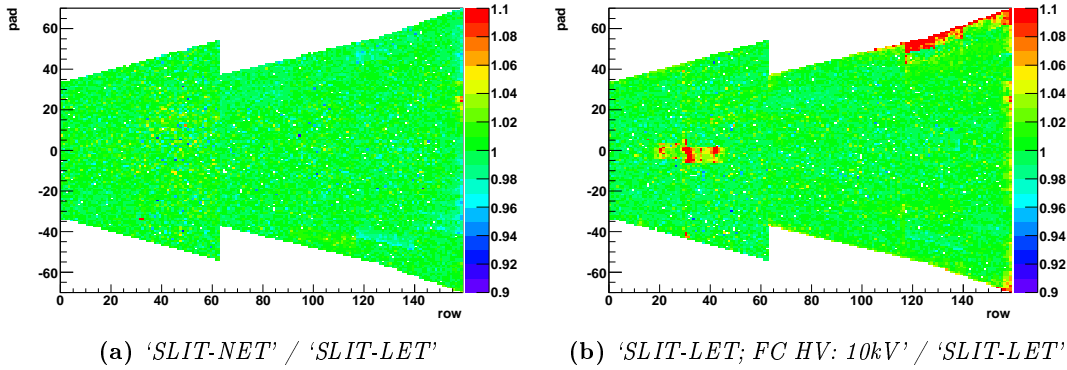


Figure 5.6: 2D noise ratio of different toroid configurations in sector C05.

### 5.1.4 Noise with the Final Configuration of the LV Power Supplies

Middle of May the first measurements with all power supplies modified as describe above and nearly all FEE in operation were carried out. Only four out of the 121 readout partitions a few additional FECs still showed problems in the readout. In the following the final noise situation of TPC is described.

After the modification of the power supplies only 1.4% of the channels show a noise larger than 1 ADC count. Compared with the clean room situation before the modified grounding scheme of the FECs (~10%) and the first measurements in the final position (~24%) this is a major success. Due to the noise increasing with the PCB track length, for the outer part of the OROC a 10% higher noise (1.1 ADC channels) should be tolerated (cf. Sec. 5.1.4.1). Allowing for this, the fraction of “high noise” pads is only 1%.

The noise distributions of the different pad sizes are displayed in Fig. 5.7. Maximum, mean and RMS values of the distributions are summarised in table 5.2. In addition the

fraction of pads above 1 ADC channel is given. For the largest pads the fraction above 1.1 ADC channels is given in brackets.

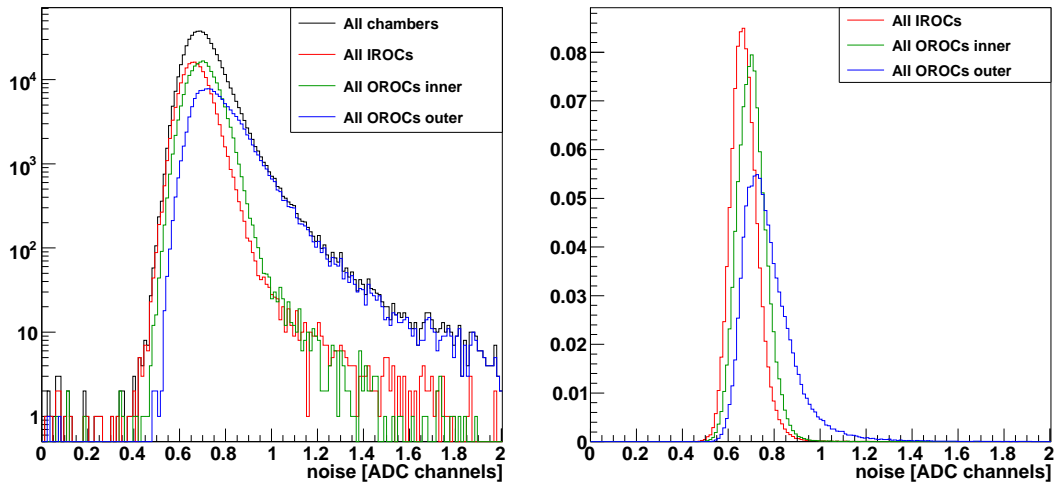
For the small and middle sized pads, only a negligible number of “high noise” pads is observed (0.3 and 0.2 %, respectively). The largest contribution comes from the largest pads (3.2 %), where the “high noise” pads are limited to a few regions mainly in the outer corners and along the long edge. A 2D representation of the noise distribution of the A- and C-Side, as well as for a single chamber is displayed in Fig. 5.8.

Conspicuous is one region of higher noise on each side. It was found that between sectors A14, A15 and C02, C03, respectively. This is in contrast to the first measurements underground (cf. Fig. 5.1) not correlated to the position of adjacent bus bars. Between sectors A14 and A15 the drift HV is connected, while between C02 and C04 one of the resistor rods is located (cf. Fig. 3.17). Such a behaviour is, however, not seen for the other resistor rods, which are between sectors A02/A03, A10/A11 and C10/C11.

It is planned to study whether the noise level can still be improved by introducing a filter in the drift voltage power supply.

pad size [mm <sup>2</sup> ]	maximum	mean <sub>0</sub> <sup>2</sup>	RMS <sub>0</sub> <sup>2</sup>	> 1 ADC [%]
4 × 7.5	0.66	0.67	0.066	0.3
6 × 10	0.70	0.70	0.066	0.2
6 × 15	0.73	0.78	0.118	4.9 (3.2)

**Table 5.2:** Maximum noise and truncated mean and its RMS between 0 and 2 for the different pad sizes. In addition the fraction of channels above 1 ADC channel “high noise” is given. For the largest pads with the longest PCB tracks a larger high noise (1.1 ADC channels) value should be accepted. The resulting fraction is given in brackets. For details see text.



(a) Noise distribution for all chambers and split for the different pad sizes (log scale!).

(b) Noise distribution for different pad sizes, normalised by the number of entries.

**Figure 5.7:** Noise distribution of all sectors



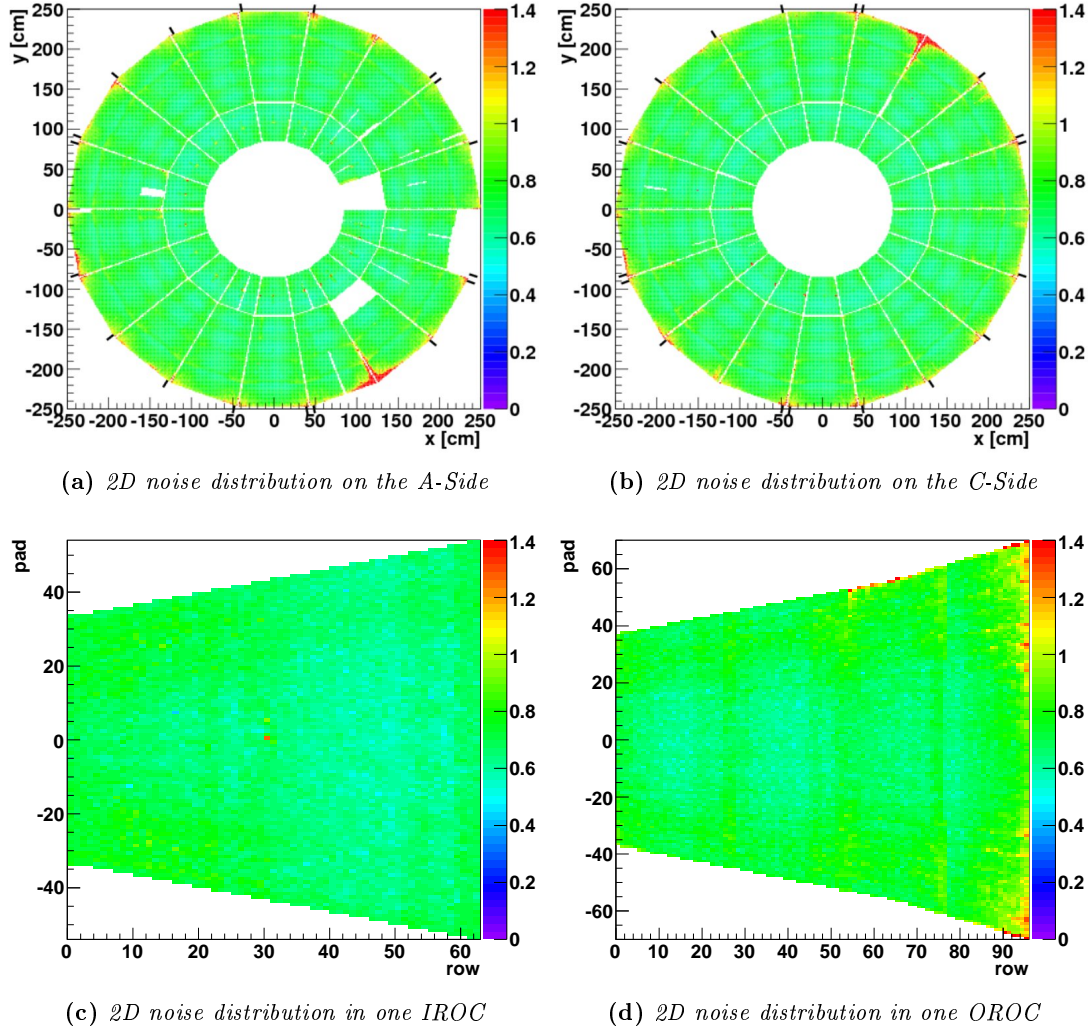


Figure 5.8: 2D noise distribution in the TPC

#### 5.1.4.1 Noise Dependence on the PCB Track Length (Final Configuration)

For completeness the dependence of the noise on the PCB track length is shown for the final configuration. In Fig. 5.9 this dependence is shown separately for the different pad sizes. A line was fit to each distribution with a robust option (70%), as described in Sec. 4.3.2.3. The fit parameters are summarised in table 5.3. Fig. 5.9d shows the distributions of the residuals wrt the line fits. To each distribution a gaussian function was fit in an interval of  $\pm 0.1$  around the peak. The width ( $\sigma$ ) of the distributions are also summarised in tab. 5.3. The linear increase of the noise with the increasing track length and the width around the linear dependence can be thought of the intrinsic noise of the system. One can then ask for the maximum intrinsic noise  $n_{max}$  for each pad size. It was calculated for each pad size in the following way:

$$n_{max} = p_0 + p_1 * l_{max} + 3\sigma,$$

where  $p_0$  and  $p_1$  are the fit parameters (intersection and slope),  $l_{max}$  is the maximum track length and  $\sigma$  as described above.  $l_{max}$  are about 120, 120 and 150 mm, respectively, for the different pad sizes in increasing order.

For the small and middle sized pads the max. noise is about 1 ADC channel, which is exactly the goal to get a SNR of 30:1. For the largest pads the intrinsic noise rises above this value for track lengths  $l \gtrsim 115$  mm and reaches 1.1 ADC channels for the longest tracks (150 mm).

Fig. 5.10 shows the 2D distribution of pads not following the linear behaviour in terms of a  $3\sigma$  band around the line fits for the A- (a) and C-Side (b). Pads (c) and (d) of the same figure illustrate in how many sectors a pad in the IROC and OROC, respectively, did not follow the linear trend. In a majority of the IROCs ( $>60\%$ ) a few pads in the centre of the chambers as well as on one side<sup>6</sup> dont follow this trend. In the OROC mainly pads in the corners and along the long edge are affected.

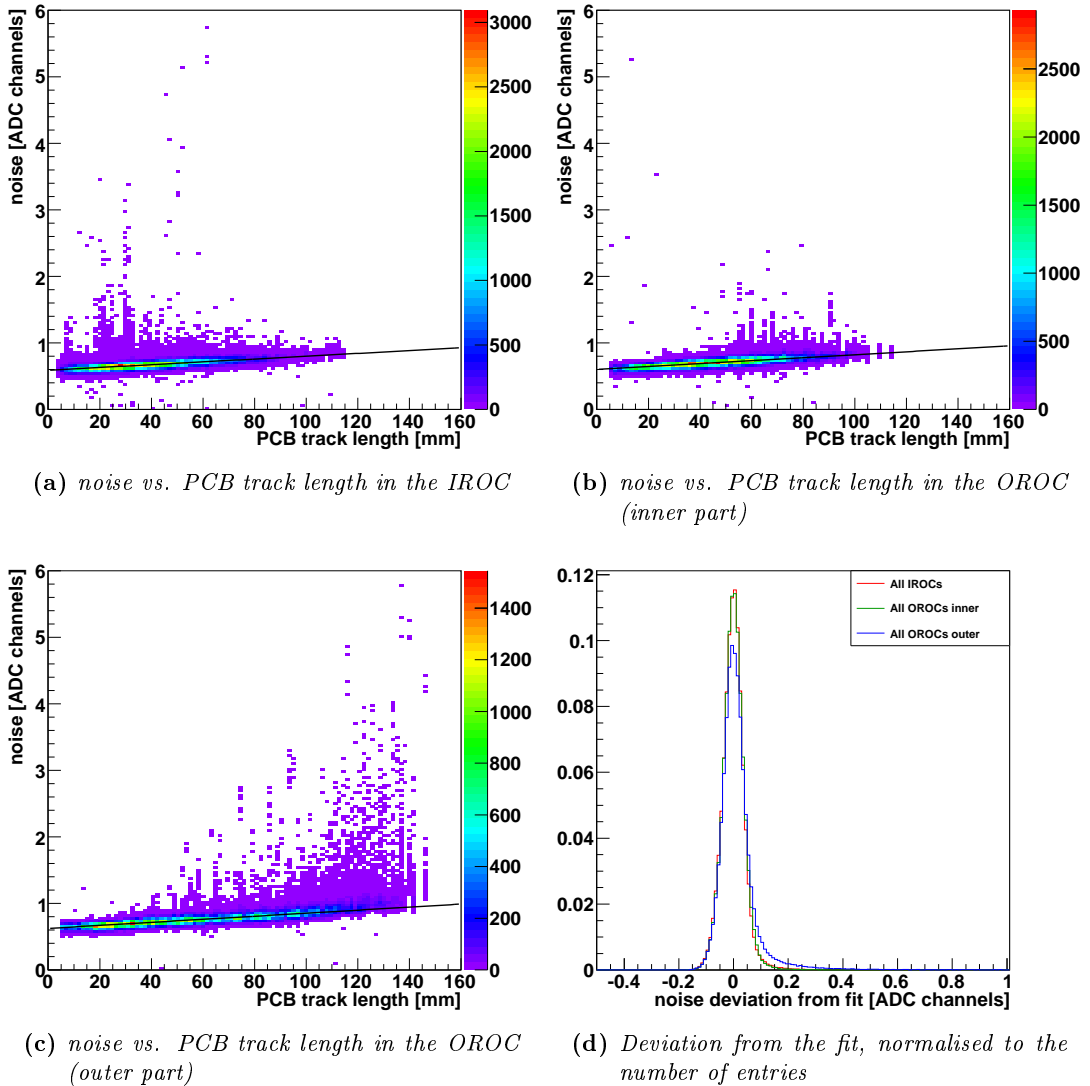


**Figure 5.9:** Correlation of noise and PCB track length. The black lines show a line fit with robust option.

<sup>6</sup>For technical reasons the capton cables used to connect the two FECs along this edge with the pad plane are longer.

pad size [mm <sup>2</sup> ]	ordinate intersection	slope	sigma	max. noise allowed
$4 \times 7.5$	$5.89 \cdot 10^{-01}$	$2.12 \cdot 10^{-03}$	$3.56 \cdot 10^{-02}$	1.0
$6 \times 10$	$6.03 \cdot 10^{-01}$	$2.20 \cdot 10^{-03}$	$3.61 \cdot 10^{-02}$	1.0
$6 \times 15$	$6.24 \cdot 10^{-01}$	$2.29 \cdot 10^{-03}$	$3.99 \cdot 10^{-02}$	1.1

**Table 5.3:** Fit parameters of the line fits in Fig. 5.9, sigma of the distributions in Fig. 5.9d and the resulting max. allowed noise ( $3\sigma$  above line fits) for the different pad sizes

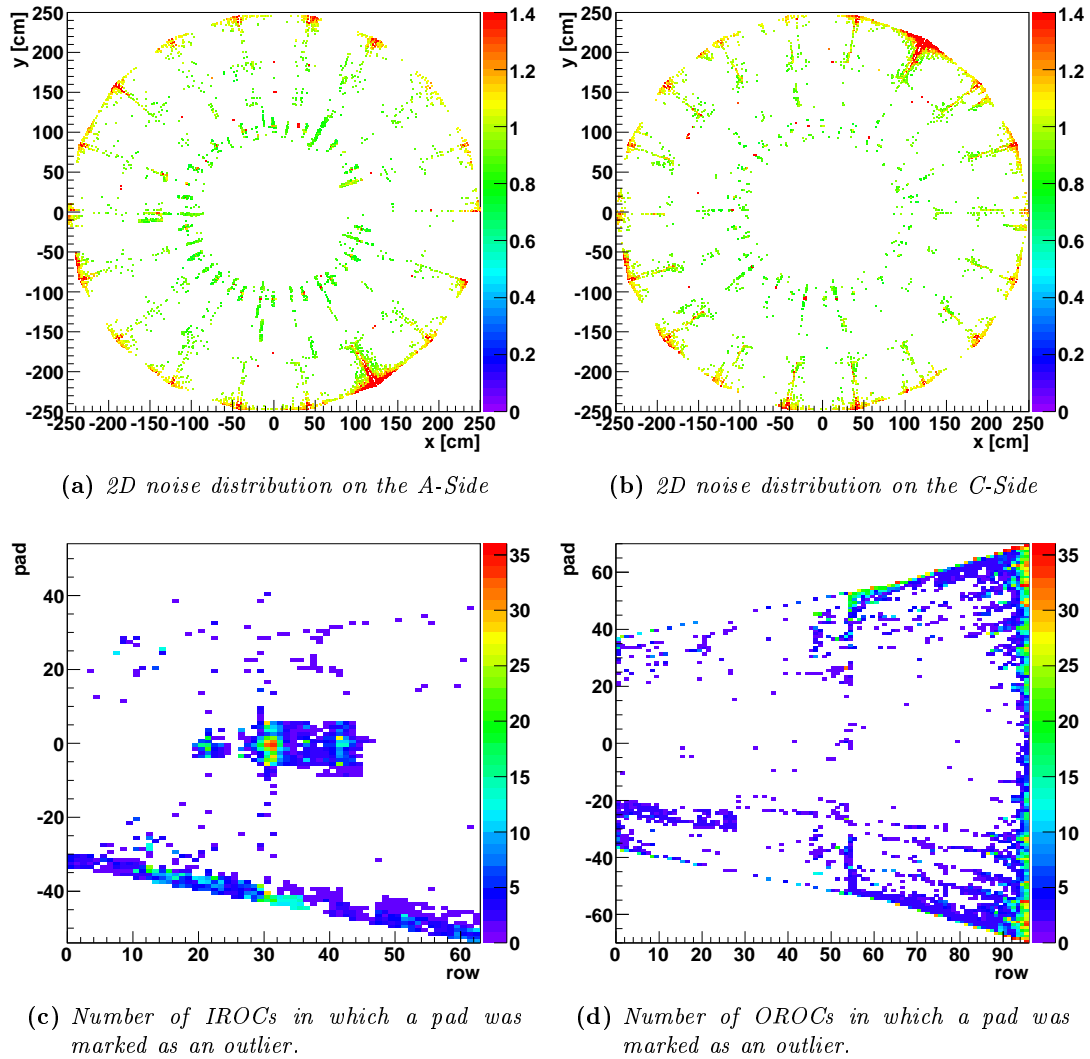


**Figure 5.10:** 2D noise distribution in the TPC. Shown are only those pads in which the noise is more than  $3\sigma$  away from the line fit shown in Fig. 5.9



## 6 Summary and Outlook

In the present work results of the commissioning data of the Time Projection Chamber of the ALICE detector system have been presented. The analysis comprised the evaluation of pedestal and noise data, as well as signals from the calibration pulser and photo electrons emitted by the central electrode.

The noise data of the first measurements revealed that a large fraction of the readout channels (10 %) show noise values larger than 1 ADC count (“high noise”), which is the limit to maintain the aimed signal to noise ratio of 30:1. The high noise is limited two common regions in all chambers. The largest fraction of high noise pads is observed in the largest pads. By minimising the ground bounce effect, which occurs due the CMOS technology used in the Front-End Electronics (FEE), the noise could be reduce to a reasonable level. The ground bounce could be reduced by desynchronisation of the readout of the FEE and a revision of the its grounding scheme.

It was shown that the noise level increases with the size of the readout pads and also the length of pcb track. Both effects result from the fact that the noise of charge sensitive amplifiers (as used in the TPC FEE) increases linearly with the input capacitance.

In the calibration-pulsar signal analysis, chip by chip variations in the arrival time and signal integral (gain) have been determined. The influence of the diffusion of the drift electrons on the cluster position resolution is, however, dominant over the influence of the chip by chip variations. The resolution of the tracking, is not influenced by the chip variations since the clusters associated to a track are effected randomly. To achieve the intrinsic  $dE/dx$  resolution the gain variations should be taken into account.

Signals from the central electrode, can be used to study a global missalignment and/or field distortions. In addition drift velocity gradients as well as its variation in time can be monitored. The analysed data show a vertical gradient in the drift velocity, which can be explained by the observed temperature gradient in the TPC. In addition a radial dependence of electron arrival times was observed. Possible explanations are a relative conical deformation of the readout plane and the central electrode or a global distortion of the electric field due to not yet properly tuned voltages on the gating grid and the cover and skirt electrodes. The ... photogrammetric measurements of the redout chamber positions in the endplate render field distortions much more probable than a mechanical misalignment.

Results of drift velocity measurements were presented and compared with measurements obtained with a dedicated drift velocity monitor. Unfortunately no overlap in the data taking periods existed. Nevertheless, the trends of the measurements show a deviation of about 2 % between both approaches. However, the origin of the difference could not have been clarified.

In the measured charge information of the calibration pulser analysis as well as the central electrode analysis individual pad row were observed showing a gain that differs by more than 10 % compared to the neighbouring pad rows. This !auffaligkeit! was explained by a floating anode or cathode wire.

First noise measurements with the TPC in its final position and connected to the final

infrastructure, showed that 24% of the pads have noise values larger 1 ADC count. The noise was strongly correlated to the position of the bus bars which supply the voltage for the FEE. The induced noise was traced back to be caused by a common mode current at about 300 kHz. The current was injected into the system by the low voltage power supplies of the FEE. Results of a systematic study with different configurations of ferrite toroids was presented. With the final configuration the fraction of high noise pads could be reduced to 1.4%.

For the analysis of the pedestal and noise data as well as the analysis of signals generated with the calibration pulser and signals from the central electrode, calibration algorithms have been developed, which are part of the official analysis framework of the ALICE detector - AliRoot.

To clarify the origin of the difference in the drift velocity measurements obtained by the drift velocity monitor and from the laser data analysis, an overlapping period of data taking is needed.

To understand if the observed radial dependence of the arrival time of the drift electrons is caused by field distortions or a mechanical misalignment a systematic study with different voltage settings on the gating grid and the cover and skirt electrodes has to be carried out. The information from the central electrode will be complemented by the analysis of the laser tracks.

A detailed study of the relative alignment of the readout chambers needs to be carried out. The information obtained from the central electrode analysis will be combined with the analysis of laser tracks as well as cosmic tracks. These studies will be further improved by the measurements of the first collisions.

# A Description of the calibration classes

In this chapter the working principles of the three calibration classes “AliTPCCalibPedestal”, “AliTPCCalibPulser” and “AliTPCCalibCE” will be explained in detail. After an introduction about the commonalities of the classes (interface, work flow), each algorithm will be described on its own.

## A.1 Common introduction

The general idea of the calibration classes is to process and analyse raw data. The algorithms are supposed to run in different environments, such as in the offline reconstruction, the high level trigger or in the data acquisition system. To guarantee flexibility in the data processing, several methods are available calling each other in a hierarchical order. For the decoding of the raw data two different algorithms are available which led to two branches of processing functions. The relevant functions are called **ProcessEvent[Fast]** taking as an input either the DATE **eventHeaderStruct** an **AliRawReader** object or an **AliTPCRawStream[Fast]** object. The function which does the actual processing of the data is called **Update** and takes as arguments the sector, pad row, pad, time bin and ADC signal. All this is summarised in fig. A.1.

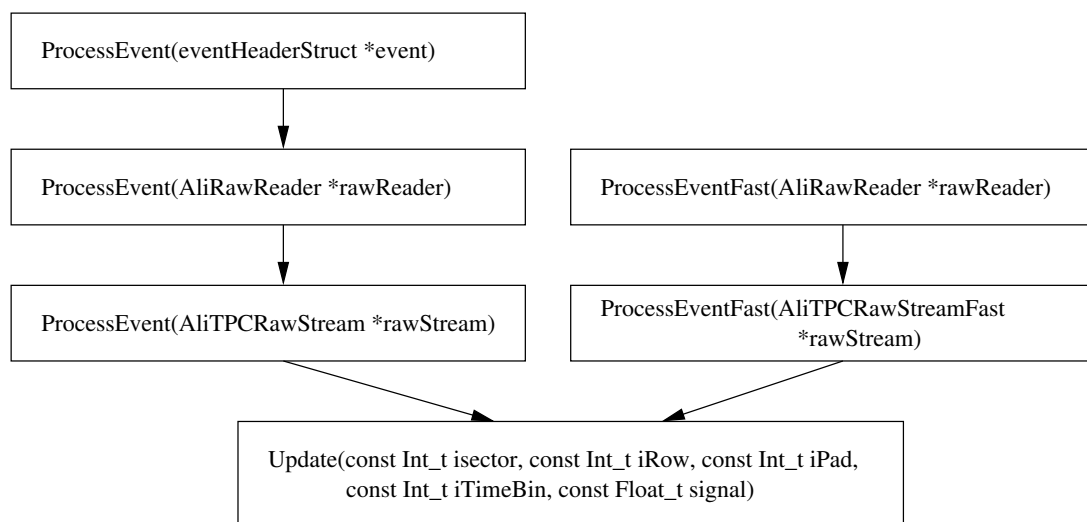


**Figure A.1:** *Hierarchy of the event processing functions of the calibration algorithms.*

The calibration data is stored in *reference histograms*, filled in the **Update** function, functions called inside, and the **EndEvent** function. For each readout chamber and calibration variable *XXX* one reference histogram is created. These are two dimensional having on the y-axis the channel number within the ROC and on the x-axis the distribution of the calibration variable. Setters exist to adjust the range and number of bins. An example of a reference histogram can be found in fig. A.2.

## A DESCRIPTION OF THE CALIBRATION CLASSES

Inside the calibration class the reference histograms are stored in *TObjArrays*. For each variable one array exists which keeps 72 histograms, one for each ROC. The arrays are called **fHistoXXXArray**. The reference histograms can be retrieved by calling the according getter function **GetHistoXXX**(Int\_t sector, Bool\_t force=kFALSE). To allocate memory only if needed, the histograms are created the first time the getter is called and the force flag is set to kTRUE.

For the Pulser and CE calibration after each event the **EndEvent** function has to be called, doing some post processing, the filling of a part of the reference histograms and calculation of data stored event by event (see description below).

After the desired statistics has been accumulated the actual calibration values pad by pad are calculated by calling the **Analyse** function. To store the data a special class **AliTPCCalROC** is used keeping all values for one readout chamber. As in case of the reference histograms, the **AliTPCCalROC** objects are only created upon request, by using the getter function **GetCalRocXXX**(Int\_t sector, Bool\_t force=kFALSE) with the force flag set to kTRUE. The objects are also stored in *TObjArrays* which are called **fCalRocArrayXXX**. A pointer to the complete arrays is provided by the **GetCalPadXXX**() functions.

To save the calibration data the function **DumpToFile** is available, taking as arguments the filename and optional a directory name to which it should be stored in the file and if the file should be updated instead of overwritten.

The process flow described above is summarised in fig. A.3.

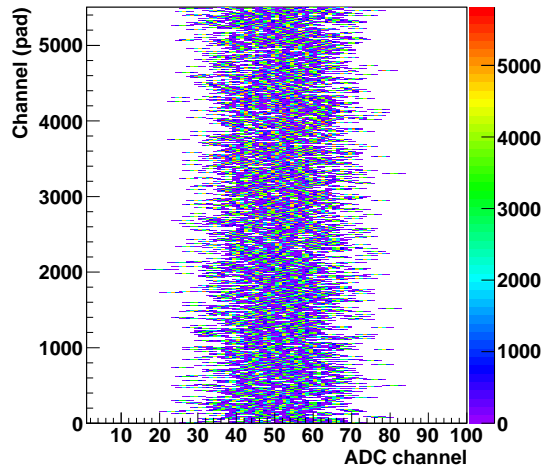


**Figure A.2:** Example of a reference histogram. Displayed are the electronic baseline distributions for all pads of one IROC.

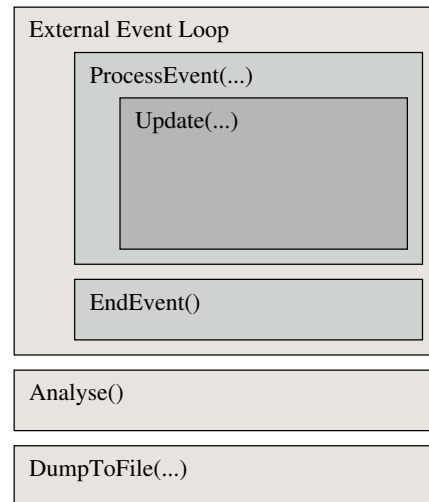


**Figure A.3:** Process flow of the calibration algorithms.

## A.2 Pedestal calibration class

### A.2.1 Signal filling [Update(...)]

The **Update** function fills the reference histograms with the ADC values of all time bins in the selected range (`fFirstTimeBin`, `fLastTimeBin`) with standard values (60, 1000). The



range can be specified by the setter function **SetRangeTime**(Int\_t tMin, Int\_t tMax). If requested by **SetTimeAnalysis**(Bool\_t time = kTRUE), pedestal values for each time bin will be calculated. This information can be used to fill the pattern memory of the ALTRO in order to perform a timebin by timebin baseline subsection.

### A.2.2 Calibration value calculation [Analyse()]

Calling the **Analyse**() routine calculates the pedestal and noise values for each channel by fitting a gauss function on the distribution. In addition a second approach is used calculating the mean and corresponding RMS. If desired a truncation range can be set using the **SetAnalysisTruncationRange**(Float\_t down, Float\_t up) function, where down and up mark the range as a fraction of the data: e.g. (0.05,0.9) would exclude the lower 5% and upper 10%.

### A.2.3 Stored calibration values

The available calibration values calculated in the pedestal calibration class, a description as well as the corresponding getter functions are summarised in table A.1

Calib. val.	description	getter (AliTPCCalROC*)	getter (TObjArray*)
Pedestal	pedestal value (mean of a gauss fit)	GetCalRocPedestal(sector)	GetCalPadPedestal()
Sigma	noise value (sigma of a gauss fit)	GetCalRocSigma(sector)	GetCalPadSigma()
Mean	pedestal value (mean of the distribution)	GetCalRocMean(sector)	GetCalPadMean()
RMS	noise value (RMS of the distribution)	GetCalRocRMS(sector)	GetCalPadRMS()

*Table A.1: Calibration values in the pedestal calibration class.*

## A.3 Pulser calibration class

### A.3.1 Signal filling [Update(...)]

In the **Update**(...) function an array (fPadSignal) is filled with the ADC signal information for each timebin of the currently processed channel (pad). In addition the maximum ADC value and corresponding timebin is stored (fMaxPadSignal, fMaxTimeBin). Only the selected time range (fFirstTimeBin, fLastTimeBin) is taken into account. The range can be set by calling **SetRangeTime**(Int\_t firstTimeBin, Int\_t lastTimeBin). Before proceeding with the next channel, the **ProcessPad**() function is called, which analyses the information currently stored in fPadSignal.

### A.3.2 Channel information processing [ProcessPad()]

As a first step the pedestal and noise values for the current pad are queried (**FindPedestal**()). Therefore either previously measured data can be used (**SetPedestalDatabase**(AliTPCCalPad \*pedestalTPC, AliTPCCalPad \*padNoiseTPC)) or if not set the pedestal and noise will be calculated. This is done by calculating the truncated mean

---

## A DESCRIPTION OF THE CALIBRATION CLASSES

---

and RMS within a range of  $\pm 10$  ADC channels around the median of the signal distribution stored in `fPadSignal`.

In the second step the properties of the pulser signal are calculated (**FindPulserSignal(...)**). For the analysis it is assumed that there is only one signal which spreads over a range of minus two to plus seven timebins around `fMaxTimeBin`. After the pedestal subtraction the signal sum, mean and RMS are calculated in this range. If the signal sum is below a threshold of 8 times the pad noise (minimum noise set to 1 ADC count), all values are set to zero.

As a third step the reference histograms for the charge (signal sum) and signal width information are filled. The time position (signal mean) is stored in an array for later processing (see below).

### A.3.3 Event information processing [**EndEvent()**]

The **EndEvent()** function loops over all readout chambers and fills the time information into the reference histograms. Stored is the deviation from the mean of the time signals in the currently processed ROC.

### A.3.4 Calibration value calculation [**Analyse()**]

In the **Analyse()** function the final calibration values are calculated as the mean of the distributions stored in the reference histograms. The information is finally stored in `AliTPCCalROC` objects.

### A.3.5 Stored calibration values

The available calibration values calculated in the pulser calibration class, a description as well as the corresponding getter functions are summarised in table A.2

Calib. val.	description	getter (AliTPCCalROC*)	getter (TObjArray*)
T0	time position (relative to the chamber mean)	GetCalRocT0(sector)	GetCalPadT0()
Q	signal sum	GetCalRocQ(sector)	GetCalPadQ()
RMS	signal width	GetCalRocRMS(sector)	GetCalPadRMS()

Table A.2: Calibration values in the pulser calibration class.

## A.4 Central electrode signal calibration class

### A.4.1 Signal filling [**Update(...)**]

Before calling one of the **ProcessEvent(...)** functions or the **Update(...)** function, **SetEventInfo**(Double\_t runNumber, Double\_t timestamp, Double\_t eventId) should be called for each event to be able to display the stored calibration values as one a function of on of these information. The **Update(...)** function itself is exactly the same as described above in the Calibration Pulser section (A.3.1).

### A.4.2 Channel information processing [ProcessPad()]

The first step is getting the pedestal and noise values (see A.3.1).

In the second step local maxima are searched in the pad signal by calling the function **FindLocalMaxima**(...). For each chamber a histogram is filled with this information. To be accepted as a local maximum the signal has to be five times larger than the pad noise and needs 2(3) preceding (succeeding) timebins with a falling signal height. Maxima are expected to arise from the laser rays, photoelectrons from the central electrode, but also periodic post peaks following the CE signal have been observed. The largest fraction however arising from the CE. In the **EndEvent**() function for each ROC the time position of the maximum of the local maxima distribution will be calculated, identified with the time position of the central electrode and stored event by event in an array (*fTMeanArrayEvent*).

If no event has been processed yet in this run no further processing on the pad signal will be done. The reason is that no position information of the central electrode signal is available at that point.

The third step is the analysis of the central electrode signal (**FindCESignal**(...)). To decide which of the local maxima found before represents the CE signal, the distance to the identified position of the previous event (see end of second step) is calculated. The maximum with the smallest distance is used. Signal sum, mean and RMS are calculated in a range of -4 to +7 timebins around the maximum. If the signal sum is smaller than eight times the pad noise, all values will be set to zero.

The fourth step filling of the signal sum and width histograms, as well as filling a temporary array with the time (signal mean) information.

### A.4.3 Event information processing [EndEvent()]

In the beginning of the function the mean drift time for each readout side is calculated.

Next it is looped over all sectors for which information are available. If the local maxima distribution histogram has less entries than 2/3 of the number of channels of the ROC, it will be skipped. This is the reason if the calibration algorithm is run on data which has no laser events.

As already described above the maximum position of the local maxima distribution is calculated. For this purpose the truncated mean within a range of  $\pm 4$  timebins around the median of the distribution is used.

To monitor the stability of the laser, the mean charge (signal sum) is calculated for each ROC and stored event by event.

In a loop over all channels the time reference histograms are filled with the difference of the pad time signal to the mean arrival time of the corresponding readout side, calculated above. This approach is used to accumulate statistics over a long time range in which the drift velocity might change. Non time dependend and time dependend effects are such hoped to be decoupled to a large extent. In addition a temporary AliTPCCalROC object is filled with the time information.

The AliTPCCalROC object is used to perform a linear as well as parabolic 2D fit to the data. This information is stored event by event and can be used to study non uniform changes in the drift velocity.

## A DESCRIPTION OF THE CALIBRATION CLASSES

### A.4.4 Calibration value calculation [Analyse()]

In the **Analyse()** function the final calibration values are calculated as the mean of the distributions stored in the reference histograms. The information is finally stored in AliTPCCaROc objects.

### A.4.5 Stored calibration values

The available calibration values calculated in the pulser calibration class, a description as well as the corresponding getter functions are summarised in table A.3

Calib. val.	description	getter (AliTPCCaROc*)	getter (TObjArray*)
T0	time position (relative to the readout side)	GetCalRocT0(sector)	GetCalPadT0()
Q	signal sum	GetCalRocQ(sector)	GetCalPadQ()
RMS	signal width	GetCalRocRMS(sector)	GetCalPadRMS()

**Table A.3:** Calibration values in the central electrode calibration class.

As described above additional data is stored event by event for each chamber. Table A.4 summarises the information, gives a short description and shows the getter function.

type of information	getter	description
results of a plane fit	GetParamArrayPol1(sector)	returns a TObjArray of TVectorD objects, one entry per event
results of 2D parabolic fit	GetParamArrayPol2(sector)	returns a TObjArray of TVectorD objects, one entry per event
mean arrival time	GetTMeanEvents(sector)	returns an array of floats (TVectorF), one entry per event
mean signal sum	GetQMeanEvents(sector)	returns an array of floats (TVectorF), one entry per event

**Table A.4:** Event by event information stored for each chamber in the central electrode calibration class.

## A.5 Using the Calibration Classes

Listing A.1 shows an example how to loop over one root raw data file and process the data with one of the calibration classes.

The code shows a ROOT macro that is supposed to be executed from the commandline prompt in the ALICE offline analysis framework AliRoot. In the example *XXX* has to be replaced by one of *Pedestal*, *Pulser* or *CE*.

Examples of how to load the macro and execute it is shown in listing A.2 for the case of a pedestal run and A.3 in case of a pulser or laser run. The listings also demonstrate the possibility of displaying the stored calibration data using the AliTPCCalPad class. For more information see the documentation in the class code.

```

1 AliTPCCalibXXX* fillCalibObject( const Char_t *filename ){
    AliTPCCalibXXX *calibObject = new AliTPCCalibXXX;
    AliRawReader *rawReader = new AliRawReaderRoot(filename);
    if ( !rawReader ) return 0x0;
    rawReader->RewindEvents();
6   while (rawReader->NextEvent()) //event loop
        events = calibObject->ProcessEvent(rawReader);
    calibObject->Analyse(); //Analyse accumulated data
    calibObject->DumpToFile("CalibXXXDataFile.root"); //Save data
    return calibObject;
11 }

```

Listing A.1: *fillCalibObject.C*

```

root [1] .L fillCalibObject.C
root [2] AliTPCCalibPedestal *c=fillCalibObject("path/to/file.root")
root [3] Int_t i;
root [4] for (i=0;i<72;i++) if (c->GetHistoPedestal(i)) cout<<i<<endl;
root [5] //assume sector 0 is filled, show its RMS reference histogram
root [6] c->GetHistoPedestal(0)->SetEntries(1)
root [7] c->GetHistoPedestal(0)->Draw("colz")
root [8] //Unsing the AliTPCCalPad class
root [9] AliTPCCalPad pedestal(c->GetCalPadPedestal())
root [10] pedestal->MakeHisto2D()->Draw("colz"); //A-Side pedestals
root [11] pedestal->MakeHisto2D(1)->Draw("colz"); //C-Side pedestals
root [12] AliTPCCalPad noise(c->GetCalPadRMS())
root [13] noise->MakeHisto2D()->Draw("colz"); //A-Side noise
root [14] noise->MakeHisto2D(1)->Draw("colz"); //C-Side noise
root [15] //display single chamber (0)
root [16] pedestal->GetCalROC(0)->MakeHisto2D()->Draw("colz")

```

Listing A.2: *commandsPedestal.cint*

```

root [1] .L fillCalibObject.C
root [2] AliTPCCalibPulser *calib=fillCalibObject("path/to/file.root")
root [3] //or
root [4] AliTPCCalibCE *calib=fillCalibObject("path/to/file.root")
root [5] Int_t i
root [6] for (i=0;i<72;i++) if (calib->GetHistoT0(i)) cout << i<<endl;
root [7] //assume sector 0 is filled, show its RMS reference histogram
root [8] calib->GetHistoT0(0)->SetEntries(1)
root [9] calib->GetHistoT0(0)->Draw("colz")
root [10] //Unsing the AliTPCCalPad class
root [11] AliTPCCalPad t0(calib->GetCalPadT0())
root [12] t0->MakeHisto2D()->Draw("colz"); //A-Side time arrival
root [13] t0->MakeHisto2D(1)->Draw("colz"); //C-Side time arrival
root [14] AliTPCCalPad q(calib->GetCalPadQ())
root [15] q->MakeHisto2D()->Draw("colz"); //A-Side signal sum
root [16] q->MakeHisto2D(1)->Draw("colz"); //C-Side signal sum
root [17] //display single chamber (0)
root [18] t0->GetCalROC(0)->MakeHisto2D()->Draw("colz")

```

Listing A.3: *commandsPulserCE.cint*



## B Additional data

### B.1 Pedestal and Noise calibration

Run Type			maximum			mean_0 <sup>2</sup>			RMS_0 <sup>2</sup>		
FC [kV]	ROC [kV]		IROC	OROC inner	OROC outer	IROC	OROC inner	OROC outer	IROC	OROC inner	OROC outer
0	0		0.68	0.73	0.73	0.688	0.774	0.860	0.059	0.159	0.226
1	0		0.68	0.73	0.77	0.709	0.806	0.915	0.103	0.197	0.258
10	0		0.68	0.73	0.77	0.723	0.825	0.943	0.126	0.215	0.267
10	0	dec.	0.68	0.73	0.77	0.725	0.800	0.914	0.131	0.191	0.256
10	0	short	0.68	0.73	0.77	0.721	0.824	0.943	0.123	0.214	0.267
20	0		0.68	0.73	0.77	0.734	0.832	0.960	0.148	0.219	0.272
50	0		0.68	0.73	0.77	0.744	0.848	0.984	0.161	0.231	0.286
100	≈1.4		0.68	0.73	0.77	0.745	0.843	0.994	0.167	0.228	0.290

**Table B.1:** Results of the noise analysis under different conditions. The max, mean and RMS values are given in ADC channels. The error on the maximum is  $2.5 \cdot 10^{-2}$ , on the mean and RMS it was estimated to be between  $3 \cdot 10^{-3}$  and  $3 \cdot 10^{-3}$  from IROC to the outer part of the OROC.

## B.2 Central Electrode analysis

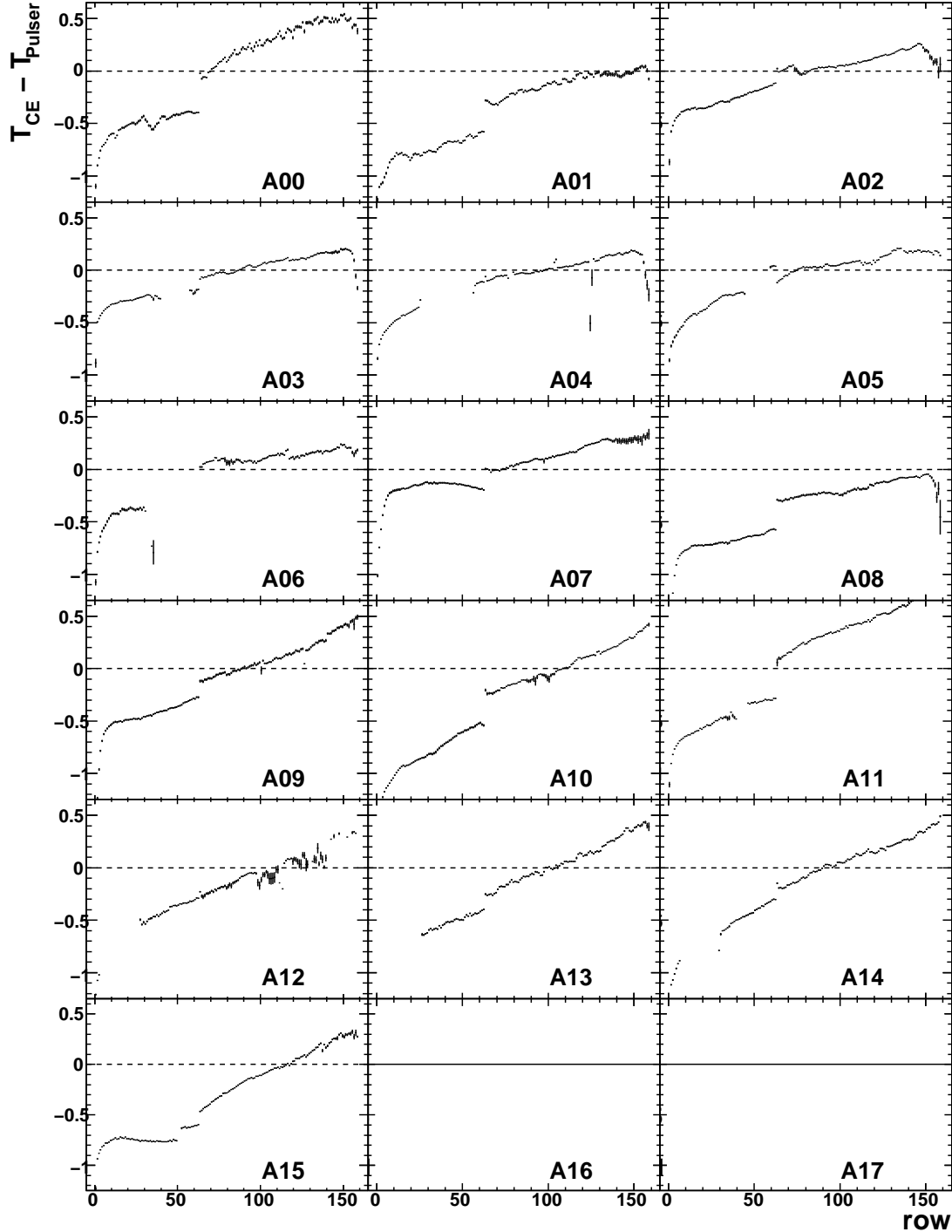


Figure B.1: Radial dependence of the central electrode drift time as a function of the global sector pad row (IROC: 0-62; OROC: 63-158) on the A-Side. For a more detailed description see 4.3.4.3.



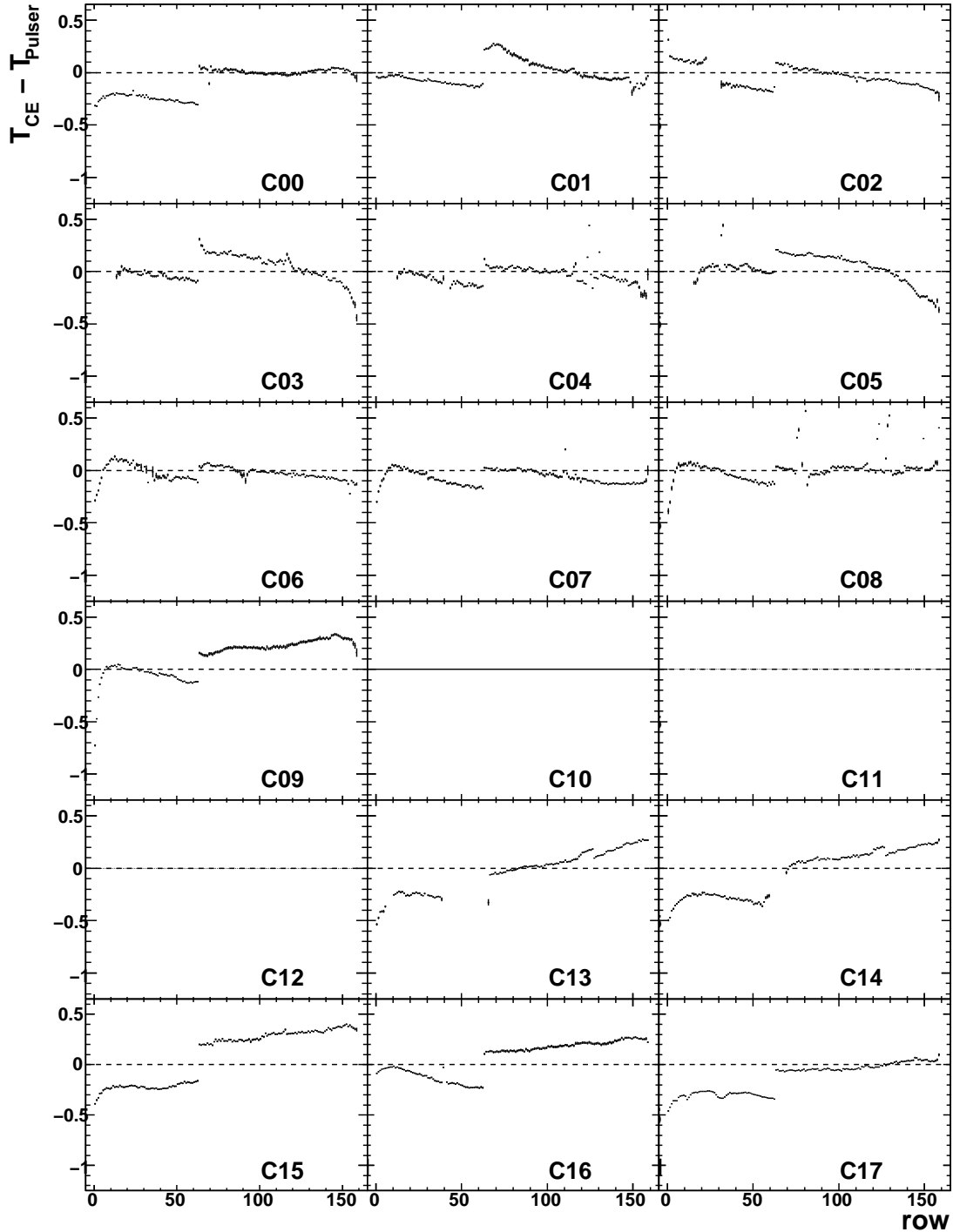


Figure B.2: Radial dependence of the central electrode drift time as a function of the global sector pad row (IROC: 0-62; OROC: 63-158) on the C-Side. For a more detailed description see 4.3.4.3.



# Bibliography

- [1] M. Gell-Mann, *A Schematic Model of Baryons and Mesons*, Phys. Lett. **8**, 214 (1964), [doi:10.1016/S0031-9163\(64\)92001-3](https://doi.org/10.1016/S0031-9163(64)92001-3).
- [2] E. D. Bloom *et al.*, *High-Energy Inelastic  $e - p$  Scattering at  $6^\circ$  and  $10^\circ$* , Phys. Rev. Lett. **23**, 930 (1969), [doi:10.1103/PhysRevLett.23.930](https://doi.org/10.1103/PhysRevLett.23.930).
- [3] J. D. Bjorken, *Asymptotic Sum Rules at Infinite Momentum*, Phys. Rev. **179**, 1547 (1969), [doi:10.1103/PhysRev.179.1547](https://doi.org/10.1103/PhysRev.179.1547).
- [4] R. P. Feynman, *Very High-Energy Collisions of Hadrons*, Phys. Rev. Lett. **23**, 1415 (1969), [doi:10.1103/PhysRevLett.23.1415](https://doi.org/10.1103/PhysRevLett.23.1415).
- [5] P. Aurenche, *The standard model of particle physics*, 1997, [arXiv:hep-ph/9712342](https://arxiv.org/abs/hep-ph/9712342).
- [6] D. J. Gross, *Twenty five years of asymptotic freedom*, Nucl. Phys. Proc. Suppl. **74**, 426 (1999), [arXiv:hep-th/9809060](https://arxiv.org/abs/hep-th/9809060), [doi:10.1016/S0920-5632\(99\)00208-X](https://doi.org/10.1016/S0920-5632(99)00208-X).
- [7] D. J. Gross and F. Wilczek, *Ultraviolet Behavior of Non-Abelian Gauge Theories*, Phys. Rev. Lett. **30**, 1343 (1973), [doi:10.1103/PhysRevLett.30.1343](https://doi.org/10.1103/PhysRevLett.30.1343).
- [8] H. D. Politzer, *Reliable Perturbative Results for Strong Interactions?*, Phys. Rev. Lett. **30**, 1346 (1973), [doi:10.1103/PhysRevLett.30.1346](https://doi.org/10.1103/PhysRevLett.30.1346).
- [9] S. Bethke,  *$\alpha(s)$  2002*, Nucl. Phys. Proc. Suppl. **121**, 74 (2003), [arXiv:hep-ex/0211012](https://arxiv.org/abs/hep-ex/0211012), [doi:10.1016/S0920-5632\(03\)01817-6](https://doi.org/10.1016/S0920-5632(03)01817-6).
- [10] F. Karsch, *Lattice QCD at high temperature and density*, Lect. Notes Phys. **583**, 209 (2002), [arXiv:hep-lat/0106019](https://arxiv.org/abs/hep-lat/0106019).
- [11] U. W. Heinz, *The little bang: Searching for quark-gluon matter in relativistic heavy-ion collisions*, Nucl. Phys. **A685**, 414 (2001), [arXiv:hep-ph/0009170](https://arxiv.org/abs/hep-ph/0009170), [doi:10.1016/S0375-9474\(01\)00558-9](https://doi.org/10.1016/S0375-9474(01)00558-9).
- [12] T. D. Lee, *Abnormal nuclear states and vacuum excitation*, Rev. Mod. Phys. **47**, 267 (1975), [doi:10.1103/RevModPhys.47.267](https://doi.org/10.1103/RevModPhys.47.267).
- [13] U. W. Heinz, *Concepts of heavy-ion physics*, 2004, [arXiv:hep-ph/0407360](https://arxiv.org/abs/hep-ph/0407360).
- [14] P. Braun-Munzinger, K. Redlich and J. Stachel, *Particle production in heavy ion collisions*, nucl-th/0304013, [arXiv:nucl-th/0304013](https://arxiv.org/abs/nucl-th/0304013).
- [15] T. Matsui and H. Satz,  *$J/\psi$  Suppression by Quark-Gluon Plasma Formation*, Phys. Lett. **B178**, 416 (1986), [doi:10.1016/0370-2693\(86\)91404-8](https://doi.org/10.1016/0370-2693(86)91404-8).
- [16] J. Rafelski and B. Muller, *Strangeness Production in the Quark - Gluon Plasma*, Phys. Rev. Lett. **48**, 1066 (1982), [doi:10.1103/PhysRevLett.48.1066](https://doi.org/10.1103/PhysRevLett.48.1066).

---

**BIBLIOGRAPHY**

---

- [17] ALICE Collaboration, *ALICE: Physics Performance Report, Volume I*, J. Phys. **G30**, 1517 (2004), [doi:10.1088/0954-3899/30/11/001](https://doi.org/10.1088/0954-3899/30/11/001).
- [18] ALICE Collaboration, *ALICE: Physics Performance Report, Volume II*, J. Phys. **G32**, 1295 (2006), [doi:10.1088/0954-3899/32/10/001](https://doi.org/10.1088/0954-3899/32/10/001).
- [19] ALICE Collaboration, *Technical Design Report of the Inner Tracking System*, CERN/LHCC 99-12, 1999.
- [20] ALICE Collaboration, *Technical Design Report of the Time Projection Chamber*, CERN/LHCC 2000-001, 2000.
- [21] ALICE Collaboration, *Technical Design Report of the Transition Radiation Detector*, CERN/LHCC 2001-021, 2001.
- [22] ALICE Collaboration, *Technical Design Report of the Time of Flight System*, CERN/LHCC 2000-012, 2000.
- [23] ALICE Collaboration, *Technical Design Report of the High Momentum Particle Identification Detector*, CERN/LHCC 98-19, 1998.
- [24] ALICE Collaboration, *Technical Design Report of the Photon Spectrometer*, CERN/LHCC 99-4, 1999.
- [25] ALICE Collaboration, *The Electromagnetic Calorimeter Addendum to the Technical Proposal*, CERN-LHCC-2006-014, 2006.
- [26] ALICE Collaboration, *Technical Design Report of the Dimuon Forward Spectrometer*, CERN/LHCC 99-22, 1999.
- [27] ALICE Collaboration, *Technical Design Report of the Zero Degree Calorimeter (ZDC)*, CERN/LHCC 99-5, 1999.
- [28] ALICE Collaboration, *Technical Design Report on Forward Detectors: FMD, T0, V0*, CERN-LHCC-2004-025, 2004.
- [29] ALICE Collaboration, *Technical Design Report of the Photon Multiplicity Detector (PMD)*, CERN/LHCC 99-32, 1999.
- [30] L. Betev and P. Chochula, *Definition of the ALICE Coordinate System and basic rules for Sub-Detector Components numbering*, ALICE-INT-2003-038, 2003.
- [31] W. Blum and L. Rolandi, *Particle Detection with Drift Chambers* (Springer-Verlag, 1994).
- [32] W.-M. Yao *et al.*, *Review of Particle Physics*, J. Phys. **G33**, 1+ (2006).
- [33] J. H. Parker and J. J. Lowke, *Theory of Electron Diffusion Parallel to Electric Fields. I. Theory*, Phys. Rev. **181**, 290 (1969), [doi:10.1103/PhysRev.181.290](https://doi.org/10.1103/PhysRev.181.290).
- [34] A. Kühmichel, *New developments in high precision, high particle density tracking with time projection chambers*, Nucl. Instr. Meth. **A360**, 52 (1995), [doi:10.1016/0168-9002\(94\)01221-0](https://doi.org/10.1016/0168-9002(94)01221-0).
- [35] L. Musa, private communication.

- [36] J. Wiechula *et al.*, *High-precision measurement of the electron drift velocity in Ne-CO<sub>2</sub>*, Nucl. Instr. Meth. **A548**, 582 (2005), doi:10.1016/j.nima.2005.05.031.
- [37] D. Vranić, *Drift Distortions in Alice TPC Field Cage*, ALICE-INT-1997-22, CERN-ALICE-INT-1997-22, 1997.
- [38] J. Baechler, C. Garabatos, M. Hoch, M. Kowalski and T. Meyer, *Calculation of power dissipation in the TPC resistor chains*, ALICE-INT-2001-12, 2001.
- [39] R. Veenhof, *Calculations for the Alice TPC read-out*, <http://rjd.home.cern.ch/rjd/Alice/>.
- [40] D. Vranić, private communication.
- [41] H. Stelzer *et al.*, *The ALICE TPC Readout Chamber: From Prototypes to Series Production*, ALICE-INT-2003-017, 2003.
- [42] L. Musa *et al.*, *The ALICE TPC front end electronics*, in *IEEE Nuclear Science Symposium* Vol. 5, pp. 3647–3651, 2003, doi:10.1109/NSSMIC.2003.1352697.
- [43] CERN-EP/ED, *ALICE TPC Readout Chip User Manual*.
- [44] <http://ep-ed-alice-tpc.web.cern.ch/ep-ed-alice-tpc/>.
- [45] C. Gutierrez *et al.*, *The ALICE TPC Readout Control Unit*, in *2005 IEEE Nuclear Science Symposium Conference Record* Vol. 1, pp. 575–579, 2005, doi:10.1109/NSSMIC.2005.1596317.
- [46] C. Lippmann and D. Vranić, *Alice TPC Numbering Conventions*, <http://lippmann.web.cern.ch/lippmann/TPC/num.pdf>, 2007.
- [47] H. J. Hilke, *Detector calibration with lasers – A review*, Nuclear Instruments and Methods in Physics Research A **A252**, 169 (1986), doi:10.1016/0168-9002(86)91177-0.
- [48] B. Nielsen, J. Westergaard, J. Gaardhoje and A. Lebedev, *Design Note on the ALICE TPC laser calibration system*, ALICE-INT-2002-022, 2002.
- [49] G. Renault, B. S. Nielsen, J. Westergaard and J. J. Gaardhoje, *The laser of the ALICE time projection chamber*, 2007, arXiv:nucl-ex/0703042.
- [50] C. Garabatos, *The ALICE TPC*, Nucl. Instr. Meth. **A535**, 197 (2004), doi:10.1016/j.nima.2004.07.127.
- [51] C. Markert, *Driftgeschwindigkeitsmessung zur Gasüberwachung im NA49-Experiment*, Diplomarbeit, Johann Wolfgang Goethe-Universität, Frankfurt am Main, 1995.
- [52] D. Antończyk, *Detailed Analysis of Two Particle Correlations in Central Pb-Au Collisions at 158 GeV per Nucleon*, Doktorarbeit, Technische Universität Darmstadt, 2006.
- [53] M. Pimenta dos Santos, *ALICE TPC READ OUT CHAMBERS COOLING SYSTEM*, CERN-ST/CV-2003-490540, 2003.

---

## BIBLIOGRAPHY

---

- [54] U. Frankenfeld, S. Popescu and H. Schmidt, *Experimental Evaluation of the ALICE TPC Front-End Electronics Cooling Strategy*, ALICE-INT-2005-001, 2005.
- [55] U. Frankenfeld, S. Popescu and H. Schmidt, *Temperature Monitoring System for the ALICE TPC*, ALICE-EN-2005-001, 2005.
- [56] <http://elmb.web.cern.ch/ELMB/>.
- [57] *TPC Commissioning Homepage*, <https://webh06.cern.ch/alice-tpc-commissioning/>.
- [58] <http://elinares.home.cern.ch/elinares/ACORDE/index.html>.
- [59] V. Prasad, *ALICE-TPC Photogrammetric measurements of TPC readout chambers on the shaft side before shimming*, ALICE survey document; EDMS number: 640963, 2005.
- [60] V. Prasad, *ALICE-TPC Photogrammetric measurements of TPC readout chambers on the shaft side*, ALICE survey document; EDMS number: 671106, 2005.
- [61] V. Prasad, *ALICE-TPC Photogrammetric measurements of TPC readout chambers on muon side*, ALICE survey document; EDMS number: 671815, 2005.
- [62] V. Prasad, *ALICE-TPC, Photogrammetric measurement of TPC readout chambers on the Shaft side (Side-A), after re-shimming*, ALICE survey document; EDMS number: 691786, 2005.
- [63] V. Prasad, *ALICE-TPC, Photogrammetric measurement of TPC readout chambers on the Muon side (Side-C), after re-shimming*, ALICE survey document; EDMS number: 691788, 2005.
- [64] <http://aliceinfo.cern.ch/Offline>.
- [65] R. Toft-Petersen, *The Laser Calibration System of the ALICE Time Projection Chamber*, Master's thesis, 2008.

# List of Figures

1.1	Running of the strong coupling constant . . . . .	3
1.2	Lattice QCD calculations of the energy density of nuclear matter as a function of the temperature . . . . .	5
1.3	The phase diagram of QCD . . . . .	5
2.1	The ALICE detector system . . . . .	9
2.2	ALICE PID performance . . . . .	10
2.3	ALICE coordinate systems . . . . .	13
3.1	View of the TPC . . . . .	15
3.2	Basic structure of a TPC . . . . .	16
3.3	Sketch of a multiwire proportional chamber with segmented cathod pads . . . . .	17
3.4	Energy loss of fast charged particles as a function of their momentum . . . . .	18
3.5	Transition scheme for the two photon ionisation process . . . . .	19
3.6	Transverse and longitudinal diffusion coefficients . . . . .	23
3.7	Sketch of a pad signal . . . . .	24
3.8	Side view of the TPC . . . . .	25
3.9	Schematic drawing of the TPC field cage components . . . . .	26
3.10	Picture of the inner field cage rods and field strips . . . . .	27
3.11	Resistor scheme . . . . .	27
3.12	Wire geometry of the inner and outer readout chambers . . . . .	29
3.13	Readout chamber details . . . . .	29
3.14	Main components of the front end cards . . . . .	30
3.15	Block diagram of the ALTRO chip . . . . .	30
3.16	Picture of a completely equipped sector . . . . .	33
3.17	Technical drawing of the end-plates. . . . .	33
3.18	Principle of the TPC laser system . . . . .	35
3.19	Design of the micro-mirror bundles of the laser system . . . . .	35
3.20	Front end card wrapped in copper plates . . . . .	37
3.21	Cooling circuit schematics . . . . .	38
4.1	Schematics of the cooling system used during the commissioning . . . . .	42
4.2	Deviations of the survey points of the ROCs from the ideal case . . . . .	44
4.3	Typical electronic baseline of one channel . . . . .	45
4.4	Pedestal and noise distribution of all sectors . . . . .	46
4.5	2D noise distribution in the TPC . . . . .	47
4.6	Correlation of noise and PCB track length . . . . .	49
4.7	2D noise distribution of channels with ‘high noise’ . . . . .	50
4.8	Noise as a function of the field cage high voltage . . . . .	52
4.8	Normalised 2D noise distributions . . . . .	53
4.9	2D noise distribution after the change of the FEE grounding scheme . . . . .	54

---

**LIST OF FIGURES**

---

4.10	Typical Calibration Pulser signal shape in one readout channel . . . . .	55
4.11	Relative timing differences within one ROC . . . . .	56
4.12	Distribution of timing differences within all sectors . . . . .	57
4.13	2D Outlier distribution from the Calibration Pulser time analysis . . . . .	57
4.14	Normalised charge distributions . . . . .	58
4.15	Normalised charge distribution for all sectors . . . . .	59
4.16	2D Outlier distribution . . . . .	59
4.17	Laser ray positions - design and measurements . . . . .	60
4.18	Central electrode time information in one OROC and the effect of Calibration Pulser corrections . . . . .	61
4.19	Signal sum on the A- and C-Side . . . . .	62
4.20	Mean radial dependence of the central electrode drift time measurements . . . . .	63
4.21	Measured derivatives in local x and local y on the A-side . . . . .	65
4.22	Measured derivatives in local x and local y on the C-side . . . . .	66
4.23	Drift velocity as a function of the date . . . . .	67
5.1	Noise distribution of sectors on the C-Side . . . . .	70
5.2	Sketch of one channel of the LV power supply to illustrate the common-mode current . . . . .	71
5.3	Common-mode current at the output of the LV power supply . . . . .	71
5.4	Sketch of one channel of the LV power supply with ferrite toroids . . . . .	72
5.5	Mean and RMS of noise distributions for different configurations with ferrite toroids . . . . .	73
5.6	2D noise ratio of different toroid configurations in sector C05 . . . . .	73
5.7	Noise distribution of all sectors . . . . .	74
5.8	2D noise distribution in the TPC . . . . .	75
5.9	Correlation of noise and PCB track length . . . . .	76
5.10	2D noise distribution in the TPC . . . . .	77
A.1	Hierarchy of the event processing functions of the calibration algorithms . . . . .	81
A.2	Example of a reference histogram . . . . .	82
A.3	Process flow of the calibration algorithms . . . . .	82
B.1	Radial dependence of the central electrode drift time as a function of the global sector pad row on the A-Side . . . . .	90
B.2	Radial dependence of the central electrode drift time as a function of the global sector pad row on the C-Side . . . . .	91



# List of Tables

1.1	Fermions of the Standard Model . . . . .	2
3.1	Size and number of readout pads. . . . .	28
3.2	Number of front end cards in each readout patch. . . . .	32
4.1	Maximum noise and truncated mean and its RMS for the different pad sizes	46
4.2	Fit parameters of the noise vs. pcb track length line fits . . . . .	50
4.3	Mathematical conditions for the outlier strips of the central electrode. $g_x$ and $g_y$ denote the x and y position in the global coordinate frame, the unit is cm. For a description of the cut names see text. . . . .	62
4.4	Results of the global misalignment study . . . . .	66
4.5	Floating anode and cathode wires found in the calibration pulser analysis. .	68
5.1	Maximum noise and truncated mean and its RMS for the different pad sizes	70
5.2	Maximum noise and truncated mean and its RMS between for the different pad sizes . . . . .	74
5.3	Fit parameters of the noise vs. pcb track length line fits . . . . .	77
A.1	Calibration values in the pedestal calibration class . . . . .	83
A.2	Calibration values in the pulser calibration class . . . . .	84
A.3	Calibration values in the central electrode calibration class . . . . .	86
A.4	Event by event information in the central electrode calibration class . . . . .	86
B.1	Results of the noise analysis under different conditions . . . . .	89



# Danksagung

Zunächst möchte ich mich bei meinem Doktorvater Priv. Doz. Dr. Hans-Rudolf Schmidt bedanken, der mich über die dreieinhalb Jahre meiner Promotion begleitet hat. Ob beim gemeinsamen Joggen, Kaffeetrinken oder mit einem Lötkolben nebeneinander auf dem Gerüst vor der TPC sitzend, wurde er nicht müde, meine Fragen mit mir zu diskutieren.

Nicht weniger Dank gilt Prof. Dr. Braun-Munzinger, der es mir ermöglicht hat, in einer so spannenden Phase von ALICE an vorderster Front dabei zu sein. Nicht nur zu sehen, sondern auch aktiv daran mitzuwirken, wie die ALICE TPC von einer leeren Hülle in kleinen Schritten zu einem hochpräzisen, unter seiner Art größten Detektor heranwächst, hat mich stark geprägt.

Ebenfalls bedanken möchte ich mich bei Prof. Dr. Christoph Blume, der das Zweitgutachten meiner Arbeit übernommen hat.

Danken möchte ich auch Chilo Garabatos und Danilo Vranić, die mittlerweile am CERN "stationiert" sind. Von ihnen erhielt ich wertvolle Informationen über den genauen Aufbau und die Funktionsweise der TPC, die so nirgends zu lesen sind.

Sehr genossen habe ich meine Aufenthalte in der 'Casa Rudi', unserer Physiker-WG am CERN. Neben meinem Doktorvater teilte ich dort das Dach mit Dr. Ulrich Frankenfeld, Daniel Soyk, Dr. Rainer Renfordt und Prof. Dr. Peter Glässel. Zahlreiche physikalische (und natürlich auch nicht-physikalisch) Diskussionen beim Abendessen oder vor dem Kamin haben meine Aufenthalte am CERN wesentlich bereichert.

Viel bedeutet mir auch das aus meiner Sicht einmalige Arbeitsklima, welches über die Jahre hinweg in unserer kleinen TPC-Gruppe an der GSI gewachsen ist. Zusammen mit Rudi, Uli, Daniel und Jörg Hehner konnte ich mir den neben der Schreibtischarbeit wichtigen sportlichen Ausgleich holen. Oft wurde die Mittagspause für eine Jogging-Runde im "GSI-Wald" genutzt. Obligatorisch geworden ist auch unser Jahresabschluss-Lauf mit anschließendem gemütlichen Ausklang.

Meinen Eltern, vor allem meiner Mutter, möchte ich von ganzem Herzen danken. Ohne ihre Unterstützung in jeglicher Hinsicht wäre ein Studium und die anschließende Promotion für mich nicht so leicht zu bewältigen gewesen.

Nicht zuletzt möchte ich mich bei meiner Freundin Nina bedanken, die mit mir im letzten halben Jahr eine ganz gewiss nicht immer einfache Zeit durchgemacht hat.



# Curriculum Vitae

## Personal data

name	Jens Wiechula
date of birth	13th November 1978
place of birth	Berlin
nationality	German
address	Adolf-Kolping-Str. 28 64625 Bensheim Deutschland

## Education

2004 to 2008	Ph.D. in nuclear physics, GSI Darmstadt / J.W.G. University Frankfurt
1999 to 2004	Diploma in physics, J.W.G. University Frankfurt
1989 to 1998	Grammar school, Goethe-Gymnasium, Frankfurt a. M.
1984 to 1989	Basic school, Henri-Dunant-Grundschule, Frankfurt a. M.

## Civilian service

1998 to 1999	Katholisches Jugendamt Frankfurt
--------------	----------------------------------

## Awards

2006	Philipp Siedler-Wissenschaftspreis
------	------------------------------------

## Professional experience

### *Work:*

2004 to 2008 Research assistant, GSI Darmstadt

- Assembly and commissioning of the ALICE TPC
- Development of calibration algorithms for the ALICE TPC

### *Schools:*

2007 Helmholtz Research School: Lecture Week on Chiral Symmetry, Kleinwalsertal

2005 QGP International School, Turin

## Teaching Experience

Leading of exercise classes in

*Theoretical Physics:*

Mechanics, Electrodynamics, Quantum Mechanics I, fall 2002 to summer 2004

*Mathematics:*

Analysis, summer 2002

## Publications

J. Lukasik et al., ALADIN2000 Collaboration, Discriminant analysis and secondary-beam charge recognition, Nucl.Instrum.Meth.A587 (2008) 413-419.

C. Sfienti et al., ALADIN2000 Collaboration, Isotopic effects in nuclear reactions at relativistic energies, Proceedings of the 45th International Meeting on Nuclear Physics, Bormio, Italy, 14-21 Jan 2007

C. Sfienti et al., ALADIN2000 Collaboration, Gross Properties and Isotopic Phenomena in Spectator Fragmentation, Nucl.Phys.A787 (2007) 627-632.

B. Alessandro et al., ALICE Collaboration, ALICE: Physics Performance Report, Vol.II, J.Phys.G32 (2006) 1295-2040.

C. Sfienti et al., ALADIN2000 Collaboration, Mass and isospin dependence in multifragmentation, Acta Phys.Polon.B37 (2006) 193-198.

J. Wiechula, et al., High-precision measurement of the electron drift velocity in NeCO<sub>2</sub>, Nucl.Instrum.Meth.A548 (2005) 582-589.

C. Sfienti et al., ALADIN2000 Collaboration, Mass and isospin effects in multifragmentation, Nucl.Phys.A749 (2005) 83-92.

## Talks

Alice TPC Collaboration Meeting, Pedestal and Pulser Calibration, 2008.

Alice TPC Collaboration Meeting, Local and global alignment using the CE, 2007.

TPC Calibration meeting, TPC calibration algorithms, T0 and Time CE calibration, 2007.

Internal group seminar GSI, Introduction to the ALICE TPC, 2007.

Frühjahrstagung der Deutschen Physikalischen Gesellschaft e. V. , Precision measurement of the electron drift velocity in NeCO<sub>2</sub>, 2004.

## Technical skills

OS: Windows, Linux

programming: C++, ROOT, AliRoot

web programming: HTML, PHP, Rails

applications: Most Microsoft programs (MSOffice), OpenOffice, LabView, L<sup>A</sup>T<sub>E</sub>X